Phase separation, degassing, and resorption of H_2O in phonolitic melt investigated by decompression experiments

Dissertation

der Mathematisch-Naturwissenschaftlichen Fakultät

der Eberhard Karls Universität Tübingen

zur Erlangung des Grades eines

Doktors der Naturwissenschaften

(Dr. rer. nat.)

vorgelegt von

M.Sc. Anja Allabar

aus Stuttgart

Tübingen

2020

Gedruckt mit Genehmigung der Mathematisch-Naturwissenschaftlichen Fakultät der Eberhard Karls Universität Tübingen.

Tag der mündlichen Qualifikation:	13.11.2020
Stellvertretender Dekan:	Prof. Dr. József Fortágh
1. Berichterstatter:	Prof. Dr. Marcus Nowak
2. Berichterstatter:	Prof. Dr. Hans Keppler
3. Berichterstatter	Prof. Dr. Max Wilke

Acknowledgements

This work was funded by the by the German Science Foundation (DFG NO378/12-1).

My special thanks goes to **Marcus Nowak** for providing this project to me and supervising me through my PhD studies. In the last years, a countless amount of questions have been answered and discussed with patience, undivided attention and genuine interest. I am especially grateful that I was encouraged and pushed to my limits, while at the same time, I was given enough support but also freedom to walk this path in my own pace whenever necessary.

I am very thankful to **Hans Keppler** for being my second supervisor who gave me guidance and support. He provided help and answers to all questions that came up in the last years. I always appreciated this second opinion.

Thanks to **Paul Bons** for his ongoing interest in our work and the involvement during the early stage of my research.

I want to thank **Holger Marxer** and **Christopher Giehl** for training me at the very beginning of my scientific career to provide me a great laboratory basis for my work.

I thank **Annette Flicker** not only for her technical support, for which she was always available, but also for having an open ear for other problems. The same applies to **Barbara Maier,** without whom our experimental work would not be possible in this quality. Furthermore, I want to thank **Simone Schafflick.** She contributed to my work with her excellent sample preparation, she always responded to my spontaneous requests and continuously showed interest in my work.

I am thankful to **Kate Dobson** and **Ed Lewellin** for giving me the chance to join their teams during experimental synchrotron campaigns. These research stays were very valuable scientific experiences for me. Within this frame, I want to thank **Jason Coumans**, **Fabian Wadsworth**, **Mathieu Colombier**, **Jeremie Vasseur**, **Francisco Cáceres**, **Bettina Scheu** and **Madeleine Humphreys**. It was a pleasure to work in this great team.

Thanks to **Dork Sahagian** for the interest in my work and the overall support that encouraged me as a researcher.

Another special thanks goes to the colleagues of my working group **Patricia Petri**, **Dennis Eul**, **Eskil Salis Gross** and other colleagues from the department **Catherine Bauer, Tatjana Epp**, **Frieder Lauxmann**, **Arno Knittel**, **Stefan Kreißl**, **Maximilian Keim**, **Rebekka Reich**, **Manuel Scharrer** for the great time and the enjoyable working atmosphere.

Finally, I especially want to thank my **family and friends** for their unconditional love and support at any time.

Author contributions

Study I: Allabar A, Nowak M (2018) Message in a bottle: Spontaneous phase separation of hydrous Vesuvius melt even at low decompression rates. Earth Planet Sci Lett 501:192-201

Author	Author position	Scientific ideas %	Data generation %	Analysis %	Interpre-tation %	Paper writing %
Anja Allabar	1st	50	100	100	50	50
Marcus Nowak	2nd	50	0	0	50	50
Title of paper:		Message in a bottle: Spontaneous phase separation of hydrous Vesuvius melt even at low decompression rates.				
Status in publication process:		published				

Study II: Allabar A, Salis Gross E, Nowak M (2020a) The effect of initial H_2O concentration on decompression-induced phase separation and degassing of hydrous phonolitic melt. Contrib Mineral Petrol 175:22

Author	Author position	Scientific ideas %	Data generation %	Analysis %	Interpre-tation %	Paper writing %
Anja Allabar	1st	85	75	75	75	80
Eskil Salis Gross	2nd	0	15	15	5	5
Marcus Nowak	3rd	15	0	0	20	15
Title of paper:		The effect of initial H_2O concentration on decompression-induced phase separation and degassing of hydrous phonolitic melt.				
Status in publication process:		published				

Study III: Allabar A, Dobson KJ, Bauer CC, Nowak M (2020b) Vesicle shrinkage in hydrous phonolitic melt during cooling. Contrib Mineral Petrol 175:21

Author	Author position	Scientific ideas %	Data generation %	Analysis %	Interpre-tation %	Paper writing %
Anja Allabar	1st	85	95	90	90	75
Katherine J. Dobson	2nd	5	5	5	0	10
Catherine C. Bauer	3rd	0	0	5	0	5
Marcus Nowak	4th	10	0	0	10	10
Title of paper:		Vesicle shrinkage in hydrous phonolitic melt during cooling				
Status in publication process:		published				

Table of Contents

Zusammenfassung

Explosive Vulkanausbrüche werden durch dynamische Prozesse im Erdinneren angetrieben. Magmen enthalten leichtflüchtige Komponenten, von denen H_2O am häufigsten vorkommt. Bei magmatischen Bedingungen können bis zu einige Gew% H_2O in Silikatschmelzen gelöst sein. Die starke Druckabhängigkeit der H_2O-Löslichkeit bewirkt eine Schmelzentgasung durch die Bildung und das Wachstum von Fluidblasen, wenn eine Schmelze beispielsweise durch den Aufstieg in der Erdkruste dekomprimiert wird. Die Blasenanzahl pro Schmelzvolumen und die Porosität einer Schmelze sind wichtige Parameter, die großen Einfluss auf die Dynamik vulkanischer Eruptionen haben. Die Blasenbildung und das Blasenwachstum verringern die Gesamtdichte der Schmelze. Damit wird der Magmenaufstieg durch zunehmenden Auftrieb beschleunigt, was letztendlich zu explosivem Vulkanismus führen kann.

Mithilfe von Dekompressionsexperimenten bei hohen Temperatur- und Druckbedingungen kann der Magmenaufstieg im Labor simuliert werden. Dies ermöglicht die Untersuchung von in der Natur nicht zugänglichen Entgasungsprozessen. Im Rahmen dieser Arbeit wurde anhand von Dekompressionsexperimenten die homogene Blasenbildung in H_2O-haltiger phonolitischer Silikatschmelze mit der Bims-Zusammensetzung der AD79 Eruption des Vesuvs untersucht. Es wurde eine konstant hohe Blasenanzahl pro Schmelzvolumen ($\sim 10^5$ mm^{-3}) unabhängig von der Dekompressionsrate nachgewiesen (Studie 1). Dies ist nicht mit der Nukleationstheorie vereinbar, welche üblicherweise zur Beschreibung der Blasenbildung in Silikatschmelzen angewendet wird. Alternativ dazu wurde auf Grundlage dieser neuen experimentellen Daten die spinodale Entmischung als Phasenseparationsmechanismus hydrierter phonolitischer Schmelze vorgeschlagen. Diese spontane Phasenseparation führt zu einer plötzlichen Entgasung, welche selbst bei niedrigen Dekompressionsraten zu explosiven Eruptionen führen kann.

Während die Dekompressionsrate keinen Einfluss auf die Anzahl an Blasen pro Schmelzvolumen in phonolitischer Schmelze hat, konnte gezeigt werden, dass die Anzahl mit der initial gelösten H_2O-Konzentration (3.3–6.3 Gew%) um eine Größenordnung variiert (Studie II). Des Weiteren wurde eine Veränderung der Entgasungsentwicklung bei einer initialen H_2O-Konzentration von 5.6 Gew% nachgewiesen. Bei niedrigerer initialer H_2O-Konzentration können die in natürlichen vulkanischen Produkten beobachteten Texturen die initial gebildeten Blasen darstellen. Bei höherer initialer H_2O-Konzentration, oder im Fall von heterogener Nukleation an Kristalloberflächen, sind diese jedoch wahrscheinlich durch Koaleszenz oder sekundäre Blasenbildung überprägt.

Neben der Untersuchung der Schmelzentgasung behandelt diese Arbeit das experimentelle Problem des Blasenschrumpfens beim Abkühlen (Studie III). Das Blasenschrumpfen kann beim Abschrecken blasenhaltiger Silikatschmelze zu porösem Glas auftreten. Dieser Abkühlungsprozess ist jedoch notwendig um die Probenanalyse bei Umgebungsbedingungen zu ermöglichen. Diese Studie zeigt, dass Blasen während des Abkühlens signifikant schrumpfen können, sodass die Glasporosität weniger als die Hälfte

der ursprünglichen Schmelzporosität betragen kann. Dies ist auf das sinkende Molvolumen von H_2O sowie auf die Resorption von H_2O aus den Blasen zurück in die Schmelze zurückzuführen. Folglich entsprechen die Glasporosität und die H_2O-Konzentration im Glas nicht notwendigerweise der Schmelzporosität und der H_2O-Konzentration in der Schmelze vor dem Abkühlen. Dies stellt ein Problem für die Interpretation von Entgasungsvorgängen dar, die aus Texturen und H_2O-Konzentrationen abgekühlten Proben abgeleitet wird. Insbesondere der Vergleich experimenteller Proben mit natürlichen vulkanischen Produkten kann ohne Korrektur der Porosität zu Fehlinterpretationen führen. Daher wurden neue Methoden zur Analyse und Interpretation des Blasenschrumpfens und der H_2O-Resorption entwickelt, welche für zukünftigen Studien nützlich sind um Ergebnisse von Dekompressionsexperimenten korrekt auf natürliche vulkanische Prozesse zu übertragen.

Abstract

Explosive volcanic eruptions are driven by dynamic processes in the Earth's interior. Within volcanic systems, magmas contain volatiles of which H_2O is the most abundant. At magmatic pressures and temperatures, up to several wt% H_2O can be dissolved in silicate melt. The strong pressure dependence of H_2O solubility causes melt degassing by formation and growth of vesicles when a melt is decompressed by, for instance, magma ascent. The vesicle number density and the porosity of a melt are important parameters that strongly influence the dynamics of volcanic eruptions. Vesiculation decreases the melt density. This accelerates magma ascent by increased buoyancy, eventually causing explosive volcanic eruptions.

Decompression experiments at high temperature and pressure are used to simulate magma ascent in the laboratory. This enables the investigation of melt degassing processes that are not directly accessible for observation in nature. Within the frame of this work, the homogeneous vesicle formation in hydrous phonolitic melt with white pumice composition of the AD79 Vesuvius eruption was investigated by means of decompression experiments. A constant high vesicle number density (~10^5 mm^{-3}) independent from decompression rate was found (Study I). This contrasts nucleation theory that is commonly used to describe vesicle formation in silicate melts. Based on these new experimental data, spinodal decomposition was proposed as an alternative phase separation mechanism in phonolitic melts. This spontaneous phase separation may cause sudden melt degassing, triggering explosive eruptions, even at low decompression rates.

While the decompression rate does not influence the vesicle number density in phonolitic melt, it was shown that the vesicle number density varies by one order of magnitude with initially dissolved H_2O concentration (3.3–6.3 wt%) (Study II). Furthermore, a change in degassing evolution at 5.6 wt% initial H_2O concentration was found. At lower concentration, the textures observed in natural volcanic products can represent the initially formed vesicles. At higher concentration or if heterogeneous nucleation on crystals is involved, vesicle textures are likely obscured by coalescence or secondary vesicle formation.

Besides the investigation of melt degassing, this work focusses on the experimental problem of vesicles shrinkage during cooling (Study III), which may occur when samples are rapidly quenched to glass in order to facilitate analysis at ambient conditions. The study shows that vesicles can significantly shrink during cooling, resulting in a glass porosity less than half the melt porosity. Vesicle shrinkage is governed by the decrease in molar volume of H_2O and the resorption of H_2O from fluid vesicles back into the melt during cooling. Consequently, the glass porosity and H_2O concentration in the glass do not necessarily represent the melt porosity and the H_2O concentration in the melt before cooling. This poses a problem in the interpretation of degassing processes derived from quenched decompression experiments. Especially the comparison of experimental samples with natural volcanic products can lead to misinterpretations when melt porosity is directly derived from glass porosity. Therefore, new methods for the analysis and interpretation of vesicle shrinkage and H_2O resorption are developed, which are useful for future studies to correctly apply experimental results to natural volcanic processes.

Outline

Volcanic eruptions are driven by the exsolution of volatiles that are initially dissolved in magmas at high pressure (P) and temperature (T) in the Earth's interior. Among other volatiles like CO_2, Cl or S-species, H_2O is the most abundant volatile in magmatic volcanic systems (e.g., De Vivo et al. 2005). The solubility of H_2O in silicate melts of up to several wt% strongly correlates with pressure and depends only to a minor extent on temperature and melt composition (e.g., Holtz et al. 1995). Besides other mechanisms (Gonnermann and Manga 2007), the ascent and the resulting decompression of a hydrous silicate melt induces H_2O supersaturation until an H_2O fluid exsolves by vesicle formation. Once H_2O vesicles coexist with the silicate melt, H_2O supersaturation can be further decreased by H_2O diffusion from the melt into fluid vesicles. The associated vesiculation decreases magma density significantly and increases the buoyancy of the melt, leading to an acceleration of magma ascent. The positive feedback between decompression-induced supersaturation, vesiculation and magma ascent may then result in magma fragmentation and explosive volcanism (e.g., Alidibirov and Dingwell 1996; Kueppers et al. 2006; Genareau et al. 2012).

The initial process of vesicle formation, defining the onset of degassing, is a key parameter to understand silicate melt degassing and the mechanisms just before and during volcanic eruptions. The vesicle number density (*VND*) determines the degassing efficiency and can, thus, be crucial for the style of a volcanic eruption. Nucleation theory is the generally used mechanism to describe vesicle formation and to predict *VND*s in silicate melts (e.g., Navon and Lyakhovsky 1998). Vesicles can nucleate heterogeneously on crystal surfaces or homogeneously within a crystal-free melt volume. In either case, a supersaturation threshold must be reached to overcome the energy barrier defined by the surface tension of the newly formed surface. In case of heterogeneous vesicle formation on crystals, this energy barrier is reduced due to the decreased required surface energy (e.g., Hurwitz and Navon, 1994). In general, nucleation theory predicts a strong increase in the *VND* with increasing decompression rate and decreasing surface tension (Navon and Lyakhovsky 1998). These dependencies in turn provide tools to determine ascent or decompression rates of a melt through the *VND* observed in natural volcanic ejecta (Toramaru 2006) or to determine surface tension at experimentally controlled decompression rates (e.g., Shea et al. 2010a; Shea 2017).

Laboratory experiments are necessary to study magmatic conditions because the dynamic degassing processes within a volcanic system are not accessible for direct observation. Magma ascent is simulated with experiments at high P and T in order to investigate decompression-induced melt degassing in millimeter-sized samples. Rapid cooling (quenching) at any stage during a decompression experiment allows analysis at ambient conditions of partially degassed glassy samples. However, such decompression experiments are challenging because the experimental protocol can affect the experimental results. For instance, pre-existing vesicles that are present due to the choice of starting material, as well as ascending vesicles that nucleated at the experiment capsule, or the H_2O diffusion towards vesicles at the interface between capsule and melt can inhibit or alter the homogeneous phase separation process that is to be investigated (Iacono-Marziano et al. 2007; Marxer et al. 2015; Preuss et al. 2016). A strict experimental protocol, which is provided by Preuss et al. 2016, is necessary to account for these problems. The compliance with such a protocol is, however, accompanied by a limitation of the experimentally accessible window (e.g., concerning the choice of decompression rate or final pressure) in which homogeneous vesicle formation can be studied.

This work consists of three studies based on superliquidus decompression experiments using phonolitic melts with AD79 Vesuvius white pumice melt composition (VAD79). Homogeneous vesicle formation and degassing during decompression of phonolitic melt were studied, while accounting for the known experimental problems. Vesicle shrinkage during cooling is another experimental problem (McIntosh et al. 2014; Marxer et al. 2015) that is further explored. Therefore, besides the volcanological aspect, this work aims towards a correct interpretation of experimental results of decompression experiments to improve their application for the interpretation of natural vesiculated volcanic ejecta and their degassing history.

Decompression experiments conducted with hydrous rhyolitic melts, that agree with the experimental protocol of Preuss et al. (2016), have shown that decompression-induced, homogeneous vesicle formation can be described by nucleation theory (Gardner et al. 1999; Mourtada-Bonnefoi and Laporte 2004; Hamada et al. 2010) due to an exponential increase in the *VND* with decompression rate. In contrast, similar experiments with superliquidus phonolitic and trachytic melts (Iacono-Marziano et al. 2007; Marxer et al. 2015; Preuss et al. 2016) have not shown a clear dependence of *VND* on decompression rate. **Study I** of this

work (Allabar and Nowak 2018) builds on this discrepancy in the dependence of *VND* on decompression rate between rhyolitic and phonolitic melts. Further superliquidus decompression experiments with phonolitic melt confirmed a high *VND* (~10^5 mm^{-3}) independent from decompression rate, which is inconsistent with nucleation theory. This independence may instead be explained by the theory of spinodal decomposition (Cahn 1965; Debenedetti 2000) which is, thus, suggested as an alternative phase separation mechanism of hydrous phonolitic melt. The experimentally determined *VND* is in the same order of magnitude as the *VND* in the natural white pumice (e.g., Gurioli et al. 2005). An extremely high decompression rate of 18 MPa·s^{-1} would be necessary to explain this high *VND* with nucleation theory. Alternatively, the high *VND* has been suggested to be formed by heterogeneous nucleation on magnetite crystals, where decompression with only ~7 MPa·s^{-1} is necessary (Shea 2017). This study, however, revealed that the high *VND* can be formed at superliquidus conditions independent from decompression rate down to 0.06 MPa·s^{-1}. The results of this study have important consequences for the interpretation of melt degassing processes involving phonolitic melts. Even at low decompression rates, a high number of vesicles can be formed that may trigger explosive volcanic eruptions.

While Study I focuses on decompression experiments with a constant initial H_2O concentration (c_{H2Oini}) of 5.3 wt%, the natural eruptive products of the different stages of the AD79 Vesuvius eruption have been reported to originate from melts with c_{H2Oini} ranging between 3.0 and 6.4 wt% (Cioni 2000). In order to investigate the influence of c_{H2Oini} on homogeneous phase separation, further decompression experiments with phonolitic melt at a constant decompression rate but varying c_{H2Oini} of 3.3–6.3 wt% were performed within the frame of **Study II** (Allabar et al. 2020a). A minimum *VND* of ~10^5 mm^{-3} at ~5 wt% initial H_2O concentration with increasing values by one order of magnitude at both lower and higher c_{H2Oini} was found. Furthermore, the absence of Fe-oxide nanolites was confirmed by Raman micro-spectroscopy. Nanolites are suggested to initiate heterogeneous nucleation (Di Genova et al. 2017a; 2018; Shea 2017) but could potentially have been overlooked during the analysis with other methods. Their absence supports that phase separation in the experiments included in this study was homogeneous. Thus, the *VND* dependence on c_{H2Oini} may also be qualitatively explained by spinodal decomposition.

In addition, the experimental results of Study II revealed a change in degassing behavior with c_{H2Oini} during continuous decompression, investigated by experiments that are

decompressed to different final pressures. At c_{H2Oini} < 5.6 wt%, the initially formed *VND* remained stable down to low pressures. At such conditions, the initial *VND* is likely preserved until the eruption of a magma to the Earth's surface. This was confirmed by the accordance of the experimental *VND*s at low c_{H2Oini} with the natural *VND*s observed in natural products of the AD79 Vesuvius eruption (Cioni 2000, Shea et al. 2014). At c_{H2Oini} > 5.6 wt% the initially formed high *VND* of almost 10^6 mm^{-3} was found to be erased within a short pressure interval by massive coalescence during further decompression with a remaining *VND* up to four orders of magnitude lower than the initial value. After coalescence, the large vesicle distances may allow a secondary build-up of H_2O supersaturation in the melt volume between vesicles during ongoing decompression. This may enable a secondary vesicle formation at the remaining lower H_2O content in the interstitial melt, resulting in a bimodal size distribution of vesicles in erupted products, also consistent with observations on natural samples (Gurioli et al. 2005).

Study II concludes that the initial *VND* in phonolitic melts is possibly formed by spinodal decomposition and depends on c_{H2Oini}. However, the *VND* finally observed in volcanic products of melts with high c_{H2Oini} is likely to be influenced by early-formed vesicles due to heterogeneous nucleation on crystal surfaces at magmatic sub-liquidus temperatures and obscured by coarsening processes, as well as secondary vesicle formation. Besides c_{H2Oini}, the resulting vesicle textures may depend on the available timescale, e.g., decompression rate before eruption and cooling.

In addition to the *VND* as an important parameter for silicate melt degassing, the porosity and concentrations of dissolved H_2O are crucial measures to interpret the degassing behavior. The glass porosity of decompressed samples that are quenched to glass for analysis, has usually been assumed to represent the melt porosity just before quenching. The glass porosity is compared to the expected equilibrium porosity in order to distinguish between equilibrium and disequilibrium degassing. A large discrepancy between equilibrium porosity and observed glass porosity is therefore often interpreted as disequilibrium degassing. However, it has been shown that vesicles may shrink during isobaric cooling induced by two processes. The molar volume of H_2O within the vesicles decreases during cooling, dictated by the equation of state of H_2O (Marxer et al. 2015). Furthermore, the H_2O solubility at constant pressure increases with decreasing temperature (at P < 300 MPa; Holtz et al. 1995; Schmidt and Behrens 2008) which can cause resorption of H_2O from the fluid vesicles back

into the melt (McIntosh et al. 2014; Ryan et al. 2015). These processes decrease porosity and increase H_2O concentration in the melt around vesicles during cooling until the melt is quenched to glass. The resulting glass porosity and H_2O concentration of the vitreous samples may not necessarily represent the molten state of the samples before cooling. This may lead to an underestimation of melt porosity and overestimation of the H_2O concentration dissolved in the melt when vesicle textures are examined in rapidly cooled glassy samples.

Study III (Allabar et al. 2020b) of this work addresses this experimental problem and shows, on the basis of the data from Study I and Study II, that vesicles significantly shrank during cooling before samples were analyzed. Despite a large discrepancy between equilibrium porosity and observed glass porosity, it was shown that the hydrous phonolitic melts must have undergone near-equilibrium degassing during decompression after vesicle formation and before cooling. Vesicle shrinkage was quantified and it was demonstrated that the extent of vesicle shrinkage depends on the cooling rate. H_2O resorption during cooling was verified by quantitative Raman micro-spectroscopy mapping that shows increased H_2O concentrations in the glass around vesicles. This result was confirmed by H_2O concentration mapping with attenuated total reflection FTIR micro-spectroscopy coupled to a focal plane array detector, the application of which is novel in this research area. Furthermore, new methods were developed to enable determination of the temperature at which vesicle shrinkage during cooling stops, helping to correct porosity data with respect to cooling induced vesicle shrinkage in samples that are quenched for analysis.

The findings of study III were extended to literature data from previously published decompression experiments with phonolitic melt for which vesicle shrinkage during cooling has not been considered before. The possibility of vesicle shrinkage in these experiments indicated that previous interpretations of decompression experiment data may need revision. The study highlights the importance to account for possible vesicle shrinkage during cooling, including the prospect to other melt compositions, in order to correctly interpret experimental results and to handle their applicability to natural volcanic systems in a sound manner.

In summary, this work is another step towards a better understanding of dynamic volcanic processes that lead to explosive volcanic eruptions. The presented results are indications for phase separation by spinodal decomposition in hydrous phonolitic melts.

Besides nucleation theory, spinodal decomposition may in general be considered as phase separation mechanism in silicate melts (Sahagian and Carley 2020). However, a proof and thermodynamic models are still lacking. Future studies may investigate the vesicle formation mechanisms in melts with phonolitic and other melt compositions experimentally or on a theoretical basis. Although very challenging, in-situ experiments at high pressure and temperature may provide evidence for a certain phase separation mechanism.

Study III of this thesis contributes to the improvement of the experimental and analytical procedure when quenched samples are used to study inaccessible high pressure and high temperature volcanic processes. While the calculations presented are semi-quantitative and apply to samples with a straightforward degassing and cooling path, natural volcanic ejecta undergo more complex degassing and cooling histories. Thus, for the correct interpretation of natural samples or samples from more complex experimental protocols, in-situ experiments and numerical models (Llewellin et al. 2019) will enable the quantification of vesicle shrinkage and H_2O resorption.

I. Message in a bottle: Spontaneous phase separation of hydrous Vesuvius melt even at low decompression rates

A. Allabar and M. Nowak

Abstract

Violent explosive volcanic eruptions are destructive and threaten millions of people and infrastructure. Ejected ash, pumice and gases are end-products of volcanic factories sourced deep within magma chambers and conduits. The different production stages are not directly observable. However, experimental simulation reveals different stages of dynamic volcanic processes. The starting point of explosive volcanic eruptions is determined by the phase separation of an H_2O fluid from a supersaturated hydrous silicate melt. The number of formed H_2O fluid vesicles per unit volume of silicate melt (*VND*) is a basic property that controls the efficiency of fluid–melt separation, ascent velocity and finally explosive volcanism. We performed decompression experiments at superliquidus temperatures to simulate phase separation of a single phase hydrous silicate melt during ascent with AD79 Vesuvius white pumice composition using decompression rates of 0.024–1.7 $MPa \cdot s^{-1}$. The white pumice buried Herculaneum and Pompeii and is representative of other catastrophic phonolitic and trachytic explosive eruptions like the violent 39 ka Campi Flegrei and the 1815 AD Tambora eruption. Here we report a high log*VND* of 5.2 (in mm^{-3}) that is independent from decompression rate within the investigated range. Even at a decompression rate of 0.024 $MPa \cdot s^{-1}$ the formation of a high *VND* inevitably causes rapid degassing due to short H_2O diffusion distances from the melt into fluid vesicles. A decompression rate meter based on nucleation theory, which is commonly used to estimate magma ascent velocity during volcanic eruptions using *VND* of volcanic ejecta, cannot be adapted to explain our experimentally determined decompression rate independent *VND*. Alternatively, decompression-induced H_2O–silicate melt phase separation may be described by diffusion controlled spinodal decomposition where maximum supersaturation is reached. This process occurs spontaneously and free of activation energy if hydrous melt is driven into thermodynamic instability where the second derivative of free energy of mixing to the H_2O content is ≤ 0. However, the decompression rate independent *VND* has profound consequences for the dynamics of natural polyphase hydrous magma phase separation. Even at low ascent rates spontaneous hydrous melt phase separation facilitates rapid density decrease accompanied by sudden increase of magma buoyancy triggering explosive eruptions.

1. Introduction

Violent explosive volcanic eruptions that ejected in the past up to thousand km^3 magma, like Vesuvius (AD79; ~3 km^3; Cioni et al. 2008) Tambora (1815; 100 km^3) and Campi Flegrei (36 ka; 100–200 km^3) are extremely destructive (e.g., Miller and Wark 2008). Actually, potentially explosive volcanic systems threaten millions of people and infrastructure. The ejecta composed of ash, pumice and gases are end products of volcanic systems rooted deep within magma chambers and conduits. The dynamic processes in the Earth's interior prior and during eruptions are not directly observable. However, experimental simulation provides access to different stages of complex dynamic volcanic processes. During magma ascent the solubility of H_2O, the most important volatile component dissolved in magma, decreases with decreasing pressure (P) (e.g., Iacono-Marziano et al. 2007). Increasing supersaturation of hydrous silicate melt leads to phase separation of an H_2O fluid, an important prerequisite to initiate explosive volcanism (e.g., Gonnermann and Manga, 2007). The resulting vesicularity is described by the vesicle number density (number of vesicles per unit volume of silicate melt, *VND*) and porosity Φ. Previous experimental degassing studies of e.g., rhyolite (e.g., Hamada et al. 2010; Mourtada-Bonnefoi and Laporte 2004; Gardner et al. 1999) report a strong increase of *VND* with decompression rate (dP/dt). One order of magnitude increase in decompression rate causes an increase of *VND* by 1.6 log units, such that the *VND* of natural volcanic ejecta is commonly used to reconstruct the ascent velocity of a magma by using calculations based on nucleation theory (e.g., Toramaru 2006).

First superliquidus decompression experiments with Vesuvius white pumice phonolite (VAD79) that buried Herculaneum and Pompeii, representative of other catastrophic phonolitic and trachytic explosive eruptions like the violent 39 ka Campi Flegrei (e.g., Mastrolorenzo et al. 2001) and the 1815 AD Tambora eruption (Foden 1986), have been conducted by Iacono-Marziano et al. (2007). They have shown that the experimental investigation of hydrous melt phase separation at low decompression rates is limited by the capsule size due to diffusional loss of H_2O towards heterogeneously nucleated vesicles at the capsule-melt interface (fringe vesicles) early formed at low supersaturation during decompression. In the central part of the samples they observed a high log*VND* of ~5.8 (*VND* in mm^{-3}) but no clear dependence of *VND* from decompression rate ranging from 1.7–

4.6 MPa·s^{-1}. Marxer et al. (2015) found a similarly high log*VND* of 5.4 for VAD79 melt towards higher decompression rates up to 10 MPa·s^{-1}. Even at low decompression rates down to 0.17 and 0.024 MPa·s^{-1}, Preuss et al. (2016) report a high log*VND* of ~5 for VAD79 and Campanian Ignimbrite (Campi Flegrei) composition ensuring that supersaturation in the central part of the melt filled capsule was not affected by diffusional H_2O loss prior to vesicle formation.

To verify the decompression rate independency of *VND* in crystal free hydrous phonolitic melt which would be a new challenge for the interpretation of volcanic ejecta and dynamics, we extend within the frame of this study the dataset for single phase hydrous VAD79 melt with 5.3 wt% H_2O at superliquidus temperatures of 1323–1373 K to simulate phase separation during ascent using decompression rates of 0.024–1.7 MPa·s^{-1}. The experimental results are essential to understand the initial step of phase separation generating fluid vesicles within silicate melt that is followed by vesicle growth, Ostwald ripening, coalescence, percolation and magma fragmentation. The *VND* controls the efficiency of diffusion controlled degassing of hydrous silicate melt. This is the basic production stage of the volcanic factory and a prerequisite to gain detailed insight into the degassing behavior of natural magma that usually is composed of hydrous silicate melt, crystals and possibly pre-existing fluid vesicles prior to ascent and explosive volcanic eruptions. The understanding of homogeneous phase separation is one important part for computational modeling of volcanic activity and finally for risk assessment of potentially explosive volcanic systems.

2. Methods

2.1 Starting material and capsule preparation

A crystal free VAD79 glass was synthesized following the protocol of Marxer et al. (2015) with additional improvement of the final cooling step: The melt was air cooled from 1873 K to a temperature nearby the glass transition (T_g) within ~1 min to inhibit crystallization. Then the supercooled melt was transferred into a furnace preheated to 833 K, whereupon the furnace was switched off to maintain a cooling rate of ~5 K·min^{-1} to room temperature, which successfully minimized tension-induced crack formation within the glass batch.

Cylinders with 5 mm diameter were drilled out of the glass, cut to 6.5 mm length and ground at the edges to prevent capsule damage during pressurization. One cylinder was

embedded in epoxy resin and ground and polished for electron microprobe analysis (EMPA). Successful homogenization of the anhydrous glass was confirmed by the EMPA using measurement conditions as described in Preuss et al. (2016) (SiO_2: 57.24%; TiO_2: 0.29%; Al_2O_3: 21.08%; FeO: 2.71%; MnO: 0.15%; MgO: 0.39%; CaO: 3.19%; Na_2O: 5.38%; K_2O: 9.47%; P_2O_5: 0.1%). Porosity of the glass cylinders that is caused by some air vesicles enclosed during synthesis was determined with a pycnometer to ensure values < 6% prior to hydration (Preuss et al. 2016). Annealed Au80Pd20 capsules (13 mm initial tube length, OD: 5.4 mm, ID: 5.0 mm) were closed with Au80Pd20 lids at the bottom. For slightly H_2O undersaturated conditions prior to decompression (Iacono-Marziano et al. 2007), the glass cylinders were loaded together with 5.3 wt% H_2O into the capsules which were then crimped to a three-sided star at the top and welded shut. Possible leakage was checked by re-weighing of the bottle-shaped capsules after heating to 383 K and again after a pressure test at 100 MPa water pressure and room temperature.

2.2 Decompression experiments

Combined hydration and decompression experiments were conducted in an internally heated argon pressure vessel (IHPV) equipped with a rapid quench setup and a piezo-actuator driven high-pressure valve that facilitates continuous decompression (Nowak et al. 2011). The samples were equilibrated at 200 MPa and 1523 K for 96 h at an intrinsic oxygen fugacity close to ΔlogQFM = +3.5 (Berndt et al. 2002). After hydration the run temperatures were reduced isobarically to 1373 and 1323 K, still above the liquidus and slightly H_2O undersaturated (Iacono-Marziano et al. 2007; Marxer et al. 2015), and held for 0.5 h to thermally equilibrate the samples before decompression. Then the hydrous melts were decompressed isothermally at decompression rates of 0.024–1.7 $MPa \cdot s^{-1}$ to induce H_2O supersaturation that is required for homogeneous phase separation at a supersaturation pressure ΔP_{hom}. At final pressures (P_{final}) of 110–70 MPa the samples were quenched isobarically with ~150 $K \cdot s^{-1}$ (Berndt et al. 2002) to room temperature, extracted from the IHPV and re-weighed to test for possible leakage.

To ensure the absence of crystals after hydration prior to decompression, VAD79 samples from the study of Marxer et al. (2015) with 2.5 mm capsule diameter (Ref02-Ref08) that were hydrated at 1323 K, 200–75 MPa and quenched without decompression were re-examined with transmitted light microscopy (TLM, 1000× magnification). Compared to the

5 mm diameter samples from Preuss et al. (2016) that contain small objects of ~1 µm in the glass, the 2.5 mm samples are free of objects down to the limit of optical resolution. This supports the assumption that the small objects in 5 mm samples are quench-crystals that have formed due to slightly slower cooling of larger samples and that the hydrous melt is crystal free prior to decompression (Preuss et al. 2016).

The air vesicles enclosed during glass synthesis and the air enclosed in the free volume of the capsules after preparation completely dissolves in the melt during hydration at slightly H_2O undersaturated conditions (for details see Preuss et al. 2016). Thus, the phase separation of the hydrous melt starts from a single phase.

2.3 Sample preparation

The decompressed sample capsules were cut along the cylinder axis. One half was prepared for SEM. The other half was prepared to a double-sided polished cantilever thin section (100–250 µm thickness) for FTIR spectroscopy and TLM analysis.

2.4 FTIR spectroscopy

Total H_2O contents (c_{H2O}) of the decompressed samples were analyzed with a Bruker Vertex v80 FTIR-spectrometer connected to a Hyperion 3000 IR-microscope in the near infrared (NIR) using a CaF_2 beam splitter, a tungsten light source and an InSb single element detector, a 15× Cassegrain objective and a knife-edge aperture which was set to 50×50 µm. The samples were analyzed in transmission mode with 50 scans, with a spectral resolution of 4 cm^{-1} and air as reference. Total H_2O contents were determined from molecular H_2O absorbance at ~5210 cm^{-1} and hydroxyl absorbance at ~4470cm^{-1} following the method of Behrens et al. (1996) using the linear molar extinction coefficients from Iacono-Marziano et al. (2007) (ε_{H2O} = 1.18 and ε_{OH} = 1.14 $l \cdot mol^{-1} \cdot cm^{-1}$). Concentration profiles were monitored perpendicular and parallel to the sample cylinder axis. H_2O filled vesicles were measured together with hydrous glass in the vesicle-rich central part of the samples.

2.5 Quantitative determination of *VND* and porosity

2.5.1 Quantitative SEM image analysis

Samples with average vesicle diameters of > 5 µm were analyzed with back scattered electron (BSE) analysis. BSE images of a representative area of each sample were recorded

with a LEO 1450 VP SEM or a Hitachi TM3030plus tabletop SEM. Magnifications were adjusted individually to resolve the smallest detectable vesicle intersections. Quantitative image analysis was performed with ImageJ and CSDCorrections (Higgins 2000) as described in Marxer et al. (2015) and Preuss et al. (2016).

2.5.2 Transmitted light microscopy analysis

A Zeiss Axio Image M2M microscope was used to quantify *VND* in thin sections with vesicles that are too small for BSE image analysis. The vesicles were marked and counted in selected sample volumes (23100 $\mu m^2 \times$ sample thickness (Table I.1) at 500× and 5655 $\mu m^2 \times$ sample thickness at 1000× magnification) with the Fission Track Studio software "Trackworks". The number of vesicles in the analyzed volumes were normalized to the amount of vesicles per mm^3 sample volume. Vesicle diameters were determined with the software provided measurement tool and used to calculate porosities and the *VND* normalized to vesicle free glass volume of the samples.

3. Results

In the fringe zones of all decompressed vitreous samples, large fringe vesicles are observed at the capsule glass-interface. The sample decompressed to 110 MPa is free of vesicles in the center of the sample. The samples decompressed to P_{final} of ≤ 100 MPa show a vesicle free zone (Fig. I.1) between the fringe vesicles and a highly vesiculated volume in the central part of the capsule (Figs. I.2 and I.3).

The size of the central vesiculated volume of the sample cylinders decreases with decreasing decompression rate (Fig. I.2). Additional larger vesicles appear in the lower part of the sample decompressed with 0.064 $MPa \cdot s^{-1}$ (CD92) and their number and extent increase with lower decompression rate such that only a small volume in the central part of the 0.024 $MPa \cdot s^{-1}$ sample (CD77) is vesiculated. The widths of the vesicle free zones range from ~800 µm in CD92 (0.064 $MPa \cdot s^{-1}$) and ~500 µm in CD63 and CD39 (Fig. I.3; 0.17 $MPa \cdot s^{-1}$) to ~150 µm in CD78 (1.7 $MPa \cdot s^{-1}$).

After decompression to P_{final} of ≤ 100 MPa the central parts of the samples show homogeneously dispersed and nearly uniformly-sized vesicles (Fig. I.4) with similar log*VND*s of 5.2 ± 0.25, irrespective of the decompression rate (Table I.1). These values are slightly lower compared to the results of Iacono-Marziano et al. (2007) (5.8) and within error

identical to data of Preuss et al. (2016) (5.1) and Marxer et al. (2015) (5.4) (Table I.1). The error ± 0.25 in log*VND* of our experiments was estimated by multiple TLM analysis of CD40 and multiple BSE image analysis of sample CD50. Both samples decompressed at 1373K reveal within error the same *VND*. The duplicated experiments (CD39 and CD63, Table I.1) confirm the experimental reproducibility. In the samples decompressed with 1.7–0.064 MPa·s^{-1} the H_2O contents in the central part of the vesiculated glass cylinders (H_2O dissolved in glass together with H_2O in fluid vesicles) correspond within error (~± 0.2 wt%) to the initial c_{H2O}. The glass porosities at a P_{final} of 80MPa are similar between 3–7%, irrespective of decompression rate. In sample CD77 decompressed with 0.024 MPa·s^{-1}, c_{H2O} is decreased in the central part to 4.7 wt% (Fig. I.5, Table I.1) and the glass porosity is < 0.1%.

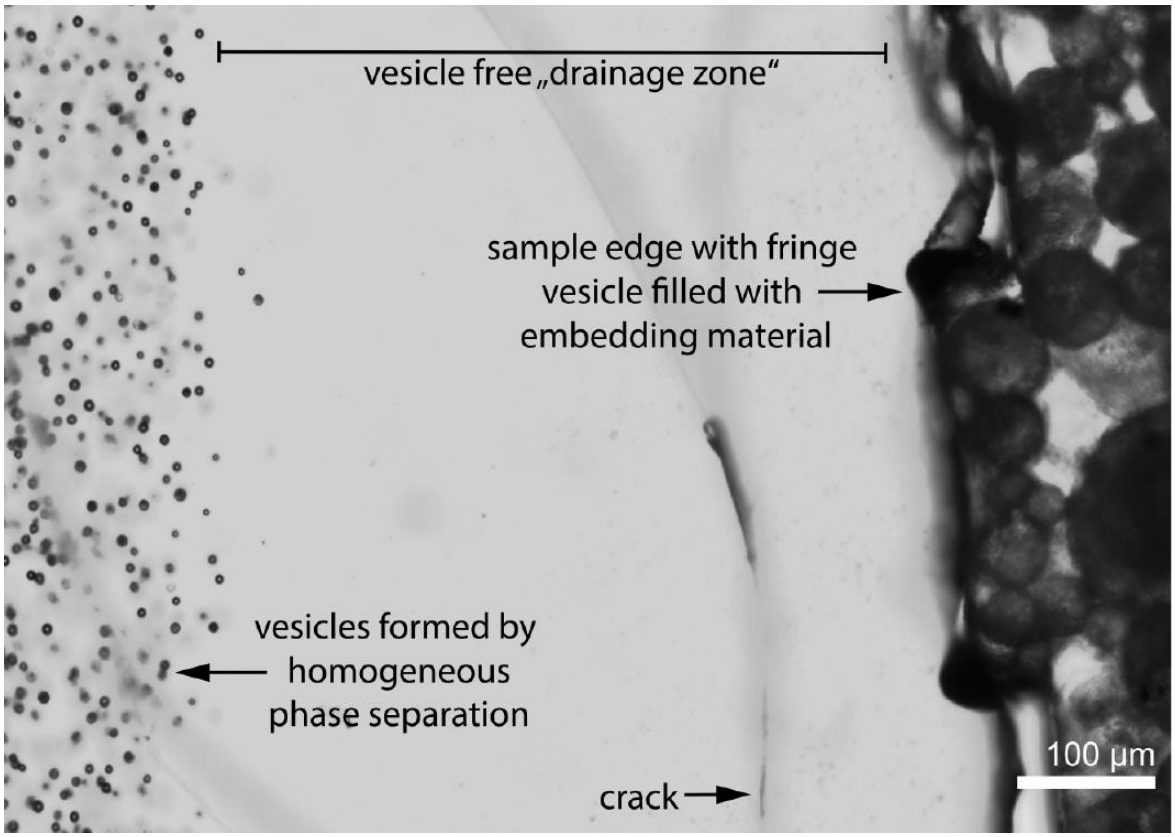

Fig. I.1 TLM image of CD39 (0.17 MPa·s^{-1}, P_{final} = 80 MPa) cantilever thin section sample edge showing the transition from a vesiculated sample core formed by homogeneous phase separation (left side) to a vesicle free drainage zone. At the sample edge fringe vesicles are hardly visible as they are filled with embedding material of the cantilever thin section.

Table I.1 Conditions and results of isothermal decompression experiments started from 200 MPa.

#	T [K]	dP/dt [MPa·s^{-1}]	P_{final} [MPa]	c_{H2O} [a] [wt%]	glass porosity [%]	equilibrium porosity [b] at P_{final} prior to quench [%]	thickness of thin section analyzed with FTIR and TLM [mm]	VND [c] [mm^{-3}]	log VND
this study:									
CD78	1323	1.7	82	5.12(0.09)	3	25	0.208	$2.11 \cdot 10^{5}$ [d,e]	5.32
CD48	1323	0.17	110	5.37(0.06)	-	-	0.104	-	-
CD40	1323	0.17	100	5.17(0.05)	< 0.1	18	0.223	$1.40E \cdot 10^{5}$ [e]	5.15
CD39	1323	0.17	80	4.97(0.13)	5	26	0.102	$1.49E \cdot 10^{5}$ [d]	5.17
CD63	1323	0.17	80	5.09(0.10)	7	26	0.218	$1.74E \cdot 10^{5}$ [d]	5.24
CD50	1323	0.17	70	5.38(0.16)	13	32	0.243	$6.70E \cdot 10^{4}$ [d]	4.83
CD92	1323	0.064	80	5.10(0.09)	5	26	0.222	$2.25E \cdot 10^{5}$ [d]	5.35
CD77	1323	0.024	80	4.71(0.03)[f]	< 0.1	21[g]	0.218	$2.45E \cdot 10^{5}$ [e]	5.39
CD51	1373	1.7	75	5.25(0.11)	3	30	0.214	$9.58E \cdot 10^{4}$ [d,e]	4.98
CD53	1373	0.17	80	5.17(0.06)	2	27	0.239	$8.92E \cdot 10^{5}$ [d]	4.95
Experiments from previous studies that fulfill the experimental protocol of Preuss et al. (2016):									
CD-C-23[P]	1323	0.17	100	4.83(0.06)	< 0.1			$1.01 \cdot 10^{5}$	5
CD-C-25[P]	1323	0.024	100	4.68(0.05)	< 0.1			$1.30 \cdot 10^{5}$	5.11
SSD06[Ma]h	1323	10	75	5.38(0.15)[i]	15		0.206	$2.57 \cdot 10^{5}$ [j,d]	5.41
B72[IM]	1323	4.63	75	5.22(0.35)[k]	6			$7.71 \cdot 10^{5}$	5.89
B74[IM]	1323	1.69	70	5.09(0.50)[k]	5			$5.65 \cdot 10^{5}$	5.75

[P]: Preuss et al. (2016); [Ma]: Marxer et al. (2015); [IM]: Iacono-Marziano et al. (2007); a: near infrared measurements in vesiculated area with H_2O vesicles in probed sample volume except of vesicle free sample CD48; ±1σ standard deviation in brackets b: calculated after Gardner et al. (1999) c: *VND* normalized to 1 mm^3 of vesicle free glass d: *VND* determined by back scattered electron (BSE) image analysis with 2D-3D conversion (detailed method description in Preuss et al. 2016) e: *VND* determined using transmitted light microscopy (detailed method description in Preuss et al. 2016) f: slightly decreased H_2O content in the central part of the sample, due to diffusional loss towards heterogeneously nucleated vesicles at capsule walls during decompression g: calculated for residual 4.7 wt% H_2O in the capsule center h: single step decompression with subsequent dwell time of 61 s at P_{final} prior to quench i: sample from Marxer et al. (2015) analyzed for this publication j: re-determined for this publication with higher back scattered electron image resolution k: total H_2O content determined by electron microprobe "by-difference" method (Iacono-Marziano et al. 2007)

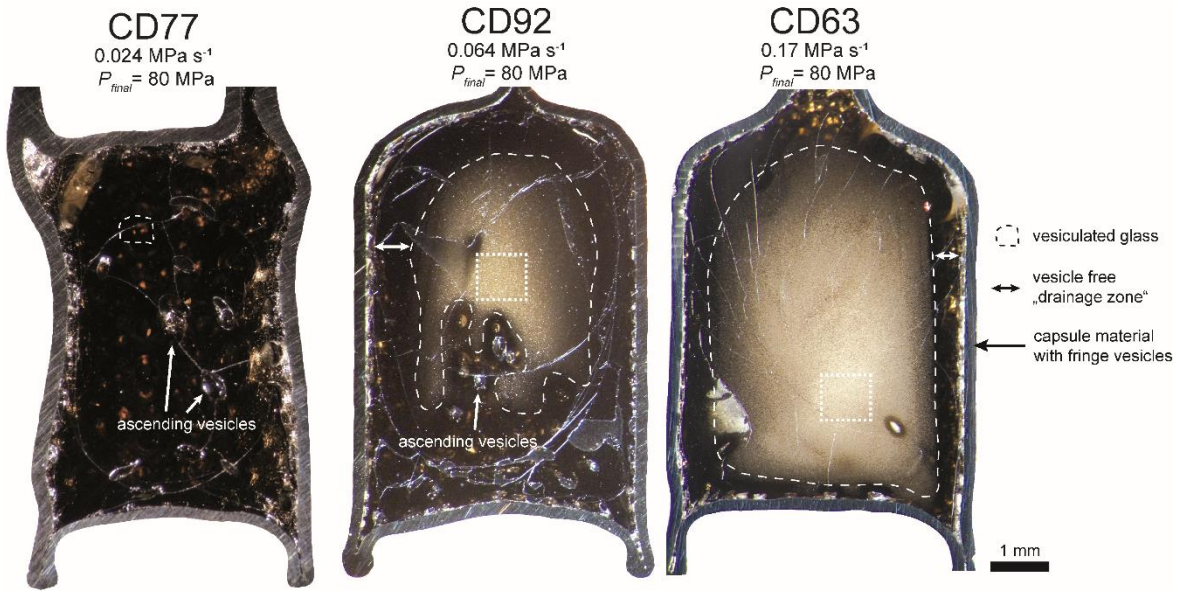

Fig. I.2 Reflected light images of samples that were cut along the cylinder axis and polished and prepared for SEM. Bright volumes in the capsule centers of CD92 and CD63 are vesiculated glasses with a log*VND* of ~5.2 ± 0.25. The gradients in brightness within the vesiculated central glasses are mainly caused by the illumination of the samples. Porosity only slightly decreases towards the rim of the vesiculated volume due to decreasing H_2O content (Fig. I.5). The vesiculated volumes are surrounded by a vesicle free H_2O depleted drainage zone and fringe vesicles are attached to the capsule wall (for explanation see text). At 0.064 MPa·s^{-1} vesicles ascended from the capsule bottom are present in the lower half of the capsule. At 0.024 MPa·s^{-1} the decompression time was long and ascending vesicles crossed the whole sample. Thus, only a small volume is observed, where homogeneous phase separation occurred. Vesicles in this sample are not visible in the reflected light image. The indicated small area in CD77 corresponds to the volume in the cantilever thin section where vesicles were observed with TLM. The dashed rectangles in CD92 and CD63 denote the areas of the zoomed images shown in Fig. I.3.

4. Discussion

The textural features of the decompressed phonolitic samples are snapshots taken at P_{final} just prior to quench. The fringe vesicles attached to the capsule walls are interpreted as heterogeneously nucleated at a low supersaturation pressure ($\Delta P_{het} << \Delta P_{hom}$) due to reduced surface energy at the capsule-melt interface (e.g., Iacono-Marziano et al. 2007). The vesicle free zone with depleted H_2O content towards the capsule walls is formed due to diffusional loss of H_2O into the fringe vesicles during decompression before homogeneous phase separation occurs in the central part of the capsule. Thus, the vesicle free zone is further referred to as drainage zone (Preuss et al. 2016). The size of the vesiculated volume, which is formed by homogeneous phase separation in the central part of the sample, decreases with

lower decompression rate due to the increasing time given for diffusional H_2O loss from the melt into fringe vesicles. We interpret the large vesicles in the lower part of the sample which appear in experiments decompressed with rates < 0.17 MPa·s^{-1} as fringe vesicles, that detached from the capsule bottom by buoyancy driven ascent during further decompression. Besides diffusional loss of H_2O in the drainage zone, these ascending vesicles define an additional limiting factor for experiments at low decompression rates because H_2O diffuses from the melt into such ascending vesicles. Thus, the H_2O content in the central part of the capsule is reduced faster than estimated solely via H_2O diffusion towards the capsule–melt interface into fringe vesicles prior to homogeneous phase separation. The decompression rate of 0.024 MPa·s^{-1} defines the experimental limit to study homogeneous phase separation at our experimental conditions because c_{H2O} in the central part of the sample CD77 is already decreased from initial 5.3 to ~4.7 wt%. Nevertheless, the H_2O loss was low enough to ensure homogeneous phase separation within a small sample volume (Fig. I.2) presumably at $P < 100$ MPa.

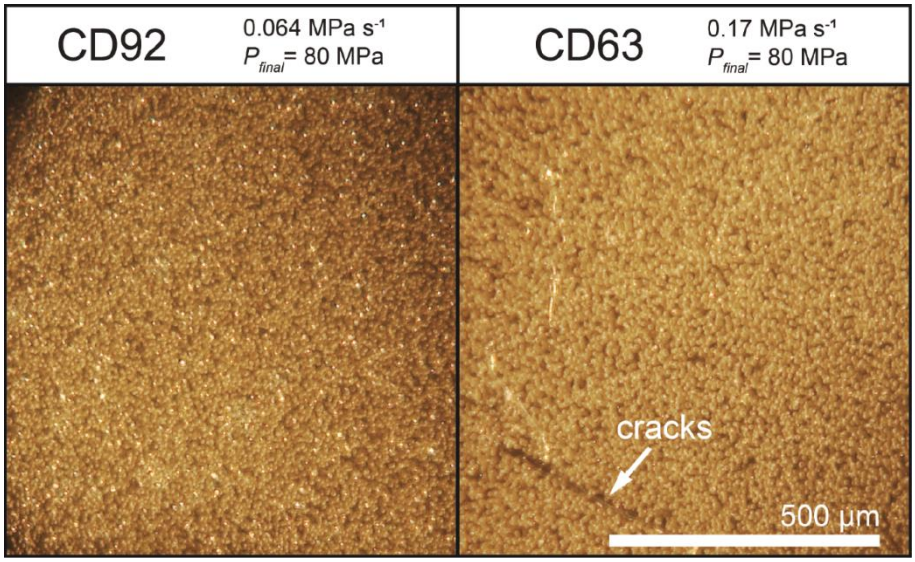

Fig. I.3 Microscope images of the central vesiculated volumes of the samples CD92 and CD63. Positions within the samples are marked in the overview images (Fig. I.2). The images and data analysis show that porosities and *VND* of the vesiculated volumes are similar in samples decompressed with different rates and identical P_{final} (Table I.1).

The absence of vesicles in the central part of the sample decompressed with 0.17 MPa·s^{-1} and quenched at 110 MPa (CD48) suggests that homogeneous phase separation occurred within a small pressure interval between 110 and 100 MPa followed by vesicle growth without any change in *VND* during further decompression to 70 MPa (Table I.1).

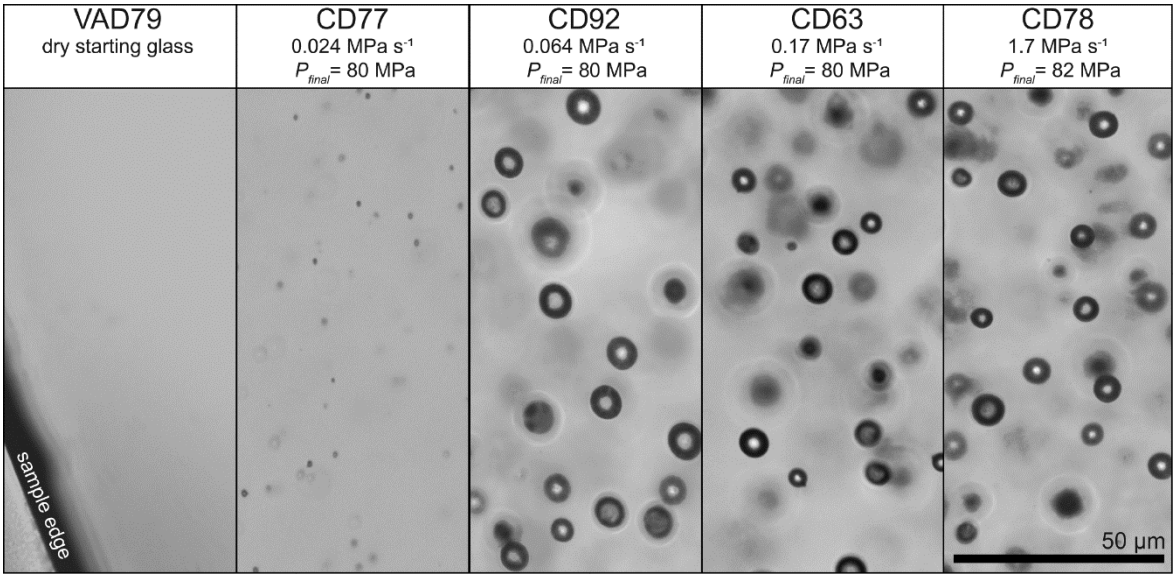

Fig. I.4 Transmitted light microscopy images of dry VAD79 starting glass and hydrous Vesuvius melt decompressed with four different decompression rates and quenched to glass at similar final pressures. The starting glass is free of vesicles and crystals. In hydrated and subsequently decompressed samples, vesicles are homogeneously dispersed and vesicle number densities are equal within error in all four samples. Vesicles in samples decompressed with ≥ 0.064 MPa·s^{-1} are nearly uniformly-sized and revealing similar porosities (Table I.1). The bright haloes visible around the vesicles out of focus are an optical effect (Becke line). The sample decompressed with 0.024 MPa·s^{-1} has a significantly lower porosity due to diffusional loss of H_2O into fringe vesicles during long decompression time before homogeneous phase separation occurred. The scale bar is valid for all images.

For the mean log*VND* of 5.2, we calculated a mean-vesicle distance (x) of ~10 µm after Hertz (1908) ($x = 5/9 \cdot VND^{-1/3}$) for random vesicle distribution. This inter-vesicle distance is small enough to adjust near-equilibrium c_{H2O} and thus near-equilibrium porosity within seconds by H_2O diffusion during further decompression, estimated using the H_2O diffusivity D_{H2O} given in Fanara et al. (2013). Thus, H_2O super-saturation in the melt cannot evolve during further decompression to form additional vesicles. Prior to quench, near-equilibrium porosity was present in all samples in which homogeneous phase separation occurred. In this case, the melts containing initially 5.3 wt% H_2O in the central part of the samples that were de-compressed with different rates had the same porosity of ~26% prior to isobaric quench at 80 MPa (calculated after Gardner et al. 1999) (Table I.1). During quench the vesicles shrink due to (1) the decrease of molar volume (V_m) of H_2O (Marxer et al. 2015) and (2) H_2O resorption from fluid vesicles into the melt during cooling (McIntosh et al. 2014), driven by increasing H_2O solubility in phonolitic melt with decreasing temperature at $P < 300$ MPa (Schmidt and Behrens 2008). Samples with identical melt porosity quenched at the same P_{final}

with identical cooling path result in similar glass porosities of 3–7% as observed in our 80 MPa experiments (Fig. I.4, Table I.1). Modeling of vesicle shrinkage during cooling is complex because of decreasing H_2O diffusivity and increasing melt viscosity. However, as first approximation it can be assumed that vesicle shrinkage is facilitated down to T_g as suggested by Marxer et al. (2015). The porosity of the melts quenched at 80 MPa is decreased from equilibrium porosity (~26%) to 10% by the decrease of V_m of H_2O. The remaining difference to the observed glass porosities is attributed to resorption shrinkage. However, this process does not affect the total H_2O content of the central vesiculated parts of the samples (the sum of H_2O in vesicles and in hydrous glass). The low glass porosity of < 0.1% of the sample decompressed with 0.024 MPa·s^{-1} to 80 MPa (CD77) is attributed to diffusional H_2O loss even in the central part of the melt towards the capsule melt interface into fringe vesicles and ascending vesicles during decompression.

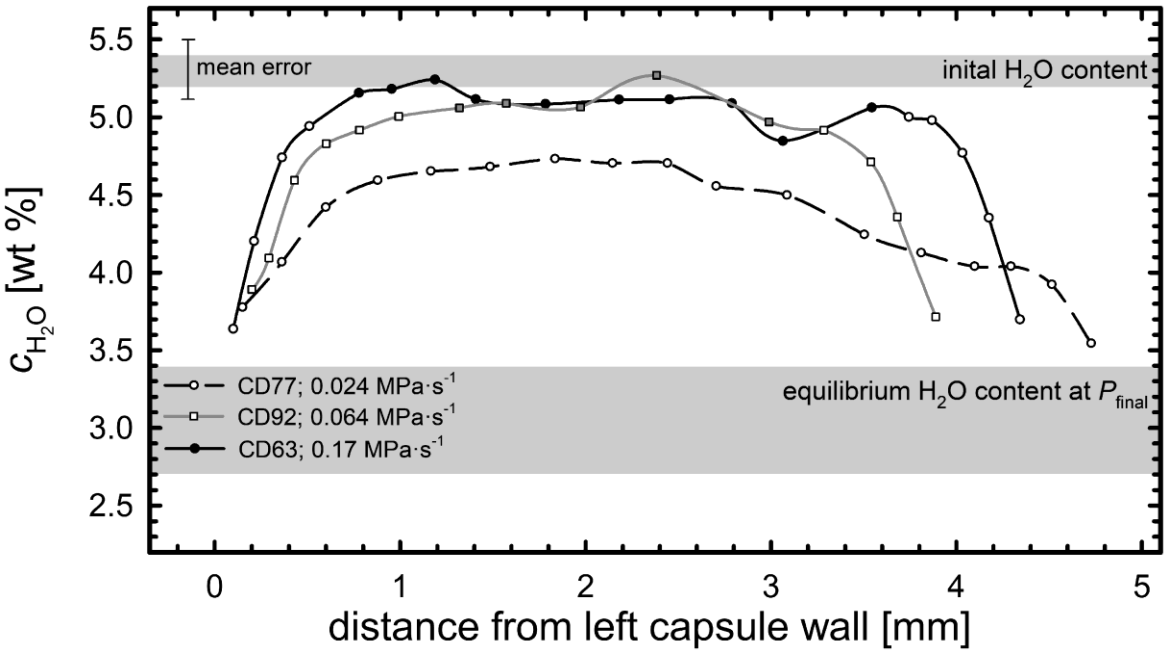

Fig. I.5 c_{H2O} profiles measured with FTIR from left to right sample edge in three samples decompressed with different decompression rates to a P_{final} of 80 MPa. Grey bars indicate initial H_2O content and equilibrium H_2O content at P_{final} (80 MPa) according to solubility experiments considering analytical error (Iacono-Marziano et al. 2007). The mean error of FTIR determined c_{H2O} is defined by error in sample thickness, density and peak height, assuming that extinction coefficients from Iacono-Marziano et al. (2007) are free of error. Filled symbols represent measurements with vesicles in the beam path, open symbols indicate measurements in the vesicle free drainage zone.

4.1 Estimation of ΔP_{hom}

Vesicle shrinkage during isobaric sample quench may lead to complete dissolution or shrinkage of vesicles below the TLM resolution limit. Thus, it is difficult to extract ΔP_{hom} that is required for homogeneous phase separation. However, to estimate ΔP_{hom}, the width of the drainage zones can be used to estimate the time that is necessary to create the H_2O diffusion profile length defined by the width of the drainage zone. Using D_{H2O} ($1.89 \cdot 10^{-10}$ $m^2 \cdot s^{-1}$, for 5.3 wt% H_2O and 1323 K) calculated after Fanara et al. (2013), we calculate the diffusion time $t = x^2/2D_{H2O}$, where x is the drainage zone width. Via the decompression rate we calculated the pressure at which phase separation occurred. This results in ΔP_{hom}'s of ~110, 115 and 100 MPa for 0.064, 0.17 and 1.7 $MPa \cdot s^{-1}$, respectively. Although this calculation is a rough estimate it shows, that homogeneous phase separation occurred at a similar ΔP_{hom} as derived from the experimental dataset with a decompression rate of 0.17 $MPa \cdot s^{-1}$.

4.2 Phase separation mechanism

4.2.3 Homogeneous nucleation

To date, phase separation of supersaturated hydrous silicate melt is described by nucleation theory (e.g., Navon and Lyakhovsky 1998), that is applicable for melts in the metastable state below the binode. For a schematic illustration we calculated a simplified isothermal binary phase diagram (silicate melt–H_2O) for a symmetric regular solution model normalized to the critical pressure (Fig. I.6). In the mechanical equilibrium approach of homogeneous nucleation, activation energy is needed to create new interfaces of nucleated H_2O vesicles in silicate melt by compositional fluctuations with large concentration differences in small volumes (Debenedetti 2000) (Fig. I.7a). At a critical vesicle radius, shrinkage or spontaneous growth occurs by condensation or vaporization of an H_2O molecule at the fluid-melt interface, respectively. The exponential increase of the nucleation rate of surviving vesicles with supersaturation pressure (difference between internal vesicle pressure and ambient melt pressure) is numerically calculated considering (1) cubed macroscopic surface tension of 0.145 $N \cdot m^{-1}$ for hydrous Vesuvius melt derived from Bagdassarov et al. (2000), (2) a pre-term that is defined by H_2O concentration (c_{H2O}) and H_2O diffusivity (Fanara et al. 2013) and (3) a correction factor to account for a steady state nucleation process rather than equilibrium (Navon and Lyakhovsky 1998).

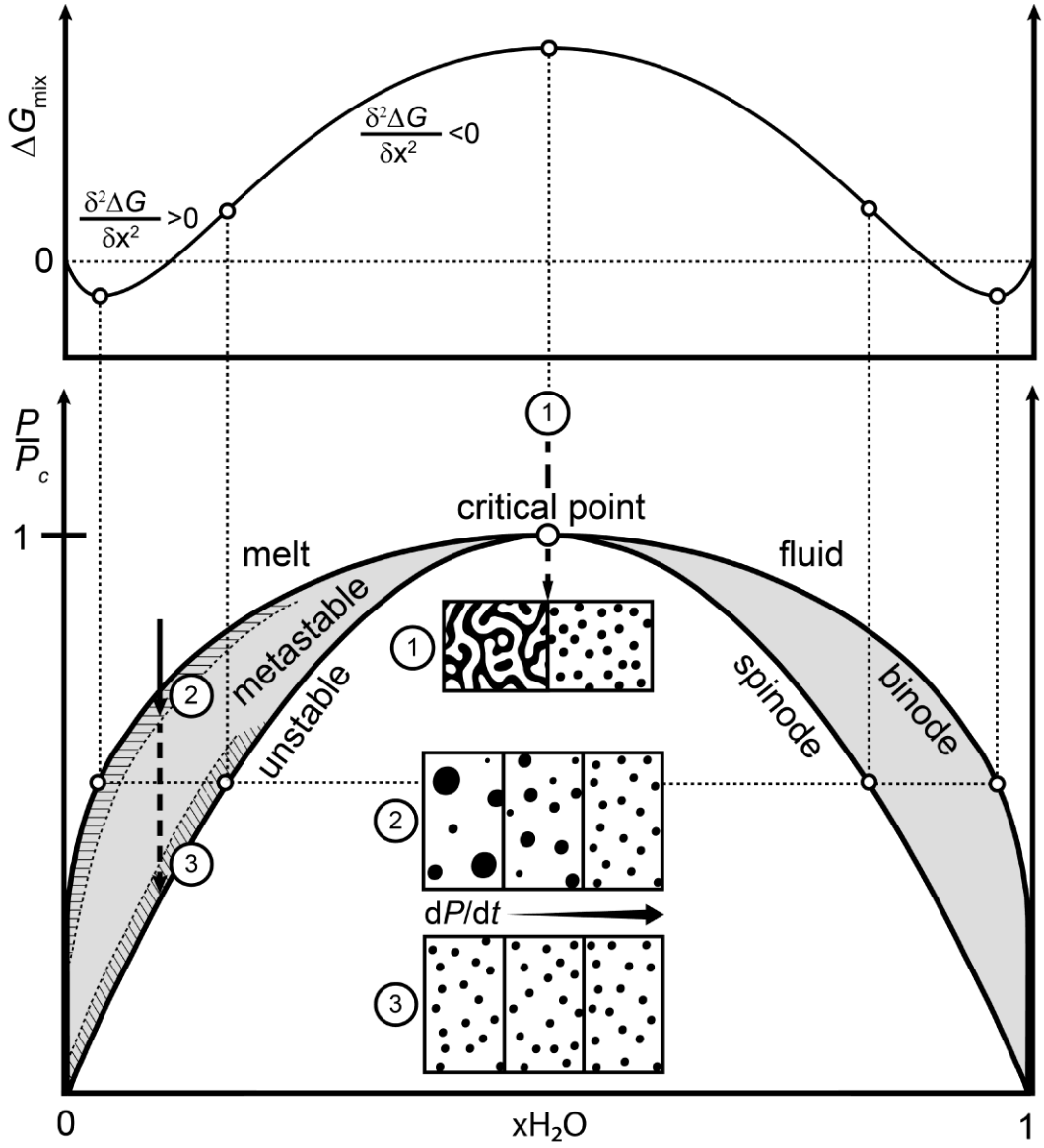

Fig. I.6 Schematic isothermal binary phase diagram calculated for a binary symmetric regular solution (Schmalzried 1981). *P* is normalized to the critical pressure (P_c) at critical composition ($x_{H2O} = 0.5$). The binode is defined by $\partial\Delta G/\partial x = 0$ and the spinode by $\partial^2\Delta G/\partial x^2 = 0$. The crosshatched fields (adapted from Binder (1984)) schematically display the regimes of nucleation (2) and spinodal decomposition (3). It has to be noted that an equation of state for the silicate melt–H_2O system is more complex but up to now not available. (1) Decompression at critical composition: At the critical point initial phase separation leads to fractal ramified structures that transform to vesicles (Zhuang and Kiran 1998); (2) off-critical composition at $x_{H2O} = 0.1$ (x_{H2O} normalized to 1 mole oxygen of anhydrous melt) equivalent to 5.3 wt% H_2O: the system is transferred into the metastable region where nucleation governed phase separation leads to decompression rate dependent *VND*s; (3) off-critical composition: the system is transferred trough the metastable region to the spinode that separates the metastable from the unstable state. Off-critical spinodal decomposition leads to uniformly-sized vesicles with a *VND* independent from decompression rate.

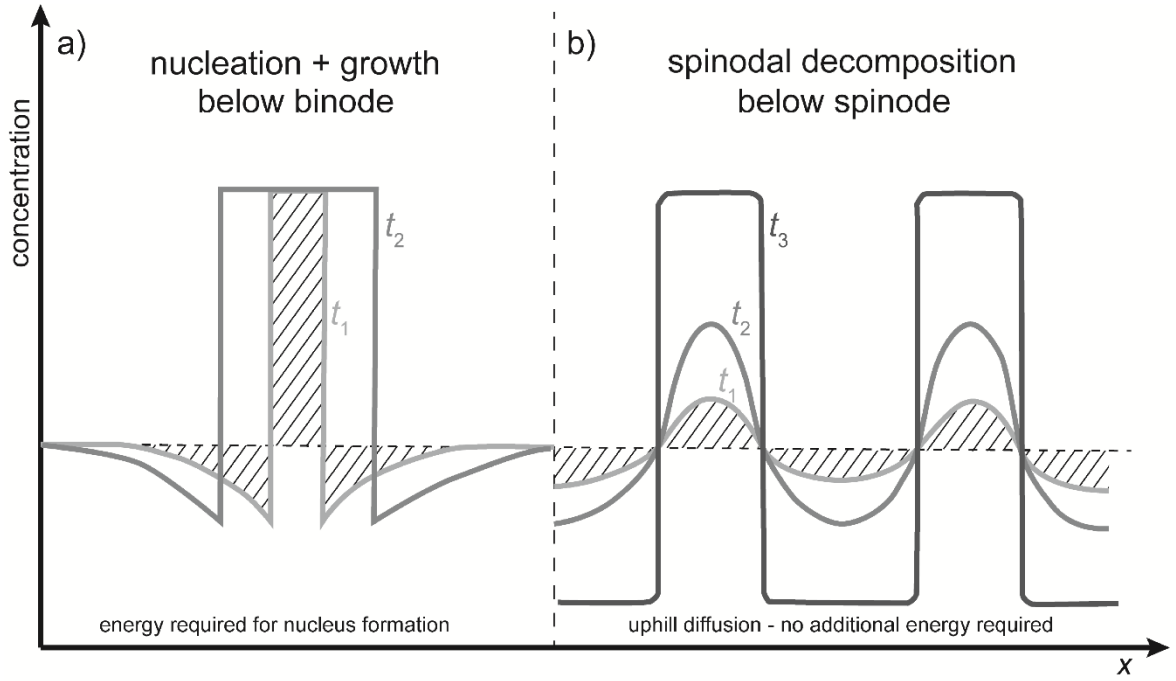

Fig. I.7 Concentration vs. distance for nucleation and growth compared to spinodal decomposition at different time steps (*t*) simplified for one dimensional treatment for a binary system (after Schmalzried, 1981, Fig. 7–13 therein). a) Nucleation and growth: activation energy is needed to create new interfaces of nucleated H_2O vesicles in silicate melt by compositional fluctuations with large concentration differences in small volumes. b) Spinodal decomposition: small concentration fluctuations lead to spontaneous uphill diffusion that lowers overall free energy. No additional energy is required.

However, nucleation theory underestimates the vesicle nucleation rate required for our experimentally observed *VND*s by several orders of magnitude, which is a well-known problem for homogeneous liquid-gas phase separation (e.g., Lubetkin 2003). Explanations for this discrepancy likely stem from the interfacial energy of a critical sized (nm scale) vesicle that might decrease significantly with supersaturation in the metastable state below the binode (Fig. I.6). This is suggested to be caused by either (1) a diffuse interface between hydrous silicate melt and H_2O clusters causing a decrease in surface tension with curvature (decreasing radius) of the critical sized vesicle (e.g., Tolman 1949; Gonnermann and Gardner 2013) or (2) a gradual change in cluster composition within a host phase at the beginning of phase separation that develops towards a second pure phase during growth (Schmelzer et al. 2004). However, an approximation to our observed *VND*s is achieved by the application of the nucleation theory based semi-empirical decompression rate meter (Toramaru 2006), which is an established method to derive magma ascent velocity using *VND*s of volcanic ejecta. With the Toramaru (2006) decompression rate meter (DRM, Equation I.1), the *VND*

as a function of decompression rate can be calculated, considering diffusivity, surface tension and the H_2O content via the saturation pressure. The model considers that every H_2O molecule represents a possible vesicle nucleation site and that during decompression the nucleation stops at a *VND* where vesicle distances are sufficiently small for a diffusion controlled decrease of H_2O supersaturation (Toramaru 2006).

$$VND = 34 \cdot C * \left(\frac{16 \cdot \pi \cdot \sigma^3}{3 \cdot k \cdot T \cdot P_w^2}\right)^{-2} \cdot \left(\frac{V_m \cdot P_w}{k \cdot T}\right)^{-\frac{1}{4}} \cdot \left(\frac{P_w^2 \cdot k \cdot T \cdot C \cdot D_{H2O}}{4 \cdot \sigma^2 \cdot (dP/dt)}\right)^{-\frac{3}{2}} \quad \text{(I.1)}[1]$$

C: initial total H_2O concentration (number of molecules per cubic meters [m^{-3}]); σ: surface tension of the vesicle- melt interface [$N \cdot m^{-1}$]; *T*: temperature [K]; k: Boltzmann constant ($1.38 \cdot 10^{-23}$ [$J \cdot K^{-1}$]); P_w: H_2O saturation pressure [Pa]; D_{H2O}: H_2O diffusivity in the silicate melt [$m^2 \cdot s^{-1}$]; V_m: volume of an H_2O molecule in the melt = $3 \cdot 10^{-29}$ m^3 (Burnham and Davis 1971); d*P*/d*t*: decompression rate [$Pa \cdot s^{-1}$]

Commonly, the model is used to derive the microscopic surface tension of nm-sized critical vesicles (which cannot be measured directly) using experimentally determined supersaturation pressures or nucleation rates of decompressed hydrous melts by inverting the nucleation theory (e.g., Cluzel et al. 2008; Gardner and Ketcham 2011; Shea 2017). Compared to macroscopic surface tension, a significantly reduced surface tension of 0.047 $N \cdot m^{-1}$ was calculated for homogeneous vesicle nucleation (σ_{hom}) in Vesuvius melt using Equation (13) given in Shea (2017). Using this value in the Toramaru (2006) model the trend matches our *VND* data at a decompression rate of 18 $MPa \cdot s^{-1}$ (Fig. I.8). However, the decompression rate meter inherently defines an exponential increase of *VND* with decompression rate ($\Delta \log VND / \Delta \log(dP/dt) = 1.6$). In case of homogeneous nucleation this dependency should be resolved by decompression experiments that cover 0.024 to 10 $MPa \cdot s^{-1}$, thus 3 orders of magnitude and a log*VND* within the range of 5 that defines a diffusion time scale to decrease H_2O supersaturation within seconds.

[1] Correction to original publication: In the original publication the square of P_w^2 in the third term is missing. This typo does not influence the results. For all calculations the correct equation was used.

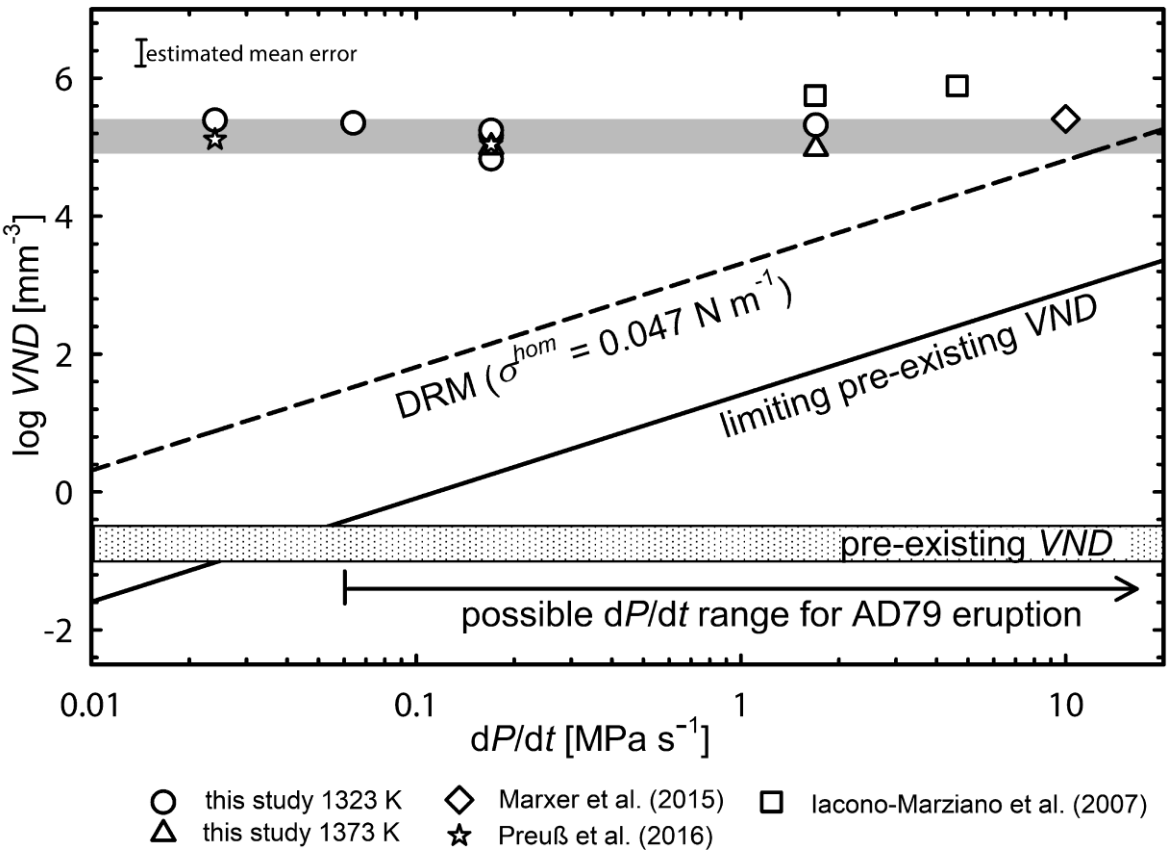

Fig. I.8 Vesicle number density vs. decompression rate. The grey line indicates the trend of data from this study. Our results, extended by the VAD79 experimental data of Iacono-Marziano et al. (2007), Marxer et al. (2015) and Preuss et al. (2016) that all fulfill the strict experimental protocol of Preuss et al. (2016), reveal within error similar *VND*s irrespective of decompression rate. The dashed line shows the dependence of d*P*/d*t* on *VND* calculated with the decompression rate meter (DRM) (Toramaru 2006; Shea 2017). The solid line represents the limiting preexisting *VND* vs. d*P*/d*t*, calculated numerically for a subliquidus magma temperature of 1223 K, an H_2O supersaturation pressure of 95 MPa, which can in principle be achieved in the Vesuvius volcanic system (Shea 2017), and cubic primitive arrangement of vesicles. Random distribution of vesicles decreases mean inter vesicle distance by a factor of 5/9 (Hertz 1908). Due to random distribution, vesicle free volumina are expected to exist that are much larger than in a cubic primitive arrangement. However, we suggest that this has minor influence on our calculation but this needs further investigation. The pre-existing *VND*, represented by the dotted line, has to be below the limiting pre-existing *VND* line to preserve supersaturation required for homogeneous phase separation. This is the case for d*P*/d*t* > 0.06 MPa·s^{-1}, defining the possible d*P*/d*t* range for the ascending AD79 Vesuvius magma causing the explosive eruption.

4.2.4 Heterogeneous nucleation

Heterogeneous nucleation can be excluded as explanation for our observed independency of *VND* from decompression rate because the experiments were carried out at superliquidus conditions. If pre-existing oxide crystals would have been present prior to

decompression, surface tension for vesicle nucleation is reduced (Hurwitz and Navon 1994) as well as the concentration of possible nucleation sites that correspond to the two-dimensional concentration of H_2O molecules at the interface of crystal and melt. Vesicles would nucleate at a low ΔP_{het} due to reduced surface energy. However, a dependency of dP/dt on *VND* such as that predicted by nucleation theory is still expected (Equation I.1; Shea 2017).

The drainage zones in the experiments show that before homogeneous phase separation occurred, H_2O concentration of the melt towards the capsule melt interface was depleted. When vesicles would have heterogeneously nucleated at a ΔP_{het} of ~5 MPa, as it can be expected for the case of heterogeneous nucleation on e.g., magnetite crystals (Shea 2017), the drainage zones would be significantly narrower than observed in our experiments. The calculated drainage zone width in the case of heterogeneous nucleation would be ~100 µm at 0.17 MPa·s^{-1} or 150 µm at 0.064 MPa·s^{-1}, significantly lower than experimentally observed (~500 µm and ~800 µm, respectively). This is an additional evidence for homogeneous phase separation in the central parts of the melts decompressed to P_{final} of ≤ 100 MPa.

4.2.5 Spinodal decomposition

The nucleation theory based DRM fails to explain the observed independency of decompression rate on *VND*. An alternative homogeneous phase separation mechanism is spinodal decomposition. This phase separation mechanism is a non-activated spontaneous process at the thermodynamic limit of metastability (e.g., Debenedetti 2000; Cahn 1965; Cahn and Hillard 1959) that is defined by the spinode (Fig. I.6), where the second derivative of the free energy of mixing ΔG ($\partial^2 \Delta G/\partial x^2$) = 0 at the inflection points of the free energy curve. The theory of spinodal decomposition is used to describe lamellae formation of solid solutions like alkali feldspar (e.g., Parsons and Brown 1991) or ternary feldspars (Petrishcheva and Abart 2012) or the decomposition of super-cooled sodium silicate melt (Cahn 1965) and organic polymer mixtures (e.g., Snyder and Meakin 1983). Spinodal decomposition at critical composition, where the binode and spinode merge, produces fractal ramified structures that are subsequently transformed into droplets to minimize the interfacial energy (e.g., Zhuan and Kiran 1998). Furthermore, it has been suggested by Paillat et al. (1992) and evidenced experimentally by Shen and Keppler (1997) and Bureau and Keppler (1999) that silicate melt and H_2O are completely miscible at high P and moderate T

relevant for deep parts of subduction zones. During isochoric cooling the supercritical fluid decomposes to hydrous silicate melt and silica-rich H_2O fluid. The observed critical opalescence is attributed to spinodal phase separation at the critical point at critical pressure, temperature and composition (Cahn 1965) (Fig. I.6). Even off-critical spinodal decomposition beyond the critical composition is observed in liquid organic polymer systems (Tanaka et al. 1990). The prerequisite is quenching below the binode through the metastable state to the spinode that separates the metastable from the unstable state, resulting directly in a droplet-type morphology with homogeneously dispersed and quite uniformly-sized vesicles in a matrix (Tanaka et al. 1990; Oh and Rey 2000) as observed in our experimental products, irrespective of the decompression rate. This is also supported by computational simulations of Cahn (1965) which show that interconnected structures form when the minor phase exceeds 15 vol% and at volumes < 15% isolated structures are expected.

Similar to reaction-induced spinodal decomposition of polymer mixtures (Oh and Rey 2000; Lamorgese and Mauri 2016), phase separation of polymerized hydrous silicate melt is a reactive process. Hydroxyl groups are the dominating species in silicate melts (Nowak and Behrens 1995, 2001). A homogeneous polycondensation reaction $2T\text{-}OH_{melt} = H_2O_{melt}+T\text{-}O\text{-}T$ ($T = Si^{4+}$, Al^{3+} cations coordinated tetrahedrally by oxygen O) is required to generate molecular H_2O that separates with a small amount of silicate melt component into the fluid phase ($H_2O_{melt} = H_2O_{fluid}$). We suggest describing this as a decompression-induced polycondensation phase separation, where both reactions run simultaneously. During off-critical spinodal phase separation at the melt rich side of the system, a small but preferentially growing amplitude of droplet like spatial concentration fluctuation with a decompression rate independent wavelength varies continuously from the melt matrix into an H_2O enriched region over a large distance without a sharp phase boundary (Cahn 1965) (Fig. I.7b). The decomposition proceeds by reaction and uphill diffusion controlled amplification of concentration gradients until a sharp phase boundary between the hydrous silicate melt and the H_2O-rich fluid phase evolves (Debenedetti 2000; Tanaka et al. 1990). After decomposition, the system is moved away from the spinode towards the binode on both sides of the phase diagram where an H_2O-rich fluid coexists with a hydrous melt, in which supersaturation caused by further decompression is then reduced by H_2O diffusion into the vesicles that were formed by spinodal decomposition.

An equation of state and thus a predictive theory for phase separation of hydrous silicate melt at large supersaturations nearing an unstable state is, up to now, not available because of complex structural silicate melt properties that depend strongly on H_2O content (e.g., Mysen 2014). Thus, we have only a qualitative picture of spinodal decomposition of hydrous silicate melt. Relaxation times at the onset of spinodal decomposition are estimated to be in the range of picoseconds for liquid-gas (Debenedetti 2000), micro- to milliseconds for liquid–liquid, and seconds to hours for solid–solid phase separation (Schmalzried 1981) depending on the wavelength of compositional fluctuations. We suggest that, in the case of a supersaturated silicate melt, the wavelength is linked to the diffusivity of H_2O and the viscoelastic properties of the melt controlled by the dynamics of T-O-T bond breaking (Malfait and Halter 2008). The short time span of the initial off-critical spinodal decomposition that defines the number density of H_2O enriched regions that evolve to H_2O-rich fluid vesicles with sharp phase boundaries is the prerequisite for the observed decompression rate independency of *VND*, and an important mechanism prior to explosive eruptions.

An explanation that spinodal decomposition might be facilitated in phonolitic melt but not in rhyolitic systems, for which this independency has not been observed (e.g., Gardner et al. 1999; Mourtada-Bonnefoi and Laporte 2004; Hamada et al. 2010), could be that the location of the critical curve of silicate melt–H_2O systems is shifted to significantly lower P and *T* conditions with decreasing SiO_2 content (Bureau and Keppler 1999). Thus, the experimentally studied metaluminous phonolitic system is expected to be closer to the critical behavior than rhyolitic systems. Furthermore, asymmetric non-ideal mixing might be considered and thus, the shape of binode and spinode differ from those shown in Fig. I.6 for a regular solution model. The metastable region might be narrower and it might be more probable to transfer the system through the metastable region without homogeneous nucleation of vesicles to occur.

4.3 Implications for nature

An independency of *VND* from decompression rate has important consequences for the understanding of the phase separation mechanism and magma ascent dynamics prior to volcanic eruptions. Our superliquidus experiments document that in a single-phase hydrous phonolitic melt a decompression rate of 0.024 $MPa \cdot s^{-1}$ is sufficient to form a high log*VND* of

5.2 ± 0.25. This is comparable with the log*VND* of natural phonolitic Vesuvius pumice in the range of 5–6 (Gurioli et al. 2005), and 4–6 for trachytic Campi Flegrei ash grains and pumice (Mastrolorenzo et al. 2001). From our knowledge, vesicularity data of thephriphonolitic Tambora ash and pumice are not available. However, estimated pre-eruptive c_{H2O} is ~6 wt% (Foden 1986) and despite the larger volcanic explosivity index, the 1815 explosive eruption style is similar to the Vesuvius AD79 eruption. Thus, similar *VND*s are expected. However, textures of natural ejecta might be strongly influenced by (1) non continuous magma ascent (e.g., Nowak et al. 2011) and (2) Ostwald ripening, coalescence, percolation and open system degassing that might occur after phase separation during magma ascent and ejection (e.g., Navon and Lyakhovsky 1998).

Furthermore, a slowly ascending fluid saturated natural magma commonly contains crystals and pre-existing heterogeneously nucleated fluid vesicles. Equilibrium H_2O content is adjusted by diffusion in melt shells (dehydration shells) around pre-existing vesicles. In this case, homogeneous phase separation is exclusively facilitated in melt volumes in which sufficient supersaturation is preserved (Fig. I.9). The size of these volumes depends on an inter-play between pre-existing vesicles, decompression rate, and H_2O diffusivity. The decompression rate defines the upper limit of pre-existing *VND* at which supersaturated melt volumes are still preserved (Fig. I.8). This is exemplarily calculated for Vesuvius melt with (1) 5.3 wt% H_2O, (2) a supersaturation pressure for homogeneous phase separation of 95 MPa, as derived from our experiments, and (3) for a temperature of 1223 K which is reasonable for natural crystal bearing Vesuvius magma (Scaillet et al. 2008). In case of a maximum possible *VND* between 0.1 and 0.3 mm^{-3} of pre-existing µm-sized vesicles at the onset of decompression (corresponding to the crystal number density in natural Vesuvius melt (Iacono-Marziano et al. 2007) acting as sites for heterogeneous vesicle nucleation), rates ≥ 0.06 $MPa \cdot s^{-1}$ are required to preserve initial H_2O concentration of interstitial melt. The decrease of inter-vesicle wall distance due to the growth of pre-existing vesicles can in first approximation be neglected for this example.

In magmas ascending with the rates at which homogeneous phase separation is possible, the independency of *VND* from decompression rate defines a phase separation horizon. The depth of the horizon corresponds to the largest possible supersaturation during decompression, leading within a very short time span to a high *VND*. Consequently, H_2O supersaturation is rapidly removed by the uptake of H_2O into growing vesicles due to short

diffusion distances. Further vesicle growth is caused by ongoing diffusion of H_2O into vesicles driven by decrease of H_2O solubility in the silicate melt and by the expansion of the fluid phase during further decompression. This results in a significant density decrease of magma that initiates a significant acceleration of magma ascent, which may end up in explosive volcanic eruptions. However, vesicle textures related to spinodal decomposition at the initial stage of phase separation might be significantly obscured and a direct comparison of our experimental textures and *VND*s with natural samples is difficult, if not impossible.

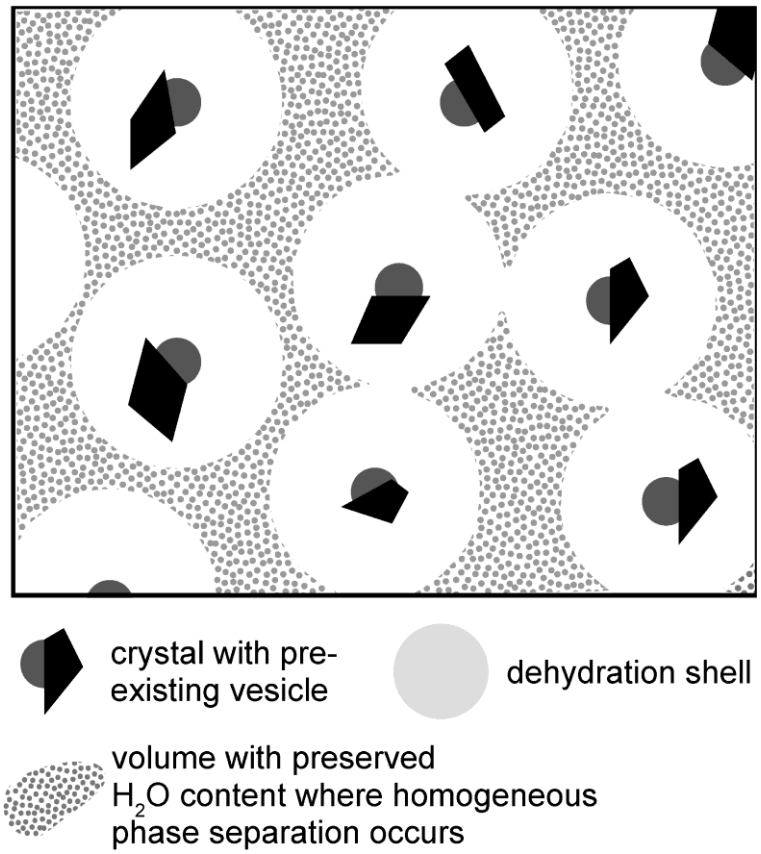

Fig. I.9 Schematic illustration of pre-existing vesicles on each crystal in a fluid saturated ascending subliquidus magma. During decompression, supersaturation is reduced by H_2O diffusion towards pre-existing vesicles, creating dehydration shells. Depending on decompression rate and the number of pre-existing vesicles, volumes can remain in which initial H_2O content is preserved and supersaturation increases until homogeneous phase separation occurs.

5. Conclusion

The observation of a decompression rate independent *VND* contrasts with previous experimental studies on other melt compositions (e.g., Hamada et al. 2010, Mourtada-Bonnefoi and Laporte 2004; Gardner et al. 1999) and up to now it remains unclear, whether

this independency is only valid for phonolitic melt. Therefore, there is a need to investigate a possible independency of *VND* from decompression rate for a broader range of melt compositions applying the strict experimental protocol of Preuss et al. (2016). Furthermore, not only decompression but also heating and changes in bulk chemistry during magma mingling and mixing can drive the hydrous silicate melt system into the metastable state towards instability and are possible triggers for phase separation. However, our experimental results are an indication but not a proof for spontaneous diffusion controlled spinodal decom-position at the limit of thermodynamic stability, where maximum supersaturation is reached and the second derivative of free energy of mixing to the H_2O content is ≤ 0. Quench effects may erase H_2O rich and H_2O poor domains in the early stage of decomposition due to an increase in H_2O solubility with decreasing temperature. In order to have a chance to distinguish between the different phase separation mechanisms, nucleation and spinodal decomposition, phase separation of hydrous silicate melt needs to be examined in-situ at high *P* and *T* by e.g., with laser or neutron scattering. Scattered light intensities reveal a distinct scattering maximum that grows with time in the case of spinodal decomposition and during nucleation and growth a scattering intensity that increases with time but shows a continuous decrease with increasing scattering angle (e.g., Xiong and Kiran 1998; Pan et al. 2006).

Assuming homogeneous nucleation and curvature reduced surface tension (Shea 2017), extremely high magma decompression rates of 18 $MPa \cdot s^{-1}$ are necessary to model the observed log*VND*s in our experiments and that of natural Vesuvius pumice in the range of 5–6 (Gurioli et al. 2005) with the DRM. In the case of heterogeneous nucleation at e.g., magnetite crystals where surface tension is significantly reduced (Shea 2017), still decompression rates of 6.7 $MPa \cdot s^{-1}$ are required to explain such high *VND*s. In contrast, our new finding is that such high *VND*s can be generated by homogeneous phase separation within melt regions between preexisting vesicles down to extremely low decompression rates of 0.06 $MPa \cdot s^{-1}$. This agrees with *VND* independent estimations of magma decompression rate for VAD79 of 0.25 $MPa \cdot s^{-1}$, derived by Shea et al. (2010a) from a conduit model of Papale and Dobran (1993). Our modeling, exemplarily for Vesuvius magma, suggests that for volcanic ejecta the mismatch between observed *VND* and ascent rate determined by DRM and independent methods de-pends on the number density of oxides (*OND*) that are effective heterogeneous vesicle nucleation sites. This number is controlled by c_{H2O}, *T*, *P* and oxygen fugacity of magma between liquidus and solidus. A change of these parameters may increase

or decrease *OND* and thus the number of heterogeneously formed vesicles. An increase of *OND* should match the proposed *VND* model of Shea (2017) when heterogeneously formed vesicles prevent the hydrous melt from supersaturation driven homogeneous phase separation, thus controlling the magma ascent rate. In contrast, a decrease of *OND* facilitates homogeneous phase separation of supersaturated melt with a d*P*/d*t* independent *VND* resulting in an increasing mismatch between observed *VND* and DRM. Our experimental findings represent a new challenge for the interpretation of volcanic dynamics and ejecta, further developments of computational modeling of explosive volcanic processes and improvement of risk assessment.

6. Supplement

Supplementary MS Excel file with detailed conditions and results of the isothermal decompression experiments is available online (open access):
https://ars.els-cdn.com/content/image/1-s2.0-S0012821X18305132-mmc1.xlsx

II. The effect of initial H_2O concentration on decompression-induced phase separation and degassing of hydrous phonolitic melt

A. Allabar, E. Salis Gross, M. Nowak

Abstract

Supersaturation of H_2O during magma ascent leads to degassing of melt by formation and growth of vesicles that may power explosive volcanic eruptions. Here we present experiments to study the effect of initially dissolved H_2O concentration (c_{H2Oini}) on vesicle formation, growth and coalescence in phonolitic melt. Vesuvius phonolitic melts with c_{H2Oini} ranging between 3.3 and 6.3 wt% were decompressed at rates of 1.7 and 0.17 MPa·s^{-1} and at temperatures ≥ 1323 K. Decompression started from 270 and 200 MPa to final pressures of 150–20 MPa, where samples were quenched isobarically. Optical microscopy and Raman spectroscopic measurements confirm that the glasses obtained were free of microcrystal and Fe-oxide nanolites, implying that the experiments were superliquidus and phase separation of the hydrous melt was homogeneous. A minimum number of the initially formed vesicles, defined by the number density normalized to vesicle free glass volume (*VND*), is observed at ~5 wt% c_{H2Oini} with a log*VND* of ~5 (in mm^{-3}). The log*VND* increases strongly towards lower and higher c_{H2Oini} by one order of magnitude. Furthermore, an important transition in evolution of vesiculation occurs at ~5.6 wt% c_{H2Oini} . At lower c_{H2Oini}, the initial *VND* is preserved during further decompression up to melt porosities of 30–50%. At higher c_{H2Oini}, the initial vesicle population is erased at low melt porosities of 15–21% during further decompression. This observation is attributed to vesicle coalescence favored by low melt viscosity. In conclusion, c_{H2Oini} determines the *VND* of initial phase separation and the evolution of vesiculation during decompression that controls the style of volcanic eruptions.

1. Introduction

Explosive volcanic activity is powered by rapid melt degassing of mainly H_2O, prior to and during fragmentation (e.g., Alidibirov and Dingwell 1996; Gonnermann and Manga 2007). Supersaturation of hydrous silicate melt induced e.g., by decompression drives vesicle formation and growth (e.g., Sparks 1978; Hurwitz and Navon 1994; Mourtada-Bonnefoi and Laporte 2004; Iacono-Marziano et al. 2007; Hamada et al. 2010; Gardner and Ketcham 2011; Preuss et al. 2016; Shea 2017; Hajimirza et al. 2019). The number of vesicles per unit volume of melt (*VND*), and thus the inter-vesicle distance, defines the degassing efficiency (e.g., Toramaru 2006; Allabar and Nowak 2018). The coupled magma density decrease amplifies ascent, volatile expansion, and fragmentation, and powers explosive volcanic eruptions (e.g., Kueppers et al. 2006; Genareau et al. 2012).

According to nucleation theory, which describes phase separation in the thermodynamically metastable state, the *VND* increases strongly with the decompression rate d*P*/d*t* (e.g., Hurwitz and Navon 1994; Toramaru 2006). In contrast to this dependence, a decompression rate independent *VND* was reported by Allabar and Nowak (2018) for hydrous phonolitic melt with white pumice composition of the Vesuvius 79AD eruption (VAD79). This composition is representative for other natural phonolitic and trachytic volcanic systems like the Campi Flegrei or Tambora that are known for violent explosive eruptions (e.g., Mastrolorenzo et al. 2001; Foden1986). The observed independence of *VND* on decompression rate in the investigated range of 0.024–10 MPa·s^{-1} is inconsistent with the theory of vesicle nucleation as phase separation mechanism. Alternatively, phase separation may be described by the theory of spinodal decomposition in the thermodynamically unstable state, for which the *VND* is expected to be independent from decompression rate (Allabar and Nowak 2018). Their experimentally observed log*VND*s (in mm^{-3}) of ~5.2 at initial H_2O concentration (c_{H2Oini}) of ~5.3 wt% match the lower end of the range of log*VND* of 5.15–7.08 recorded in natural VAD79 pumice (Gurioli et al. 2005; Shea et al. 2010a). However, natural eruptive products of the different stages of the AD79 Vesuvius eruption have been reported to originate from melts with c_{H2Oini} ranging between 3.0 and 6.4 wt% (Cioni 2000). So far, degassing of superliquidus phonolitic melt by homogeneous phase separation has been investigated as a function of decompression rate (Iacono-Marziano et al. 2007; Marxer et al. 2015; Preuss et al. 2016; Allabar and Nowak 2018) and slight variations in decompression temperature (1323–1373 K; Allabar and Nowak 2018). A systematic investigation of the effect of c_{H2Oini} on homogeneous phase separation of phonolitic melt during decompression is lacking. Dissolved H_2O significantly influences physicochemical parameters of silicate melt such as viscosity (e.g., Giordano et al. 2008), H_2O diffusivity (e.g., Nowak and Behrens 1997; Fanara et al. 2013), and surface tension (e.g., Bagdassarov et al. 2000). It is thus expected that c_{H2Oini} of silicate melt controls homogeneous phase separation by vesicle formation and the evolution of vesiculation during decompression. Therefore, experimental data of decompressed hydrous phonolitic VAD79 melt are compiled that fulfill the experimental protocol of Preuss et al. (2016) ensuring homogeneous phase separation (Iacono-Marziano 2007; Marxer et al. 2015; Preuss et al. 2016; Allabar and Nowak 2018). These data are extended by additional decompression experiments at temperatures (*T*)

between 1323 and 1523 K using VAD79 melt with varying c_{H2Oini} ranging between 3.3 and 6.3 wt% and a dP/dt of 0.17 MPa·s^{-1}.

2. Experimental methods

2.1 Starting material

Crystal-free homogeneous starting glasses of the VAD79 white pumice composition (Iacono-Marziano et al. 2007) were synthesized following the procedure of Marxer et al. (2015) in combination with the cooling optimization described by Allabar and Nowak (2018). Analyticalgrade oxide (SiO_2-glass, TiO_2, Al_2O_3, FeO, MgO, MnO) and carbonate ($CaCO_3$, Na_2CO_3, K_2CO_3) powders as well as $(NH_4)_2HPO_4$ as phosphorous source were used as raw materials for glass synthesis. To obtain accurate weight portions, the strongly hygroscopic SiO_2, Al_2O_3, and MgO powders were dried at 1073 K for 18 h, and the carbonate powders were dried at 383 K for 24 h and, subsequently, cooled and stored in a desiccator. The dried powders were weighed to obtain 50 g of glass for each batch. The powders were ground and mixed in a ZrO_2 ball mill for homogenization. One powder mixture used for the glass batch (VAD79_12) was ground in a corundum ball mill to minimize possible ZrO_2 contamination. Enrichment of ZrO_2 may lead to nanometer-sized Zr phases (Cormier et al. 2015; Dargaud et al. 2011) prior or during decompression of hydrous melt. Crystalline phases even at a nanometer scale may initiate heterogeneous H_2O vesicle nucleation (e.g., Shea 2017) that has to be avoided to study homogeneous phase separation.

The powder mixtures were decarbonated and fused in a Pt90Rh10 crucible by heating to 1873 K. After 6 h heating, the melts were rapidly quenched in deionized water. The cracked glasses were crushed and ground in the respective ball mills and melted again for 1 h at 1873 K. To inhibit crystallization, the melts were then air-cooled within 1–2 min close to the glass transition temperature (T_g) of 937 K, calculated after Giordano et al. (2008) assuming an H_2O content of 1000 ppm. Subsequently, the supercooled melts were transferred into a furnace preheated to 833 K. The furnace was then switched off to maintain a cooling rate of ~5 K·min^{-1}. This cooling procedure was fast enough to inhibit partial crystallization, and stress-induced cracking within the glass batches was minimized when cooling to room temperature. The compositions of the VAD79 glasses measured prior to the decompression experiments are given in Table II.1.

Cylinders with a diameter of 5 mm were drilled from the glass batches and cut to lengths of 5.3–6.7 mm. The sharp cylinder edges were rounded with abrasive paper to prevent capsule damage during pressurization. The porosity of the glass cylinders, caused by some air vesicles trapped during melt synthesis, was determined by pycnometry to confirm porosities < 6% prior to the combined hydration and decompression experiments (Preuss et al. 2016).

Table II.1 Bulk glass compositions (in wt%) of synthesized VAD79 glasses, used for decompression experiments based on white pumice composition given in Iacono-Marziano (2007) ($VAD79^{IM07}$) and measured by electron microprobe analysis after glass synthesis and normalized to 100%.

	$VAD79^{IM07}$	VAD79_03	VAD79_06	VAD79_07	VAD79_08	VAD79_10	$VAD79\_12^{\#}$
SiO_2	57.15 (39)	57.66 (43)	56.97 (44)	57.19 (56)	57.82 (27)	57.4 (39)	57.73 (34)
TiO_2	0.30 (05)	0.29 (03)	0.30 (02)	0.29 (02)	0.28 (02)	0.29 (02)	0.28 (03)
Al_2O_3	21.34 (25)	20.96 (31)	21.27 (19)	21.15 (19)	20.69 (23)	20.77 (24)	20.77 (34)
FeO	2.70 (17)	2.70 (18)	2.74 (17)	2.72 (21)	2.69 (11)	2.72 (05)	2.62 (11)
MnO	0.14 (06)	0.14 (03)	0.16 (03)	0.15 (04)	0.14 (04)	0.14 (02)	0.14 (03)
MgO	0.39 (05)	0.39 (03)	0.39 (03)	0.36 (04)	0.38 (04)	0.37 (04)	0.3 (02)
CaO	3.26 (12)	3.2 (18)	3.27 (10)	3.15 (10)	3.10 (09)	3.19 (08)	3.17 (10)
Na_2O	5.16 (15)	5.38 (18)	5.31 (20)	5.37 (18)	5.37 (19)	5.40 (20)	5.32 (17)
K_2O	9.46 (15)	9.17 (57)	9.52 (16)	9.41 (12)	9.39 (14)	9.62 (16)	9.49 (23)
P_2O_5	0.09 (04)	0.10 (03)	0.08 (03)	0.09 (03)	0.09 (03)	0.10 (07)	0.08 (03)
ZrO_2	n.d.	n.d.	n.d.	0.12 (05)	0.10 (05)	n.d.	0.06 (02)

ZrO_2 concentrations are mean of measured concentrations above detection limit of ~350 ppm.
n.d.: ZrO_2 was not analyzed in these glasses
numbers in brackets are 1σ standard deviations
#: synthesized using a corundum ball mill; all other batched were synthesized using a ZrO_2 ball mill

2.2 Capsule preparation

A sufficiently large capsule volume has to be ensured, which is capable of containing the melt with equilibrium porosity (Φ_{equ}) without bursting during decompression to the relevant final pressure (P_{final}). Therefore, the Φ_{equ} at each P_{final} was calculated using the expected porosity Equation of Gardner (1999) (Equation 5 therein). The H_2O solubility dependence from solubility experiments of Iacono-Marziano et al. (2007) and Marxer et al. (2015), the equation of state (EOS) for H_2O of Duan and Zhang (2006), and the melt density calculation of Ochs and Lange (1999) were used for calculation. The resulting sample volumes were considered for the relationship of capsule to glass cylinder length. Cleaned and annealed Au80Pd20 tubes (13 mm length, 5 mm inner diameter) were closed with an electric arc-welded lid at the bottom. Glass cylinders were inserted into the capsules together with

the desired amount of water. The top of each capsule was crimped to a three-sided star and welded shut while cooling with liquid nitrogen to prevent H_2O loss by vaporization. A typical weight loss by welding-induced capsule metal loss is ~0.3 mg for the used design. If the weight loss of glass and water filled capsules m_{wl} was determined to be > 0.3 mg after welding, m_{wl}-0.3 mg was attributed to H_2O loss as expressed in the negative errors given in Table II.2 for the gravimetrically determined initial H_2O concentration ($c_{H2Ograv}$). However, it may be possible that more than 0.3 mg Au80Pd20 is lost instead of H_2O during welding. This would result in an overestimation of the negative error of $c_{H2Ograv}$. To check for possible leakage, the capsules were stored in a compartment dryer at 383 K, pressurized to 100 MPa at ambient T in a cold seal pressure vessel and again stored in a compartment dryer. After each step, the weight of the capsule was checked to exclude leakage prior to the decompression experiments.

3. Decompression experiments

3.1 Experimental technique

The combined hydration and decompression experiments were performed in an internally heated argon pressure vessel (IHPV) equipped with a rapid quench setup and a piezoactuator driven high-pressure valve for continuous decompression (Berndt et al. 2002; Nowak et al. 2011). The intrinsic redox condition of the IHPV is 3.5 log units above the quartz fayalite magnetite (QFM) buffer at H_2O saturated run conditions (Berndt et al. 2002). All samples were hydrated for at least 94 h at T ranging between 1500 and 1550 K at a starting pressure (P_{start}) of 200 MPa, except of CD83 and the samples with c_{H2Oini} > 5.6 wt%, which were hydrated at 198 and 270 MPa, respectively. After hydration, T was decreased to superliquidus decompression temperatures (T_d) ranging between 1323 and 1523 K (Table II.2) and thermally equilibrated for at least 0.5 h before isothermal decompression was initiated. Two control thermocouples recorded sample temperature gradients of < 20 K over a distance of ~12 mm. Because the sample length is lower (< 6.7 mm) than the distance of the two thermocouples, the T gradient within the samples is < 10 K.

For the decompression rates ≥ 0.17 MPa·s^{-1}, the micrometer screw of the decompression valve was used to release pressure manually. During decompression, T decreased by ~5–10 K due to adiabatic cooling that could not fully be compensated by the digitally controlled furnace power. Only during decompression of sample CD95, which was

decompressed to the lowest P_{final} of 20 MPa, the maximum T drop was ~50 K at P_{final}. At P_{final}, the decompression valve was closed and the capsules were isobarically quenched using an electrical power supply to melt the quench platinum wire, at which the capsules were suspended in the sample holder. Successful capsule drop was confirmed by a monitored T decrease ranging between 2 and 10 K in the hot zone of the furnace. The maximum achievable cooling rate of the IHPV is about 150 $K \cdot s^{-1}$ (Berndt et al. 2002). However, this cooling rate induces stress-induced cracks within the quenched glass samples. This leads to disintegration of the samples during further preparation. Therefore, a 35 mm brass cylinder was mounted at the bottom of the sample holder to reduce the cooling rate and thus crack formation during quench. The medium quench rate (MQ) of 44 ± 11 $K \cdot s^{-1}$ (Allabar et al. 2020b) inhibited disintegration of the samples during preparation.

3.2 Experimental decompression condition

The data for published decompression experiments using VAD79 white pumice composition (Iacono-Marziano et al. 2007; Marxer et al. 2015; Preuss et al. 2016; Allabar and Nowak 2018) that fulfill the experimental protocol given in Preuss et al. (2016) are compiled in Table II.2. The experimental protocol ensures homogeneous phase separation by vesicle formation in the central part of the sample without effects of the experimental design or capsule size. Therefore, only data of experiments using glass cylinders were considered to exclude *VND* data influenced by pre-existing vesicles induced by the use of glass powder as starting material (Preuss et al. 2016). Additionally, the limitation of decompression rate defined by the sample diameter is considered, ensuring a central sample volume that is unaffected by diffusional H_2O loss into early-formed fringe vesicles at the capsule wall and by vesicles ascending from the capsule bottom into the central melt volume (Iacono-Marziano et al. 2007; Marxer et al. 2015; Preuss et al. 2016; Allabar and Nowak 2018). At a decompression rate of 0.024 $MPa \cdot s^{-1}$, homogeneous phase separation is facilitated only in a small central melt volume that is already affected by diffusional H_2O loss into fringe vesicles using 5 mm diameter samples with 5.3 wt% c_{H2Oini} (Allabar and Nowak 2018). This defines the decompression rate limit for capsules with 5 mm diameter at the given H_2O concentration. With decreasing c_{H2Oini}, the H_2O diffusivity and, consequently, the H_2O-depleted drainage zone width decrease. This expands the feasible decompression rate towards

lower values, at which homogeneous phase separation can still be observed in the central sample volume.

The compiled published VAD79 superliquidus decompression experiments were extended during this study by additional experiments to obtain four experimental series and an undecompressed reference sample (Table II.2): (1) To investigate the influence of c_{H2Oini} on the degassing behavior of phonolitic melt, the C-series was performed with fixed T of 1323 K and a dP/dt of 0.17 MPa·s^{-1}, while the c_{H2Oini} was changed. Therefore, the experimental set given in Allabar and Nowak (2018) with a c_{H2Oini} of 5.3 wt% H_2O was extended by experiments with higher (~6.3 wt%) and lower c_{H2Oini} (~3.3 and ~4.3 wt%; Table II.2; Fig. II.1). These samples were decompressed to P_{final} ranging between 20 and 150 MPa. The 5.3 wt% c_{H2Oini} data set of Allabar and Nowak (2018) at a dP/dt of 0.17 MPa·s^{-1} was extended by an experiment with a P_{final} of 60 MPa (CD73). The sample CD83 was hydrated with excess H_2O to prove that there is no difference in *VND* after decompression from H_2O supersaturated (CD73 of this study and experiments by Iacono-Marziano et al. 2007 and Marxer et al. 2015) and H_2O undersaturated conditions (Preuss et al. 2016, Allabar and Nowak 2018, this study). To obtain a similar c_{H2Oini}, CD83 was hydrated at 198 MPa, where H_2O solubility is 5.34 wt% (Iacono-Marziano et al. 2007; Marxer et al. 2015). In this case, the homogenization time after T decrease from hydration T to T_d was 1.5 h to ensure re-equilibration and homogenization of H_2O concentration due to increasing solubility with decreasing T (Schmidt and Behrens 2008). The experiment CD-C-23 of Preuss et al. (2016) also fulfills the experimental parameters of the C-series. (2) Experiments of the D-series were performed with a c_{H2Oini} of ~5.3 wt%. This series is a compilation of experiments performed at 1323 K with variable decompression rates. The experiments from Allabar and Nowak (2018), and experiments listed therein, were extended by the experiment CD28 decompressed with 1.7 MPa·s^{-1}. (3) To ensure T_d being well above the liquidus, experiments at 1373 K were performed (Allabar and Nowak 2018) at decompression rates of 1.7 MPa·s^{-1} (TD-series) and (4) 0.17 MPa·s^{-1} (T-series). The experiment CD44 was decompressed at 1523 K with the latter rate.

The sample Ref_A2 was hydrated with 5.3 wt% H_2O at 1523 K and 200 MPa. The sample was quenched with MQ without decompression after the T decrease to 1323 K and a homogenization time of 0.5 h. Therefore, this sample represents the initial state of the samples with c_{H2Oini} of 5.3 wt% prior to decompression.

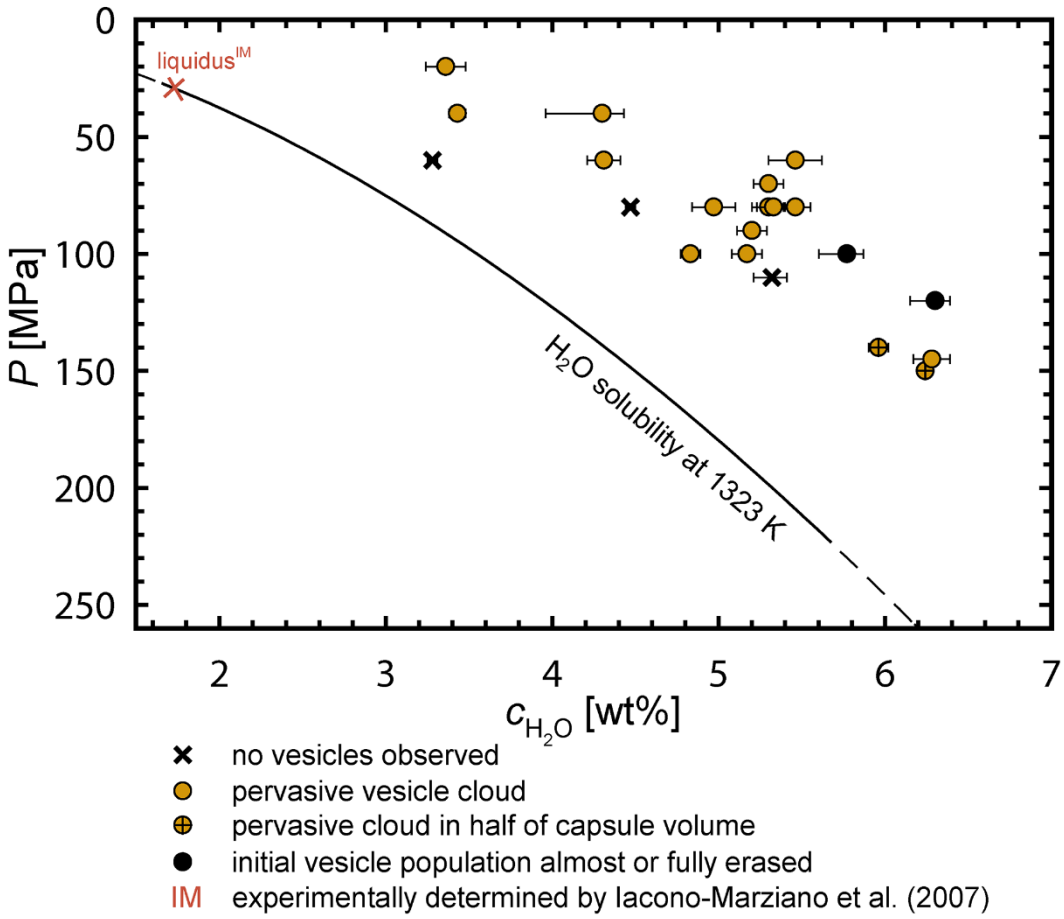

Fig. II.1 Experiments of the C-series plotted at final pressure (P_{final}) and initial H_2O concentration (c_{H2Oini}) (Table II.2). Symbol fillings indicate textural features of the samples. The samples were decompressed with 0.17 MPa·s^{-1} at 1323 K and quenched with 44 K·s^{-1} (MQ). The H_2O solubility curve (solid line) is derived from solubility experiments of Iacono-Marziano et al. (2007) and Marxer et al. (2015) (c_{H2O}[wt%] = 0.2321·P[MPa]$^{0.5928}$) and extrapolated towards high c_{H2O} (dashed end of line). The cross with the index "liquidus^{IM}" marks the P with corresponding equilibrium c_{H2O} at which the liquidus was experimentally determined (Iacono-Marziano et al. 2007; Marxer et al. 2015). Pervasive vesicle clouds within the central sample volumes are observed in all vesiculated samples with c_{H2Oini} < 5.6 wt%. These clouds are stable down to low P_{final}. At higher c_{H2Oini}, the initially formed main vesicle population is erased at relatively high P_{final} of ≥ 100 MPa.

Table II.2 Experimental conditions and results. All samples were hydrated prior to decompression for at least 94 h at 1500–1550 K at P_{start}.

series	sample	glass batch VAD79_	vesicle population	P_{start} [MPa]	P_{sat} [MPa]	T_d [K]	P_{final} [MPa]	dP/dt [MPa·s^{-1}]	t_d [min]
no vesicles observed									
	RefA_2	10	-	200	192	1323	-	-	
C	CD93	12	-	200	88	1323	60	0.17	2.7
C	CD86	10	-	200	147	1323	80	0.17	6.5
C	CD48	7	-	200	199	1323	110	0.17	8.7
vesiculated samples									
C	CD94	12	main	200	94	1323	40	0.17	5.3
C	CD95	12	main	200	91	1323	20	0.17	7.0
C	CD87	10	main 2nd(cap)	200	138	1323	60	0.17	7.7
C	CD85	10	main 2nd(cap) 2nd(ves)	200	138	1323	40	0.17	9.6
C	CD-C-23	3	main	200	167	1323	100	0.17	6.6
C	CD40	8	main	200	187	1323	100	0.17	8.5
C	CD42	8	main	200	189	1323	90	0.17	9.7
C	CD63	7	main	200	195	1323	80	0.17	11.2
C	CD39	8	main	200	175	1323	80	0.17	9.3
C	CD91	12	main 2nd(cap)	200	197	1323	80	0.17	11.4
C	CD83	12	main	198	198	1323	80	0.17	11.6
C	CD50	7	main	200	195	1323	70	0.17	12.2
C	CD73	10	main 2nd (cap) 2nd (ves)	200	200	1323	60	0.17	13.7
C	CD102	12	main	270	255	1323	150	0.17	10.3
C	CD101	12	main	270	258	1323	145	0.17	11.1
C	CD97	12	coalesced	270	260	1323	120	0.17	13.7
C	CD98	12	main	270	237	1323	140	0.17	9.5
C	CD100	12	main(clouds) coalesced	270	224	1323	100	0.17	12.2
D	CD92	10	main	200	183	1323	80	0.064	26.7
D	CD78	10	main	200	184	1323	82	1.7	1.0
D	B74	-	main	200	200	1323	70	1.69	1.3
D	B72	-	main	200	200	1323	75	4.63	0.4
D	SSD06	2	main	200	200	1323	75	10	0.2
D	CD28	3	main	200	194	1323	95	1.7	1.0
D	CD-C-25	3	main	200	158	1323	100	0.024	40.5
D	CD77	10	main	200	160	1323	80	0.024	55.6
TD	CD59	6	main	200	189	1373	110	1.7	0.8
TD	CD55	6	main	200	190	1373	100	1.7	0.9
TD	CD57	6	main	200	196	1373	100	1.7	0.9
TD	CD51	7	main	200	193	1373	75	1.7	1.2
T	CD52	7	main	200	189	1373	90	0.17	9.7
T	CD53	7	main	200	187	1373	80	0.17	10.5
T	CD44	8	half capsule	200	174	1523	80	0.17	9.3

P_{start}: hydration pressure and starting pressure of decompression; P_{sat}: saturation P calculated from dependency of H_2O solubility experiments by Iacono-Marziano et al. (2007) and Marxer et al. (2015), for supersaturated experiments $P_{start} = P_{sat}$; T_d: decompression temperature; P_{final}: final pressure, at which samples were isobarically quenched; dP/dt: decompression rate; t_d: decompression time = (P_{sat}-P_{final})/(dP/dt); $c_{H2Ograv}$: gravimetrically determined H_2O concentration in the capsule; c_{H2OIR}: total H_2O concentration measured by FTIR with vesicles in beam; (ves) in the drainage zone of a large vesicle; (cap) in drainage zone towards the capsule wall;

(Table II.2 continued) The c_{H2O} printed in bold numbers are the c_{H2Oini} of the experiments.

$c_{H2Ograv}$ [wt%]	+	-	c_{H2OIR} [wt%]	Φ_{glass} [vol%]	*VND* [mm^{-3}]	log*VND* [mm^{-3}]	references
5.27	0.10	0.10	5.26± 0.05	-	-	-	
3.34	0.10	0.10	3.28 ± 0.03	-	-	-	
4.35	0.11	0.23	4.47 ± 0.03	-	-	-	
5.32	0.09	0.09	5.37 ± 0.06	-	-	-	AN18
3.40	0.10	0.10	**3.43 ± 0.05**	0.3 ± 0.1	9.11E+05[a]	5.96	
3.36	**0.12**	**0.12**	-	15.4 ± 2.1	2.35E+06[b]	6.37	
4.31	**0.10**	**0.10**	-	5.4 ± 1.3	3.26E+05[ab]	5.51	
			-	0.3 ± 0.1	5.23E+05[a]	5.72	
4.30	**0.13**	**0.34**	-	24.4 ± 2.2	2.83E+05[b]	5.45	
			4.27 ± 0.07	3.2 ± 0.5	1.38E+06[c]	6.14	
			4.27 ± 0.07	0.2 ± 0.1	4.61E+05[a]	5.66	
4.76	0.10	0.10	**4.83 ± 0.06**	< 0.1	1.01E+05[a]	5.00	PR16
5.27	0.09	0.09	**5.17 ± 0.09**	< 0.1	1.40E+05[a]	5.15	AN18
5.31	0.09	0.09	**5.20 ± 0.09**	1.1 ± 0.1	9.59E+04[b]	4.98	
5.30	**0.10**	**0.10**	-	7.0 ± 0.7	1.74E+05[b]	5.24	AN18
5.34	0.09	0.09	**4.97 ± 0.13**	4.5 ± 0.5	1.49E+05[b]	5.17	AN18
5.33	**0.10**	**0.10**	-	9.0 ± 1.1	2.56E+05[bc]	5.41	
			5.20 ± 0.13	1.3 ± 0.4	9.26E+05[a]	5.97	
5.34*	0.17	0.17	**5.46 ± 0.07**	3.2 ± 1.0	6.08E+05[a]	5.78	
5.30	**0.09**	**0.09**	-	13.1 ± 1.4	6.70E+04[ab]	4.83	AN18
5.46*	**0.17**	**0.17**	-	18.5 ± 2.2	3.03E+05[bc]	5.41	
			4.99 ± 0.18	1.0 ± 0.3	8.14E+05[a]	5.91	
			-	9.0 ± 1.0	1.16E+06[c]	6.07	
6.30	0.10	0.41	**6.24 ± 0.03**	0.2 ± 0.1	4.99E+05[a]	5.70	
6.30	0.11	0.29	**6.28 ± 0.11**	2.3 ± 0.7	6.08E+05[ac]	5.78	
6.30	**0.09**	**0.15**	-	8.9 ± 1.4	8.27E+01[b]	1.92	
6.27	0.10	0.47	**5.96 ± 0.06**	0.3 ± 0.1	6.85E+05[a]	5.84	
5.77	**0.10**	**0.17**	5.43 ± 0.07	0.2 ± 0.1	8.08E+05[a]	5.91	
			-	9.3 ± 2.3	5.54E+01[b]	1.74	
5.27	0.10	0.10	**5.10 ± 0.09**	4.6 ± 0.6	2.25E+05[b]	5.35	AN18
5.30	0.11	0.11	**5.12 ± 0.05**	3.3 ± 0.6	2.11E+05[ab]	5.32	AN18
5.46*	**0.16**	**0.16**	5.09[#] ± 0.5	5.0 ± 1.0	5.65E+05	5.75	IM07
5.46*	**0.16**	**0.16**	5.22[#] ± 0.35	6.0 ± 1.0	7.71E+05	5.89	IM07
5.46*	**0.16**	**0.16**	-	15.0 ± 1.5	2.57E+05[b]	5.41	MA15
5.34	0.10	0.10	**5.29 ± 0.06**	0.5 ± 0.1	1.12E+05[ab]	5.05	
4.66	0.10	0.10	**4.68 ± 0.05**	< 0.1	1.30E+05[a]	5.11	PR16
5.29	0.11	0.17	**4.71[$] ± 0.03**	< 0.1	2.45E+05[a]	5.39	AN18
5.44	0.10	0.10	**5.21 ± 0.05**	< 0.1	3.02E+05[a]	5.48	
5.29	0.10	0.10	**5.22 ± 0.05**	0.5 ± 0.1	3.96E+04[ab]	4.60	
5.32	0.10	0.10	**5.32 ± 0.07**	< 0.1	6.02E+04[a]	4.78	
5.33	0.09	0.17	**5.27 ± 0.11**	4.2 ± 0.9	9.58E+04[ab]	4.98	AN18
5.33	0.10	0.10	**5.21 ± 0.07**	1.6 ± 0.4	9.18E+04[ab]	4.96	
5.28	0.10	0.10	**5.17 ± 0.06**	1.5 ± 0.2	9.00E+04[b]	4.95	AN18
5.28	0.10	0.10	**4.96[$] ± 0.18**	< 0.1	7.37E+05[a]	5.87	

Φ_{glass}: glass porosity; *VND*: vesicle number density normalized to vesicle-free glass, analyzed with: transmitted light microscopy, b SEM-BSE-imaging, c laser scanning microscopy imaging; *supersaturated conditions, value corresponds to solubility at hydration P and T_d; [$] diffusional H_2O loss towards fringe vesicles prior to phase separation due to low decompression rate (Allabar and Nowak 2018); [$] diffusional H_2O loss prior to phase separation due to high diffusivity at high T_d; # EMPA by-difference method between vesicles (Devine et al. 1995); References PR16: Preuss et al. (2016); AN18: Allabar and Nowak (2018); IM07: Iacono-Marziano et al. (2007); MA15: Marxer et al. (2015).

3.3 Sample preparation

Pieces from the starting glass batches were embedded in epoxy resin and ground and polished for electron microprobe analysis (EMPA). The decompressed samples and the hydrated sample REF_A2 were cut along the cylinder axis. One half was embedded in epoxy resin and ground and polished for EMPA, scanning electron microscopy (SEM), laser scanning microscopy (LSM), and Raman micro-spectroscopy (RMS). The other halves were unwrapped from the capsule material, embedded with epoxy resin in glass-ceramic rings, and ground to a thickness of 100–320 μm. These samples were polished on both sides to obtain thin sections for Fourier transform infrared micro-spectroscopy (FTIR) and transmitted light microscopy analysis (TLM). Sample thickness was measured with a Mitutoyo digital micrometer (± 3 μm).

4. Analytical methods

4.1 Electron microprobe analysis

After glass synthesis, pieces of each glass batch were analyzed with a JEOL JXA 8900 R electron microprobe to confirm chemical composition and homogeneity (Table II.1). EMPA WDS measurements were conducted with an acceleration voltage of 15 kV, 3 nA beam current, and a defocused beam of 20 μm to optimize for Na analysis (Devine et al. 1995). Peak counting times were set to 10 s (Na), 16 s (Si, Al, Fe, Mg, Ca, K), and 30 s (Ti, Mn, P) according to Preuss et al. (2016). Zr was additionally analyzed in glasses VAD79_07, 08, and 12 with a peak counting time of 60 s. 15–20 randomly distributed points were measured for each glass. The results (Table II.1) agree within error with the VAD79 white pumice composition given in Iacono-Marziano et al. (2007).

4.2 Quantitative determination of *VND* and porosity

VND and glass porosity (Φ_{glass}) were determined in the central part of the samples where they are texturally homogeneous. Thus, convection-like patterns and effects of the capsule–melt contact, such as heterogeneously formed fringe vesicles and H_2O-depleted drainage zones, were excluded from quantitative analysis (see results for further textural features). Sample vesicle textures with average vesicle diameters of > 5 μm were analyzed with backscattered electron (BSE) or LSM images. *VND*s of samples containing smaller vesicles

were quantified in thin sections with transmitted light microscopy. In some samples, several areas (BSE) and volumes (TLM) were analyzed (Table II.2). Analysis of up to three areas within one sample resulted within error (± 0.13 log units, see description below) in similar *VND* and Φ_{glass}. Mean values are, therefore, given in Table II.2.

4.2.1 Quantitative SEM and LSM image analysis

BSE images of the intersected samples were recorded with a LEO 1450 VP SEM or a Hitachi TM2020plus tabletop SEM, using individual magnifications of 150–2000× to resolve the smallest detectable vesicle intersections on a µm scale. Several adjacent images were recorded and stitched for analysis. Surfaces of the intersected samples were imaged with a Keyence VK-X100 confocal laser scanning microscope. These images with contrast-rich surface information were treated similarly as the BSE images for quantitative image analysis. Both methods yielded similar *VND* within error, as tested with the sample CD73 for reference. BSE or LSM images were quantitatively analyzed with ImageJ combined with a stereological 2D to 3D transformation, using CSDCorrections (Higgins 2000) as described in detail by Marxer et al. (2015) and Preuss et al. (2016). An analytical error in *VND* determination of ± 0.13 log units was estimated considering all steps that are prone to errors, such as the choice of different analyzed areas within a sample, different operators for counting vesicles, or filling of vesicle intersections by blackening, to obtain sufficient contrast between glass and intersected vesicles for image analysis. Errors in porosity from image analysis were provided by CSDCorrections.

4.2.2 Transmitted light microscopy

Vesicles were quantified in the thin sections by marking the vesicles, while focusing through the samples with a Zeiss Axio Image M2M microscope, using the Fission Track Studio software "Trackworks". The sizes of the analyzed areas were chosen individually for each measurement ranging between $2.3 \cdot 10^{-2}$ and $8.5 \cdot 10^{-5}$ mm^2. Together with the sample thickness, this defines the size of the analyzed volume used to normalize the counted number of vesicles to the number of vesicles per mm^3. Mean vesicle diameters were determined with the software-provided measurement tool to calculate Φ_{glass} and *VND*. Furthermore, inspection with TLM ensured microlite-free experimental samples. Errors from TLM analysis were calculated with an error propagation calculation using the error in sample

thickness of ± 3 μm and assuming an error of 10% for vesicle size measurement, and 5% for the vesicle count.

4.3 Raman micro-spectroscopy

RMS was used to detect possible Fe-oxide nanolitization of the glasses, which is suggested to significantly affect the degassing behavior of supersaturated hydrous melt (Di Genova et al. 2017a, 2018; Shea 2017). The hydrated samples REF02 (Marxer et al. 2015), Ref_A2 (this study), and the partly degassed samples CD73 and CD95 with VAD79 composition were measured for this purpose. For comparison, hydrated glasses (IB_C_1a, IB_P2), a nominally dry glass (CI_glass), and a partly degassed sample (CD_C_5) from Preuss et al. (2016) with trachytic Campanian Ignimbrite (CI) composition, which shows similar degassing behavior to VAD79 melt (Preuss et al. 2016), were analyzed. Raman spectra were collected using a Renishaw InVia confocal Raman micro-spectrometer equipped with a 532 nm laser, a 1800 grooves·mm^{-1} grating and an Peltier-cooled CCD detector. Laser power was set to 10%, which corresponds to a laser power of ~2.5 mW on the sample. This energy is sufficiently low to avoid oxidation (Di Genova et al. 2017a) and dehydration of the samples. A 50× objective with a numerical aperture of 0.75 was used together with the standard confocality setting. Focus depth was adjusted 6 μm below the sample surface to optimize the signal intensity (Di Genova et al. 2017a). Spectra were collected ranging between 300 and 950 cm^{-1}, and acquisition times were 10 s for each of three accumulations.

4.4 FTIR micro-spectroscopy

Near-infrared (NIR) measurements were performed with a Hyperion 3000 IR microscope connected to a Bruker Vertex v80 FTIR spectrometer to determine total H_2O contents (c_{H2OIR}) of the decompressed samples. A tungsten light source, a CaF_2 beam splitter, and an InSb single-element detector were used together with a 15× Cassegrain objective. For each measurement, 50 scans in transmission mode were recorded with a spectral resolution of 4 cm^{-1} using air as reference. Following the method of Behrens et al. (1996), the total H_2O contents were determined from molecular H_2O (~5210 cm^{-1}) and hydroxyl absorbance (4470 cm^{-1}). To calculate total H_2O contents, peak heights after linear background correction were used together with the linear molar extinction coefficients $\varepsilon_{H2O} = 1.18$ and $\varepsilon_{OH} = 1.14$ l·mol^{-1}·cm^{-1} and the glass density dependence on H_2O concentration

ρ[g·cm^{-3}] = 2.47-0.013·c_{H2O} [wt%] (Iacono-Marziano et al. 2007). H_2O concentration profiles were measured perpendicular and parallel to the samples cylinder axis using a motorized XYZ microscope stage and a knife-edge aperture that was set to a measurement window of 50 × 50 µm. During profile measurements and due to small inter-vesicle distances on a 10 µm scale, the H_2O-filled vesicles in samples with low Φ_{glass} < 5% were measured together with H_2O dissolved in the glass in the probed sample volumes. At higher glass porosities, these measurements were not possible, because samples become increasingly opaque with respect to NIR light.

5. Results

5.1 ZrO_2 concentration of synthesized glasses

The two glasses VAD79_07 and 08 synthesized using a ZrO_2 ball mill reveal ZrO_2 concentrations of 1200 and 1000 ppm, respectively (Table I.1). These values are higher than for the glass that was synthesized using a corundum mill (VAD79_12) with a ZrO_2 concentration of 600 ppm. Note that the given concentrations are mean values of those measurements for which the ZrO_2 concentration was above the detection limit of 350 ppm. For VAD79_07, this was the case in 19 out of 20 measurements, for VAD79_08 in 13 out of 15 analyses, and only 9 out of 20 measurements for VAD79_12. The results indicate that a contamination by 400–600 ppm ZrO_2 by mechanical erosion during milling occurred in glass batches using a ZrO_2 ball mill as compared to the glass using a corundum ball mill for synthesis.

5.2 Fe-oxide nanolites

Following the method of Di Genova et al. (2017a, 2018), RMS measurements confirm the absence of a distinct Raman scattering band at 670–690 cm^{-1} (Fig. II.2a), indicative of Fe-oxide nanolites, for undecompressed and decompressed VAD79 samples (2.7 wt% FeO_{tot}, 1.37–5.26 wt% H_2O). In contrast, experimental undegassed and partially degassed hydrous CI samples (4.41 wt% FeO_{tot}, Preuss et al. 2016) with c_{H2O} > 3 wt% show a distinct Raman band at 680 cm^{-1}. This is consistent with the nanolite occurrence field of hydrous Fe-bearing silicate glasses (Fig. II.2b) defined by Di Genova et al. (2017a).

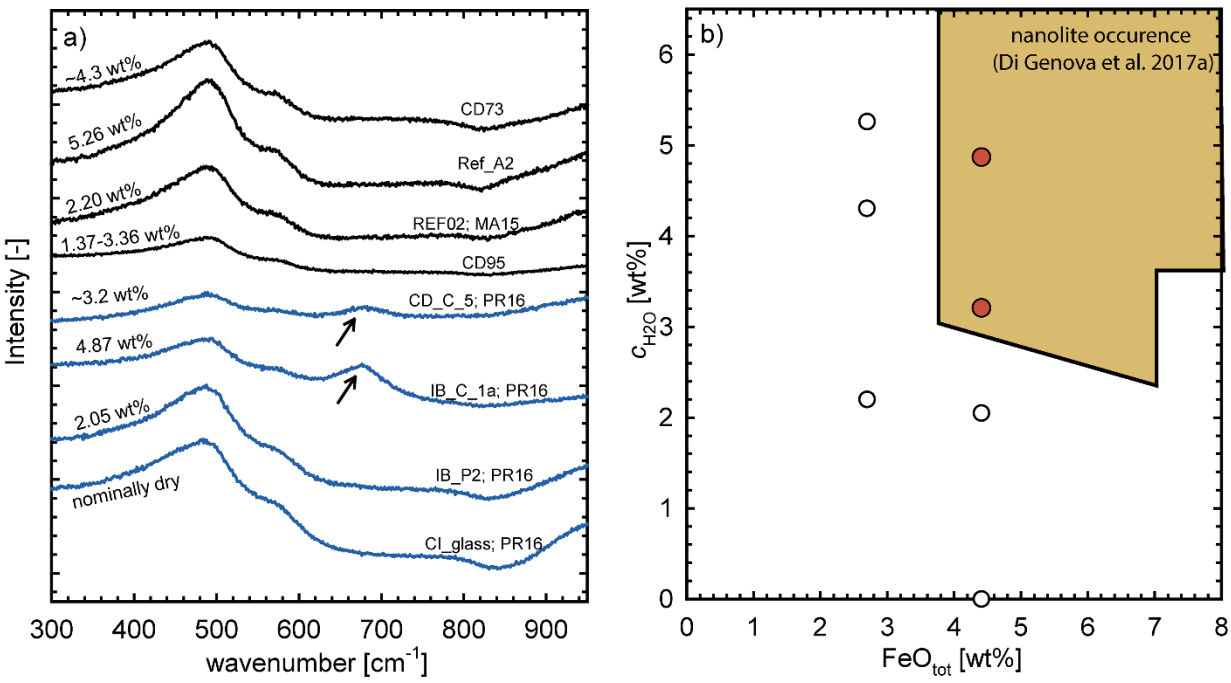

Fig. II.2 a) Raman spectra of phonolitic VAD79 and trachytic (Campania Ignimbrite (CI) composition) samples with 2.7 and 4.4 wt FeO_{tot} respectively. Numbers at each spectrum are H_2O concentrations (c_{H2O}) in the glasses. In undecompressed and vesicle-free samples (Ref_A2, REF02, IB_C_1a, IB_P2), c_{H2O} was measured with FTIR in transmission. Due to the high glass porosity in the decompressed samples, c_{H2O} of CD73 was determined with Raman micro-spectroscopy (Allabar et al. 2020b) and H_2O concentration given for CD-C-5 is the calculated residual c_{H2O} (Preuss et al. 2016). For CD95, the estimated possible range of c_{H2O} in the glass is given, which is between equilibrium c_{H2O} at P_{final} and T_d and the c_{H2Oini}. At c_{H2O} of 4.87 and ~3.2 wt%, a Raman signal indicative of Fe-oxide nanolites is detected at ~680 cm^{-1} (Di Genova et al. 2017a) in samples of CI composition. Fe-oxide nanolites were not detected in the VAD79 samples (black spectra) and the CI samples (blue spectra) with low H_2O contents. References: MA15: Marxer et al. 2015; PR16: Preuss et al. 2016. b) Fe-oxide nanolite occurrence field (yellow area) determined by Di Genova et al. (2017a). The samples of CI composition in which nanolites were detected (filled, red circles) fall into the area. All samples with c_{H2O} and FeO_{tot} concentrations outside this area do not show Raman bands indicative of Fe-oxide nanolites, consistent with the results of Di Genova et al. (2017a).

5.3 Vesicle textures

In all decompressed samples, at the capsule–glass interface, strongly deformed 50–350 µm sized fringe vesicles are present, which increase in size with decreasing P_{final} (Fig. II.3). In the central sample volume, vesicles are not observed at 60, 80, and 110 MPa in experiments with c_{H2Oini} of 3.28 (CD93), 4.47 (CD86), and 5.32 wt% (CD48), respectively. In all other samples, the central volume is vesiculated and surrounded by a vesicle-free zone (drainage zone) close to the capsule walls. In samples decompressed with 0.17 MPa·s^{-1}, the drainage zone width increases with c_{H2Oini} from ~250 µm at 3.3 wt% to ~500 µm at 4.3 and 5.3 wt% and ~650 µm at 6.5 wt% (Fig. II.3), due to increased H_2O diffusivity. These values were

determined for samples with low Φ_{glass}, because the drainage zone thins out, as the porosity in the vesiculated sample volume and the fringe vesicles increase the total sample volume. Furthermore, the drainage zone becomes thinner in case of a second phase separation event, located close to the main population (see description below). On the other hand, the drainage zone width increases with decreasing decompression rate due to increased time for H_2O diffusion as shown in Allabar and Nowak (2018).

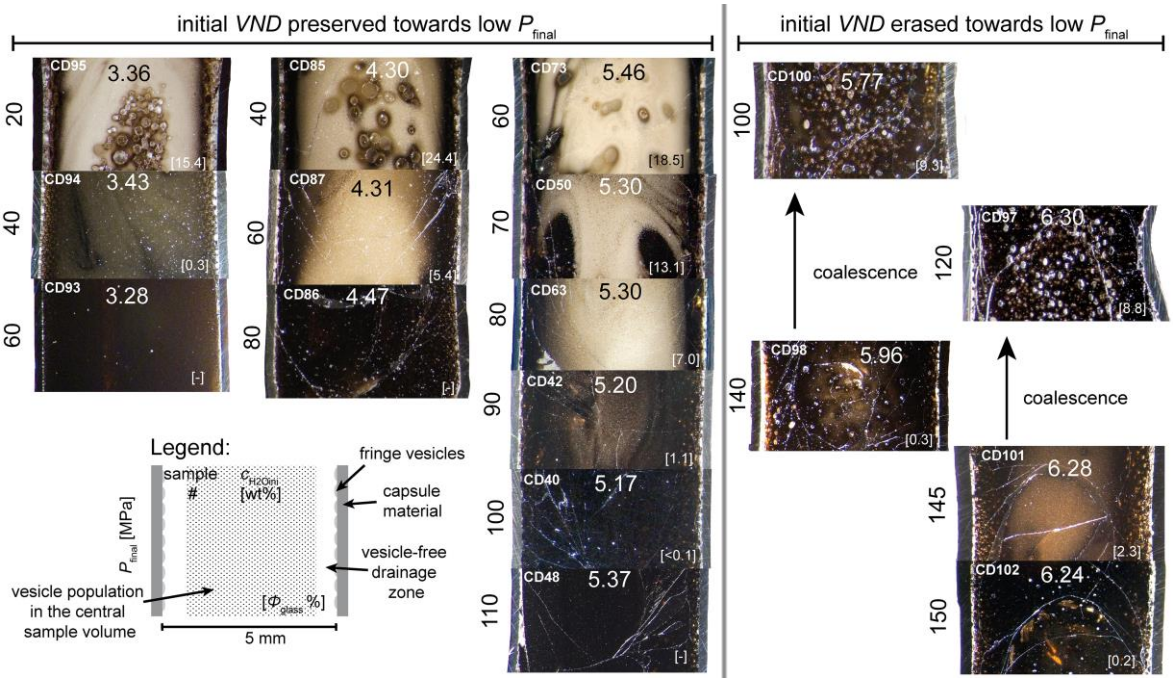

Fig. II.3 Details of reflected light images of the experimental samples of the C-series at constant decompression rate of 0.17 MPa·s^{-1}, different P_{final} and c_{H2Oini} ranging between 3.3 and 6.3 wt%. Sample images reflect the sample orientation during the experiments. For illustration purposes, not all samples of the C-series are shown. *VND*s of the samples are given in Table II.2. Full sample images are provided in the supplement "Sample images".

The central vesiculated volumes in samples with $c_{H2Oini} < 5.6$ wt% contain a high number density of homogeneously dispersed small vesicles, which are similarly-sized within each sample (further referred to as main vesicle population). In the experiments with the lowest P_{final} (CD85, CD95, CD73), some vesicles of the main population are observed to be connected to each other. Additionally, in these samples, larger vesicles are observed within the main vesicle population (Fig. II.3). Some of the large vesicles are connected to vesicle-free streaks underneath (e.g., CD73, Fig. II.3) and are surrounded completely by a vesicle-free drainage zone ~50 µm in width.

In addition to the main vesicle population, which fills most of the central sample volume, in CD87, CD85, CD91, and CD73, a population of smaller vesicles (second

population) is observed. Vesicles of the second population are located between the central vesiculated volume and the drainage zone of the capsule wall or in the drainage zone of large vesicles in CD85 and CD73 (Fig. II.4), but always close to the main vesicle population.

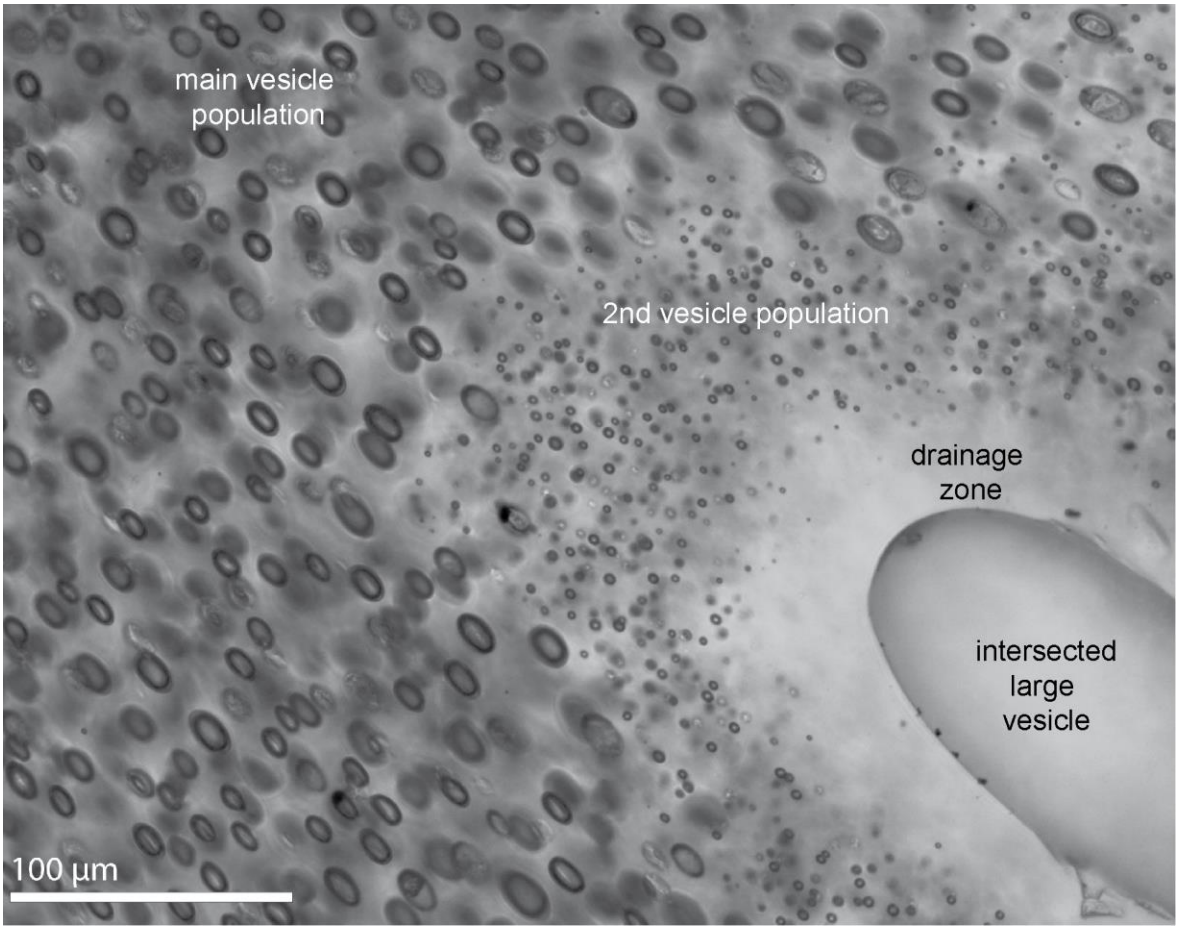

Fig. II.4 Transmitted light microscopy image of CD73 thin section in the central vesiculated sample volume. Between the main vesicle population and the intersected large vesicle, a transition zone is visible, which consists of the drainage zone of the large vesicle and a second vesicle population with a lower Φ_{glass} of 9% and higher log*VND* of 6.07 compared to the main population with log*VND* = 5.41 and Φ_{glass} of 18.5%. Black points at the edge of the large intersected vesicle are artifacts from preparation on the sample surface.

At 6.3 wt% c_{H2Oini} and a P_{final} of 150 MPa (CD102), vesicles are observable only in the top half of the sample volume at the limit of optical resolution. During further decompression, a pervasive vesiculation throughout the central capsule volume is observable in sample CD101, which was decompressed to a P_{final} of 145 MPa (bright area in the center of the sample in Fig. II.3). Eventually, at 120 MPa, less but significantly larger vesicles remain (CD97). The same pattern is observed in samples with slightly lower c_{H2Oini} of 5.96–5.77 wt%, with half of the sample vesiculated at a P_{final} of 140 MPa. At a P_{final} of 100 MPa (CD100), only

small vesicle clouds with finely dispersed vesicles are observed, while the remaining central sample volume contains a low number of large vesicles. In CD44, decompressed at high T_d of 1523 K, half of the sample volume shows finely dispersed vesicles, while the other half contains some large vesicles.

5.4 *VND* and glass porosity

A systematic dependence of *VND* with decompression rate is lacking for hydrous VAD79 melt with c_{H2Oini} of ~5.3 wt%, as already shown by Allabar and Nowak et al. (2018) for the d*P*/d*t* range of 0.024–10 MPa·s^{-1}. The additional experiment CD28 of this study, with a log*VND* of 5.05, matches with their range of log*VND* from 4.83–5.39, irrespective of decompression rate. The log*VND*s of the additional experiments performed at 1373 K ranging between 4.60 and 4.98 are lower (TD and T-series; Fig. II.5) except for one experiment with a log*VND* of 5.48 (CD59). At 1523 K (CD44), log*VND* increased to 5.87, however at slightly lower c_{H2Oini} of 4.96 wt%. The standard deviation of log*VND* is 0.26, as derived from data of the experiments performed at 1373 K and similar c_{H2Oini} of ~5.3 wt%. For experiments of the C-series with c_{H2Oini} ~5.3 wt% and different P_{final}, the standard deviation of log*VND* is 0.34. This defines an experimental error in log*VND* of ~0.3 log units that is larger than the estimated analytical error of ± 0.13 (error bars in Fig. II.5).

Significant changes in *VND* result from experiments with varying c_{H2Oini}. The highest log*VND*s of 5.96 and 6.37 are observed in samples with c_{H2Oini} of ~3.3 wt% (Fig. II.5). The log*VND* decreases to ~5 at c_{H2Oini} of 5 wt%. Towards c_{H2Oini} of ~6.3 wt%, the log*VND* increases again to ~5.8. In contrast, the *VND* keeps constant within error with decreasing P_{final} for experiments with constant c_{H2Oini} (see "Supplementary information"). Thus, the *VND* is dependent only on c_{H2Oini} and slightly on T_d. In the experimentally investigated P_{final} range, Φ_{glass} of the main population increases with decreasing P_{final} from < 0.1 to a maximum of 15.4, 24.4, and 18.5% at ~3.3, ~4.4, and ~5.3 wt% c_{H2Oini}, respectively (Table II.2).

The log*VND*s of the second population of vesicles (Table II.2) ranging between 5.66 and 6.14 are significantly higher than the log*VND* of the respective main populations of 5.41–5.45. The Φ_{glass} within the volume of the second vesicle population ranging between 0.2 and 9.0% are lower than the values of the respective main population ranging between 9.0 and 24.4%. In sample CD73, the second population shows a higher Φ_{glass} in the drainage zone of

the large vesicle (9.0%, Fig. II.4) compared to the second population located in the capsule wall drainage zone (1.0%).

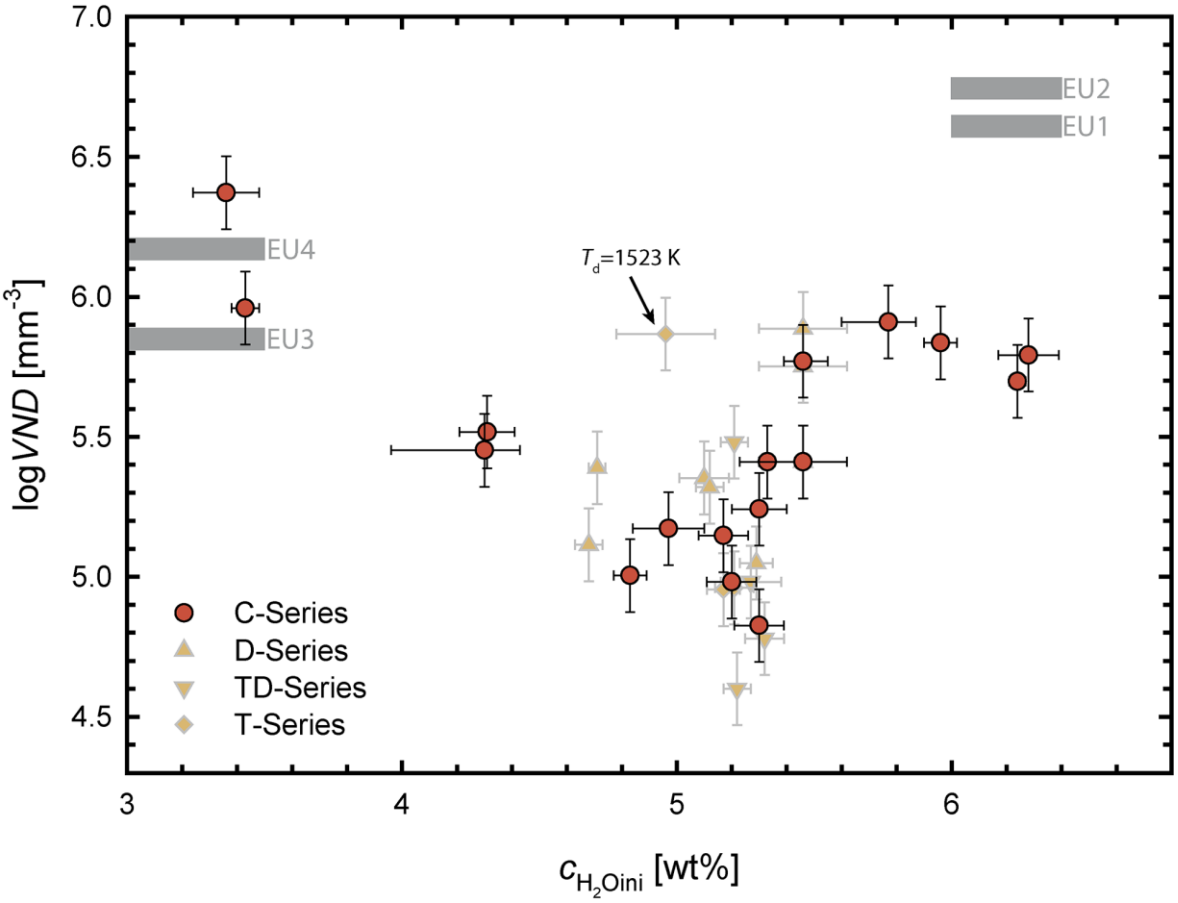

Fig. II.5 log*VND* (vesicle number density) of the main vesicle populations within the central sample volume vs. initial H_2O concentration (c_{H2Oini}). The *VND* shows a minimum at c_{H2Oini} of ~5 wt% and increases towards lower and higher c_{H2Oini} up to 1.5 log units. Experiments with various decompression rates (D-series) and similar c_{H2Oini} ranging between 4.68 and 5.46 wt% reveal no systematic change of *VND* similar to the T-series experiments with increased *T*d of 1373 K. A substantially higher T_d of 1523 K, however, results in a significantly higher log*VND*. The grey bars indicate the mean log*VND*s and the corresponding pre-eruptive H_2O concentrations derived from melt inclusions (Cioni 2000) of white (EU1 and EU2) and grey pumice (EU3 and EU4) of the AD79 Vesuvius eruption (Gurioli et al. 2005; Shea et al. 2010a).

5.5 H_2O concentrations

The H_2O concentrations as measured by FTIR (c_{H2OIR}) of the central sample volumes without observable vesicles resemble the initial $c_{H2Ograv}$. The same holds for the samples with Φ_{glass} < 5%, where the probed volume contained glass together with vesicles (e.g., CD-C-23, CD40). In three experiments, considerable weight loss occurred during welding. For two of these samples (CD102 and CD101), c_{H2OIR} is similar to $c_{H2Ograv}$, whereas CD98 has a reduced

c_{H2OIR} of 5.96 wt% as compared to the $c_{H2Ograv}$ of 6.27 wt%. In CD44, the c_{H2OIR} measured in the central vesiculated sample volume is slightly decreased to 4.96 wt% with respect to the $c_{H2Ograv}$ of 5.28 wt%. For CD85, which also experienced weight loss during welding, the porosity was too high for reliable c_{H2OIR} determination. The c_{H2OIR} measured in the volumes of the second population of vesicles are within error similar to the $c_{H2Ograv}$ in CD87, CD85, and CD91, but decreased considerably to 4.99 wt% in CD73 compared to the $c_{H2Ograv}$ of 5.46 wt%.

6. Discussion

6.1 H_2O concentrations

In experiments starting from slightly undersaturated conditions, the c_{H2Oini} is defined by the gravimetrically determined $c_{H2Ograv}$. However, since, for samples with Φ_{glass} < 5%, the c_{H2OIR} equals within error $c_{H2Ograv}$ (e.g., CD-C-23, CD40; Table II.2), c_{H2OIR} was used as the dissolved H_2O concentration in the melt prior to decompression (c_{H2Oini}). This has the advantage that uncertainties in $c_{H2Ograv}$, caused by weight loss during welding, are eliminated (e.g., CD102, CD98). The c_{H2OIR} reveal that weight loss of CD102 and CD101 resulted from Au80Pd20 loss during welding, whereas in case of CD98, some H_2O was lost. Similar to CD77 (Allabar and Nowak 2018), the c_{H2O} prior to phase separation in CD44 was already reduced as compared to the $c_{H2Ograv}$. During decompression at a higher T_d of 1523 K, the H_2O diffusivity is higher and viscosity is lower than at a lower T_d of 1323 K. Thereby, diffusional loss of H_2O into fringe vesicles, that early nucleated heterogeneously at the capsule wall during decompression, increases and ascent of fringe vesicles is facilitated. Both effects reduce H_2O supersaturation within the central sample volume, similar to CD77 with a low decompression rate of 0.024 MPa·s^{-1} (Allabar and Nowak 2018). However, in both samples, a reduced but constant c_{H2OIR} was measured in the central vesiculated sample volume, which was therefore used as c_{H2Oini}.

For CD100, a mean c_{H2OIR} of 5.43 wt% was measured in various small vesicle clouds. Because the vesicle clouds of the main vesicle population are only small (~0.1 mm^3), it may be possible that after phase separation of the main vesicle population, H_2O was lost into large vesicles which are located close to the small vesiculated melt volumes, driven by Ostwald ripening. Because CD98 with a similar c_{H2Oini} shows that the melt was vesiculated by the main population at higher P_{final}, it is suggested that the high *VND* observed in the small vesicle

clouds in CD100 represents the product of a phase separation at the initial c_{H2O}. Therefore, c_{H2Oini} of 5.77 wt% is assumed for CD100.

In decompression experiments that started from H_2O supersaturated conditions after hydration (e.g., CD83 and CD73), c_{H2Oini} is defined by the H_2O solubility at P_{start} and T_d. Solubility data for hydrous VAD79 melt at T_d and P_{start} were derived from Iacono-Marziano et al. (2007) and Marxer et al. (2015). The $c_{H2Ograv}$, c_{H2OIR}, and H_2O solubility data that were used as c_{H2Oini} are highlighted in bold numbers in Table II.2.

Results of c_{H2OIR} measurements in the glass between vesicles are presented in Allabar et al. (2020b). These data are not used for further discussion here, because the c_{H2OIR} of the glass between vesicles does not represent c_{H2O} dissolved in the melt at P_{final} prior to quench due to H_2O resorption from the fluid phase back into the melt during quench (McIntosh et al. 2014; Allabar et al. 2020b).

6.2 Phase separation

6.2.3 Verification of homogeneous phase separation

With the decompression experiments compiled and performed for this study, it is intended to investigate homogeneous phase separation of hydrous phonolitic melt. Therefore, it is necessary to verify a single-phase superliquidus system at the onset and during decompression until vesicle formation starts in the central volume of the sample. The use of a ZrO_2 ball mill for synthesis of the starting glasses VAD79_03–10 caused ZrO_2 contamination of 1000–1200 ppm, while the use of a corundum ball mill for synthesis of VAD79_12 yields a lower ZrO_2 contamination of 600 ppm ZrO_2. ZrO_2 saturation caused by ZrO_2 contamination could lead to pre-existing ZrO_2 or $ZrSiO_4$ crystals or ZrO_2 rich domains on a mesoscopic scale (e.g., Cormier et al. 2015; Dargaud et al. 2011). Zr-phases may act as vesicle nucleation sites, favoring heterogeneous nucleation of vesicles during decompression. However, a ZrO_2 solubility of 3660 ppm was calculated for dry VAD79 melt composition at 1323 K using the model of Gervasoni et al. (2016). The ZrO_2 solubility increases linearly with H_2O concentration up to 2 wt% and remains constant towards higher c_{H2O} in granitic melts at high T (Watson and Harrison 1983). Assuming a similar dependence in phonolitic melt, the measured ZrO_2 concentrations in the starting glasses are far below the ZrO_2 saturation limit. Furthermore, pre-existing crystals in the starting glasses or crystal formation during

degassing caused by ZrO_2 contamination were not observed by TLM or SEM-BSE imaging. Experimental samples with high and low ZrO_2 contamination with identical decompression conditions of c_{H2Oini} ~5.3 wt%, dP/dt of 0.17 MPa·s^{-1}, and P_{final} of 80 MPa reveal similar *VND*s. The samples CD63 (starting glass VAD79_07) and CD91 (starting glass VAD79_12) reveal log*VND*s of 5.24 and 5.41, respectively.

Aside from Zr-phases, Fe-oxide crystals may form during the decompression experiments at the lowest T_d of 1323 K. Surfaces of magnetite crystals reduce efficiently the energy and the supersaturation pressure required for H_2O vesicle nucleation (e.g., Hurwitz and Navon 1994; Shea 2017). H_2O solubility experiments of Iacono-Marziano et al. (2007) reveal that at P between 250 and 30 MPa, the phase boundary of Fe-oxides for VAD79 melt is between 1323 and 950 K. This is supported by the synthesis of hydrous reference VAD79 samples of Marxer et al. (2015) at 1323 K, 200-75 MPa and intrinsic oxygen fugacity of ΔlogQFM = + 3.5. BSE images reveal that these glasses are free of µm-sized Fe-oxide crystals. Phase equilibria experiments with hydrous CI melts of similar composition, determined by Fabbrizio and Carroll (2008) at ΔlogNNO = + 0.8, reveal liquidus temperatures higher than 1143 K and 1133 K for P of 50 and 200 MPa, respectively. However, experiments at T > 1143 K that are required to bracket the phase boundary for the liquidus phase magnetite are lacking. Fanara et al. (2012) performed phase equilibria experiments with hydrous CI melt in an IHPV at intrinsic ΔlogQFM = + 3.5. The liquidus temperature, defined by the phase boundary of magnetite, is between 1273 and 1323 K for H_2O activities between 1 and 0.5 and a P of 200 MPa. These data show that for hydrous VAD79 melt, the phase boundary of magnetite may be close to the lowest decompression temperature of 1323 K.

Another driving mechanism for decompression-induced vesicle formation in hydrous melt might be heterogeneous nucleation at nanometer-sized Fe-oxide crystals (ultra-nanolites smaller than 30 nm and nanolites 30 nm to 1 µm as classified by Mujin et al. 2017), as suggested by, e.g., Di Genova et al. (2017a,b; 2018) and Shea (2017). Such nanolites are observed in natural volcanic products. The formation of Fe-oxide nanolites can be related to pre-, syn-, and post-eruptive processes. Post-eruptive Fe-oxide nanolites are observed in glass particles of welded tuff (Schlinger and Smith 1986; Schlinger et al. 1988) and in natural obsidian glasses (Sharp et al. 1996). Fe-oxide nanolites related to syneruptive processes are observed in dense juvenile fragments of lava derived from a 2011 sub-plinian andesitic-dacitic eruption of Shinmoedake (Mujin and Nakamura 2014 and Mujin et al. 2017). Fe-

oxide nanolites at and near vesicle surfaces of Mt Etna ashes might be related to syn- and posteruptive processes (Barone et al. 2016). Furthermore, Di Genova et al. (2017a; b; 2018) observed Fe-oxide nanolites in experimental and natural hydrous silicate glasses.

Fe-oxide nanolites potentially drive heterogeneous vesicle nucleation that may have been overlooked in previous studies of Iacono-Marziano et al. (2007), Marxer et al. (2015) Preuss et al. (2016) and Allabar and Nowak (2018), because this mechanism may mimic homogeneous phase separation. Fe-oxide nanolites may form during thermal equilibration prior to decompression and during decompression and degassing of hydrous VAD79 melt. Nanolite formation might be induced by thermodynamic metastability or instability of H_2O supersaturated melt and by increasing liquidus temperature with decreasing H_2O content.

However, the RMS measurements (Fig. II.2) prove that the selected quenched hydrous VAD79 samples are free of Fe-oxide nanolites. The minimum decompression temperature of 1323 K for our VAD79 experiments is sufficiently high to inhibit Fe-oxide nanolitization prior to and during decompression and phase separation, and during cooling the samples. This holds even for the sample CD95 with the lowest c_{H2Oini} of 3.36 wt% c_{H2Oini} and P_{final} of 20 MPa (Fig. II.1) that experienced a T drop of 50 K at the end of decompression. Thus, the vesicle formation in hydrous VAD79 melt is not affected by Fe-oxide nanolitization.

In contrast to the VAD79 samples, the CI samples containing 4.87 and ~3.2 wt% H_2O (Preuss et al. 2016) show distinct Raman bands at ~680 cm^{-1}, indicative of Fe-oxide nanolites. However, both hydrous melt compositions reveal log*VND*s in the same order of magnitude of 4.83–5.92 during decompression, independent of decompression rate (Preuss et al. 2016; Allabar and Nowak 2018) and independent of the occurrence of Fe-oxide nanolites in the quenched glasses. This suggests that (1) the Fe-oxide nanolites, detected in hydrous Campi Flegrei trachytic glass samples of Preuss et al. (2016), formed after decompression and vesicle formation during rapid isobaric quench within the metastable field of the hydrous supercooled melt or (2) that Fe-oxide nanolites in CI melts formed prior to phase separation, e.g., deep within the metastable field of supersaturated melt, and mimic homogeneous vesicle formation.

We conclude that heterogeneous vesicle nucleation at low supersaturation occurred only at the interface of capsule walls and melt as an experimental artifact (fringe vesicles) in our samples. A vesicle-free drainage zone evolved between fringe vesicles and the central sample volume by diffusional H_2O loss into fringe vesicles during further decompression

after their formation. If heterogeneous nucleation had also formed the observed vesicles in the central sample volume, this vesicle-free drainage zone would be smaller due to much lower supersaturation P required for heterogeneous nucleation and the shorter time available for H_2O diffusion into fringe vesicles (Allabar and Nowak 2018). At a ΔP_{het} (difference between saturation P and pressure of heterogeneous vesicle nucleation) of ~5 MPa that is suggested for nucleation at magnetites (Hurwitz and Navon 1994; Shea 2017), the drainage zones would be only ~120 µm for 6.3 wt% c_{H2Oini} to ~75 µm at 3.3 wt%. The observed drainage zone width of 650 and 250 µm, respectively, is indicative of homogeneous phase separation at larger supersaturations at the pressure at which phase separation starts (P_{hom}). Finally, for heterogeneous nucleation, a dependence of *VND* on dP/dt, as predicted by nucleation theory, is still expected (Shea 2017; Allabar and Nowak 2018). However, this is not observed in hydrous phonolitic melt.

In summary, in the decompression experiments of this study and in the published experiments compiled in this study, it is ensured that homogeneous phase separation by vesicle formation occurred in the central volume of the samples as close to the terminus as possible. Therefore, only the main vesicle population was considered for characterization of homogeneous phase separation by quantitative *VND* analysis.

6.2.4 Homogeneous phase separation

Homogeneous phase separation occurred in the central volume of the samples where the c_{H2Oini} was preserved and not affected by diffusional H_2O loss towards heterogeneously nucleated vesicles at the capsule walls. Allabar and Nowak (2018) showed that an independence of *VND* on decompression rate cannot be explained by nucleation theory, but is consistent with the theory of spinodal decomposition.

For vesicle nucleation, a continuous increase of *VND* with decreasing P_{final} is expected until a sufficiently high number of vesicles is formed to decrease supersaturation below a threshold value for further nucleation. This leads to a broadening in vesicle size distribution towards low decompression rates (Shea et al. 2010b). However, the observed independence of *VND*s with decreasing P_{final} at constant c_{H2Oini}, the similarly-sized vesicles in the central sample volume within each experiment (see VVD-plots in the "Supplementary information"), and the independence of *VND* from decompression rate (Allabar and Nowak 2018) indicate that the formation of vesicles is inconsistent with nucleation theory. It is

suggested that off-critical spinodal decomposition is a potential phase separation mechanism in H_2O supersaturated phonolitic melt (Allabar and Nowak 2018). Spinodal decomposition is a non-activated spontaneous process at the spinode, i.e., at the thermodynamic limit of metastability (e.g., Cahn and Hillard 1959; Cahn 1965). Thermally induced spatial concentration (c) fluctuations are attenuated by downhill diffusion in the metastable state, where the second derivative of the free energy of mixing (ΔG) $\partial^2\Delta G/\partial c^2$ is > 0. In the unstable state, however, where $\partial^2\Delta G/\partial c^2$ is < 0, the concentration fluctuations are amplified by uphill diffusion until sharp phase boundaries between hydrous silicate melt and an H_2O-rich fluid phase evolve (Debenedetti 2000; Tanaka et al. 1990).

A quantitative approach, based on the theory of spinodal decomposition, to explain the observed minimum of *VND* at a c_{H2Oini} of ~5 wt% (Fig. II.5) is difficult, because H_2O is a reactive component in silicate melts. The volatile component H_2O dissolves mainly as hydroxyl groups and as some molecular H_2O, which was demonstrated by in-situ measurements of hydrous aluminosilicate melt (Nowak and Behrens 1995; Nowak and Behrens 2001). The polycondensation reaction 2(Si,Al)-OH = (Si,Al)-O-(Si,Al) + H_2O produces molecular H_2O during phase separation and is accompanied by an exothermic reaction enthalpy (Nowak and Behrens 2001), in addition to the enthalpy and entropy of mixing. Thus, the phase separation cannot be quantified by a simple regular solution model as conceptually presented by Allabar and Nowak (2018). However, a sound physicochemical quantification of spinodal phase separation of hydrous phonolitic melt is beyond the scope of this study. Regardless of these limitations, a qualitative justification for the observed dependence of *VND* on c_{H2Oini} is possible for two different assumptions:

(1) It is possible that the observed *VND* is defined by the wavelength of concentration fluctuations that are amplified during spinodal decomposition. In this case, vesicles are formed one wavelength apart from each other. Such a case is described for droplet-type spinodal decomposition, which is possible when the volume fraction of the minor phase, H_2O in the case of hydrous melt, is < 15% (Cahn 1965). The critical (i.e., minimum) wavelength (λ_c) that is amplified when a system becomes unstable is $\lambda_c = 2\pi/\beta_c$, where the critical wavenumber β_c is defined as (Cahn 1965):

$$\beta_c = \left(\frac{-\partial^2 \Delta G/\partial c^2}{2\kappa}\right)^{\frac{1}{2}} \quad \text{(II.1)}$$

where κ is a positive constant and the numerator term is the curvature of the free energy curve as a function of composition at given P and T. The wavenumber, at which amplification is maximum, is $\beta_m = \beta_c/(2^{0.5})$. Consequently, at given P and T, the wavelength of successfully amplified concentration modulations, which may be associated with the observed *VND*, depends on composition, i.e., on the H_2O concentration. In our experiments, not only the c_{H2Oini} is varied, but as a consequence, also the P_{hom}. This could lead to the increase of *VND* towards high and low c_{H2Oini}. The higher T of 1523 K of CD44, compared to all other experiments, could have induced a similar change in curvature of the free energy curve as the increase or decrease in c_{H2Oini}, leading to a higher *VND* (Fig. II.5).

(2) Alternatively, the *VND* observed in the experimental samples may be the result of textural coarsening of fractal ramified structures (Cahn 1965) of the two phases, into which the hydrous melt may have separated by spinodal decomposition. Since the samples that were quenched at different P_{final} show similar *VND*s at constant c_{H2Oini}, there might be a stable *VND* at which coarsening stops. Coarsening likely depends on melt viscosity, surface tension, and H_2O diffusivity, which are all parameters that depend on H_2O concentration. This could result in the varying *VND* with changing c_{H2Oini}.

6.3 Evolution of degassing

For all vesiculated samples, Φ_{glass} is smaller than the calculated Φ_{equ} at P_{final} and T_d (Allabar et al. 2020b). At first sight, this suggests disequilibrium degassing during decompression. However, diffusion calculations reveal that near equilibrium must have been approached in all experiments due to sufficiently high H_2O diffusivity and small inter-vesicle distances at a 10 μm scale (Allabar et al. 2020b). Only for the samples with ~3.3 wt% c_{H2Oini}, degassing close to equilibrium is not ensured during decompression to P_{final} (Allabar et al. 2020b). For all other experiments, the low Φ_{glass} compared to Φ_{equ} is suggested to be related to vesicle shrinkage during isobaric cooling caused by the decrease of the molar volume of the H_2O fluid during cooling (Marxer et al. 2015), accompanied by resorption of H_2O from fluid vesicles back into the melt (McIntosh et al. 2014) due to increasing H_2O solubility with decreasing T (e.g., Schmidt and Behrens 2008). The suggestion of significant vesicle shrinkage

is supported by the observation of strongly deformed fringe vesicles. Vesicle shrinkage during cooling of the samples from this study is in detail explained in Allabar et al. (2020b). However, the c_{H2Oini}-dependent *VND*s and coalescence processes can be discussed here, without considering vesicle shrinkage.

At c_{H2Oini} < 5.6 wt%, the initially formed *VND* of the vesicles of the main population remains stable during decompression to low pressure until Φ_{melt} is sufficiently large for the onset of coalescence, as observed in the experiments with P_{final} of 20, 40, and 60 MPa with 3.36 (CD95), 4.30 (CD85), and 5.46 wt% (CD73) c_{H2Oini}, respectively (Fig. II.6). It can be excluded that the larger vesicles observed in the central part of the samples are due to pre-existing vesicles that might result from air vesicles in the glass cylinders used for the decompression experiments (Preuss et al. 2016). In this case, the vesicle-free drainage zone around these vesicles should be as wide as the drainage zone towards the capsule wall, which is not the case (Fig. II.3). In CD95, the drainage zone towards fringe vesicles at the capsule wall is ~400 µm, while the distance between the walls of large vesicles and the main population is only ~50 µm. This suggests that the large vesicles in the central volume of the samples may be former fringe vesicles that detached from the capsule walls and ascended through the melt during further decompression and degassing. Vesicle-free streaks, indicating the ascent track of these vesicles, are visible, e.g., in CD73 (Fig. II.3). However, in CD95 and CD85, large vesicles are isolated in the center of the samples and surrounded by small vesicles. Ascent tracks below these large vesicles are not visible. Additionally, the observation that at P_{final} > 20 and > 40 MPa large vesicles are not present in central sample volumes with c_{H2Oini} of 3.3 and 4.3 wt%, respectively, argues for coalescence, forming the large vesicles from the main vesicle population at the lowest P_{final}. Assuming Φ_{equ} (calculated after Gardner et al. 1999, Equation 5 therein) prior to quench (Allabar et al. 2020b), it can be concluded from the experimental observations that coalescence and the linked reduction of *VND* of the main vesicle population starts at similar Φ_{melt} of 30–50%, 30–40%, and 35–40%, at 3.3, 4.3, and 5.3 wt% c_{H2Oini}, respectively. Note that the Φ_{melt} values for 3.3 wt% c_{H2Oini} are prone to the uncertainty whether near-equilibrium degassing occurred in CD95 (Allabar et al. 2020b). In case of disequilibrium degassing, the Φ_{melt} at the onset of coalescence would be lower.

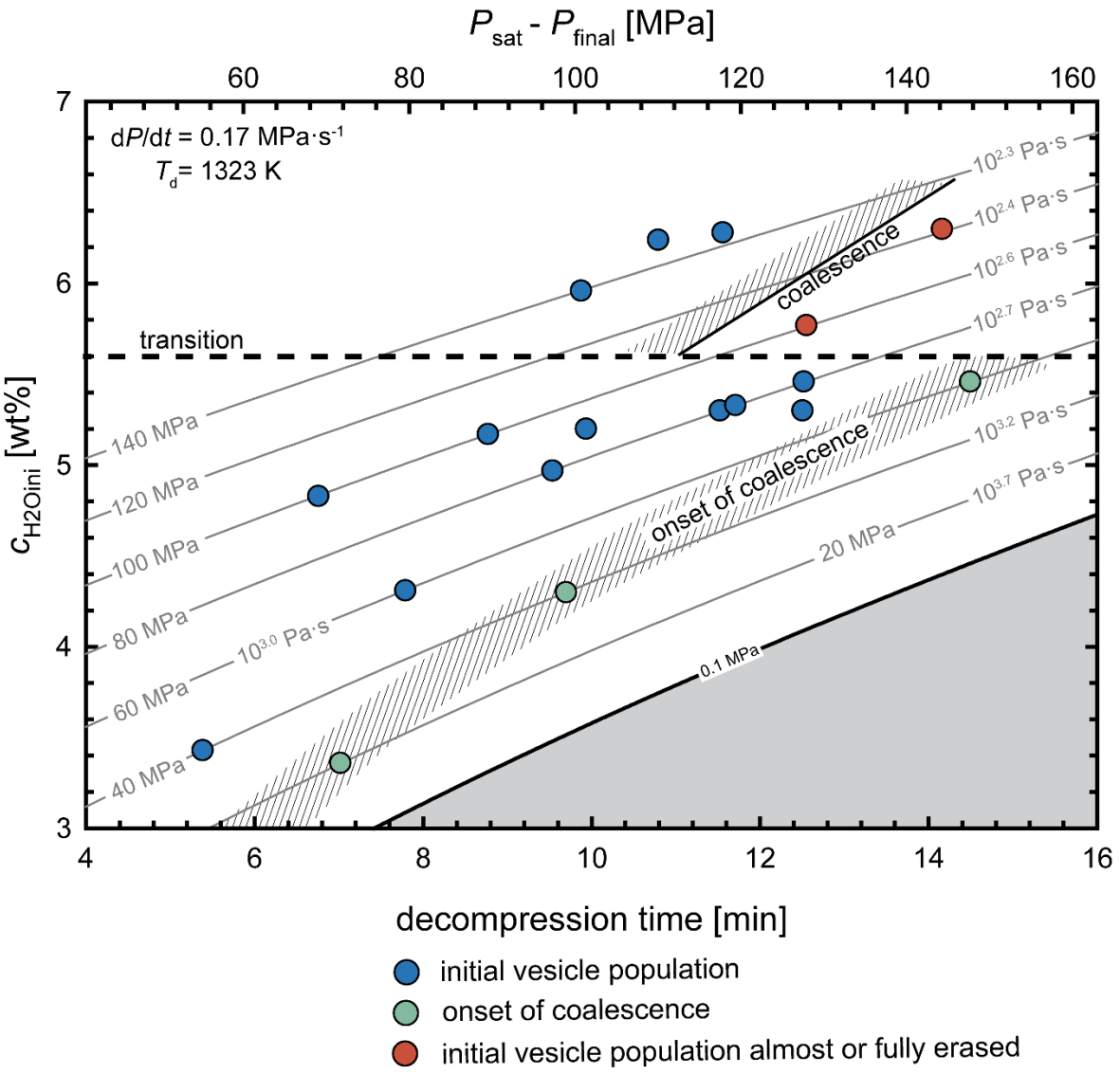

Fig. II.6 Experimental parameters and textural features of the C-series plotted for initial H_2O concentration (c_{H2Oini}) vs. decompression time [(saturation pressure (P_{sat}) - final pressure (P_{final}))/(dP/dt)] for a dP/dt of 0.17 MPa·s^{-1} and a decompression temperature of 1323 K. The grey lines indicate the P_{final} in MPa and the corresponding melt viscosity in case of equilibrium degassing calculated after Giordano et al. (2008). The colors of symbols indicate the stage of vesicle coalescence observed in the experiments. A transition in degassing evolution occurs at c_{H2Oini} of 5.6 wt%. Below 5.6 wt% c_{H2Oini}, the initial *VND* (vesicle number density) is preserved to relatively low P_{final} until the onset of coalescence is observed. In this case, the *VND* is likely preserved until magma ejection to the surface in case of a natural system, where decompression rate accelerates while degassing proceeds (Proussevitch and Sahagian 1996). Note that equilibrium degassing is not ensured in the experiment decompressed with c_{H2Oini} of ~3.3–20 MPa (Allabar et al. 2020b). Thus, the actual melt viscosity may be slightly lower than the given value for equilibrium c_{H2O} for this experiment. At c_{H2Oini} > 5.6 wt%, vesicle coalescence occurs at higher (P_{sat} - P_{final}), i.e., higher c_{H2O} and lower melt viscosity. *VND* is significantly reduced and during further decompression it is likely that H_2O supersaturation builds up in interstitial melt volumes due to large inter-vesicle distances, causing a possible second phase separation event at c_{H2O} < c_{H2Oini}.

The vesicles of the second population formed when H_2O diffusion into the large vesicles or fringe vesicles and towards the opposite side into vesicles of the main population was not fast enough to effectively reduce the H_2O supersaturation that had built up during further continuous decompression. This led to a secondary homogeneous phase separation event at $c_{H2O} < c_{H2Oini}$ and lower P_{final} as compared to the main vesicle population, resulting in lower Φ_{equ} and consequently lower Φ_{glass}. The log*VND* of the second population is 0.21–0.69 log units higher than the log*VND* of the respective main population. This is consistent with an increase of *VND* towards lower c_{H2O} of the melt just prior to phase separation (Fig. II.5).

However, this observation contrasts with the measured c_{H2OIR} of the volumes of the second population, which mostly reflects within error the c_{H2Oini} (Table II.2). The measured c_{H2OIR} could in this case overestimate the c_{H2O} of the melt at phase separation. As described in Allabar et al. (2020b), H_2O is resorbed from the fluid back into the melt during quench. As a result, the $c_{H2Omelt}$ at T_d and P_{final} is lower than $c_{H2Oglass}$ between vesicles at ambient conditions. In the large volume of the main vesicle population, the H_2O is resorbed rapidly into the melt from the vesicles during cooling due to short inter-vesicle distances on a 10 µm scale. Thus, the measured c_{H2OIR} is expected to reflect the c_{H2Oini} and thus the c_{H2O} at phase separation. In the small volume of the second population, which is always located close to the main vesicle population, H_2O may not only be resorbed from the vesicles of the second population but also from the main population into the melt volume of the second population. As a result, the measured c_{H2OIR} in the glass is higher than the c_{H2O} at phase separation.

At c_{H2Oini} of 5.6 wt% a transition is observed in the degassing evolution during decompression (Fig. II.6). At $c_{H2Oini} > 5.6$ wt%, the initial *VND* of the main population is only observable for a short *P* interval of, e.g., ~20 MPa at 6.3 wt% c_{H2Oini}. In CD102 ($P_{final} = 150$ MPa), only in half of the sample, vesiculation is observable at very low Φ_{glass}, which is first due to the large drainage zone at high c_{H2Oini}, that is better visible in CD101 (Fig. I.3) due to the higher Φ_{glass}. Second, vesicles in CD102 could have shrunk and H_2O may have been resorbed back into the melt during cooling (Allabar et al. 2020b), so that this experiment may be at the very limit of vesicle observation for the used quench rate. During decompression from 150 to 145 MPa (CD101), the initially observed log*VND* remains stable at ~5.7. During further decompression to 120 MPa, the main vesicle population is completely erased by coalescence and a low log*VND* of 1.92 remains (CD97) at decompression times ($(P_{sat} - P_{final})/(dP/dt)$) at which the initial *VND* is still observed at $c_{H2Oini} < 5.6$ wt% (Fig. II.6).

The P range of 145–120 MPa, during which *VND* drastically decreases at 6.3 wt% c_{H2Oini}, corresponds to Φ_{melt} (= Φ_{equ}) between 15 and 21% for equilibrium degassing of the homogeneously formed vesicles of the main population. Therefore, coalescence occurs at much lower melt porosities and to a greater extent at 6.3 wt% compared to c_{H2Oini} < 5.6 wt%. In experiments with c_{H2Oini} < 5.6 wt%, where the onset of coalescence is observed at 20, 40, and 60 MPa with increasing c_{H2Oini}, logη (in Pa·s) calculated for equilibrium c_{H2O} at 1323 K is 3.7, 3.2, and 3.0 (Giordano et al. 2008), respectively (Fig. II.6). Note that the first value for 3.3 wt% c_{H2Oini} may be lower in case of possible disequilibrium degassing. Beyond the transition at c_{H2Oini} of 5.6 wt%, the initial vesicle population is already completely erased at lower decompression time, i.e., lower logη of 2.4–2.6. The early onset of coalescence at c_{H2Oini} > 5.6 wt% is attributed to the lower viscosity with increased c_{H2O}. Decreasing viscosity favors coalescence (e.g., Fortelný et al. 1999). Consequently, at a decompression rate of 0.17 MPa·s^{-1}, the initial *VND* cannot be preserved during further continuous decompression.

6.4 Implications for volcanic eruptions

During the 79AD Vesuvius eruption, grey (tephriphonolite) and white (phonolite) pumice were ejected and are recorded in distinct eruptive units (EU) (e.g., Cioni et al. 1995). One may assume that small differences in bulk composition between white and grey pumice do not significantly influence the degassing behavior, as shown by Preuss et al. (2016) for VAD79 white pumice and trachytic CI composition.

For the melt that formed the natural Vesuvius white pumice, a c_{H2Oini} of 6.0–6.4 wt% was determined in melt inclusions in samples of eruptive unit 2 (EU2) (Cioni 2000). For EU1, pre-eruptive H_2O concentration data are lacking. However, chemical bulk compositions of EU1 and EU2 are similar, and a homogeneous H_2O distribution in the magma that formed the white pumice is assumed (Shea et al. 2014). Therefore, the c_{H2Oini} of EU1 is suggested to be similar to EU2. The log*VND* in the white pumice ranges from 6.41 to 6.89 in EU1 and 6.38–7.08 in EU2 with mean values of 6.61 and 6.74, respectively (Shea et al. 2010a; Gurioli et al. 2005; Fig. II.5). However, pre-eruptive T was ~1100–1200 K (Shea et al. 2009), well below the experimental temperatures, which results in partial crystallization and a higher melt viscosity by one log unit (Giordano et al. 2008) at the given c_{H2Oini}.

EU1 and EU2 reveal higher *VND*s than the experimental initial *VND* for similar c_{H2Oini} (Fig. II.5). Furthermore, in the experiments with c_{H2Oini} > 5.6 wt%, the initial main population

is erased at relatively high *P* during decompression at 1323 K (Fig. II.6). However, at the lower magmatic temperature, it is possible that coalescence is shifted to lower *P*, due to higher viscosity compared to the superliquidus decompression experiments. Thus, the high *VND* in EU1 and EU2 may still represent the main vesicle population. Two possible scenarios may explain the high *VND* in natural white pumice, both considering pre-existing vesicles prior to homogeneous phase separation (Allabar and Nowak 2018), because vesicles may heterogeneously nucleate at low supersaturation (Hurwitz and Navon 1994; Shea 2017) on crystal surfaces in a subliquidus melt. These pre-existing vesicles drive buoyant acceleration of magma ascent and decrease melt c_{H2O} in their vicinity by H_2O diffusion. The assumption of a pre-existing vesicles number density, which equals the crystal number density of up to 0.3 mm^{-3} (Iacono-Marziano et al. 2007; Allabar and Nowak 2018), results in a limiting decompression rate for homogeneous phase separation of 0.06 $MPa \cdot s^{-1}$ for a magma with c_{H2Oini} of 6.3 wt% and *T* of 1150 K. In the first scenario, at decompression rates > 0.06 $MPa \cdot s^{-1}$, the initial c_{H2O} is preserved in interstitial melt volumes. The observed *VND* of natural white pumice would represent the initial *VND* of homogeneous phase separation that was preserved during magma ascent to the surface. This requires that at lower *T* of ~1150 K, the initially formed *VND* at c_{H2Oini} of ~6 wt% *VND* is higher than observed in experiments at 1323 K.

In the second scenario, at decompression rates < 0.06 $MPa \cdot s^{-1}$, the pre-existing *VND* is sufficient to reduce H_2O supersaturation to prevent homogeneous phase separation at high c_{H2O}. The *VND* of white pumice suggests vesicle formation at decreased c_{H2O} values of < 3.3 wt%, at which homogeneous phase separation produced a high *VND*, consistent with the experimental results. In both scenarios, initial and second phase separation events occur that lead to a bimodal vesicle size distribution, as observed in natural products (e.g., Gurioli et al. 2005), and indicate two decompression and vesiculation stages.

The eruptive units EU3 and EU4 consist of grey pumice with a c_{H2Oini} of 3–3.5 wt% (Cioni 2000; Shea et al. 2014). The log*VND*s range from 5.15 to 6.57 in EU3 and 5.97–6.30 in EU4 with mean values of 5.84 and 6.18, respectively (Gurioli et al. 2005; Fig. II.5). Due to a pre-eruptive magma *T* of ~1323 K (Cioni et al. 1995) for the grey pumice, the *VND*s are comparable to our experimental results and are in good agreement with the experimentally derived *VND*s (Fig. II.5). Thus, we suggest that the high *VND*s in the natural grey pumice represent the initially formed vesicle population that is preserved down to 0.1 MPa and causes

porosities up to 80% (Shea et al. 2012) until open system degassing commences. In the superliquidus continuous decompression experiments of this study, the onset of coalescence in samples with c_{H2Oini} of 3.3 wt% was already observed at 20 MPa during decompression with 0.17 MPa·s^{-1} (Fig. II.6). However, in a natural system, decompression rate increases at the onset and during vesiculation by increasing buoyancy of the melt with decreasing density. Thus, the time available for coalescence decreases and the initial *VND* is likely preserved until the magma reaches the surface.

Previously, it has been shown that under the assumption of homogeneous nucleation, extreme decompression rates of 50–55 MPa·s^{-1} would be necessary to explain the observed high *VND*s in grey pumice. Therefore, it has been suggested that heterogeneous nucleation on oxides caused the high *VND* observed in grey pumice, for which decompression rates of 2.35–11.53 MPa·s^{-1} were calculated (Shea et al. 2012). Contrary to that, an alternative explanation is phase separation by spinodal decomposition that may have formed the high *VND*. Micro-phenocrysts, mainly leucite, with high number densities of ~10^4 formed during degassing (Shea et al. 2012) and are, therefore, not considered as sites for heterogeneous nucleation. Furthermore, we assume that although chlorine is an additional component (~0.6–0.8 wt%, Shea 2014) in natural VAD79 magma, the experiments of this study, with solely H_2O as volatile component, may be comparable with the natural system, because a non-volatile behavior of chlorine during the AD79 Vesuvius eruption is observed (Shea et al. 2014). Therefore, the solubility of H_2O in phonolitic-trachytic melt is not largely affected by such low chlorine concentrations (Webster et al. 2014). According to our experimental data, we suggest that 0.17 MPa·s^{-1} is sufficient to form ~10^6 mm^{-3} vesicles by spinodal decomposition before the onset of an explosive eruption and ejection of the grey pumice.

7. Conclusion

In addition to the decompression rate independent *VND* (Allabar and Nowak 2018) in superliquidus phonolitic melt, the high *VND* and their dependence on c_{H2Oini} found in this study are also compatible with the theory of spinodal decomposition. However, definite evidence and a quantitative description for this phase separation mechanism are still lacking.

The *VND* finally observed in volcanic products is, particularly for high c_{H2Oini}, likely an obscured product of initial vesicle formation, coalescence, ripening, and secondary phase separation processes in interstitial melt volumes. The resulting vesicle texture depends on

parameters such as melt viscosity and the available timescale, i.e., decompression rate before and during fragmentation and quench. From the comparison of experimental results with natural pumices of the AD79 eruption, the high *VND* in natural products may be explained by homogeneous spontaneous phase separation as in the experiments of this study. However, although the high temperature experiments of this study are not fully comparable with the VAD79 eruption, they may be similar to the recent magma conditions of Vesuvius. In the last 20 ka, the magma temperature of Vesuvius has continuously increased from ~1100 to > 1373 K (Scaillet et al. 2008). Therefore, the results of this study may be useful for the interpretation of future Vesuvius eruptions and eruptions of other volcanoes with phonolitic and trachytic superliquidus melt.

8. Supplement

8.1 Supplementary information

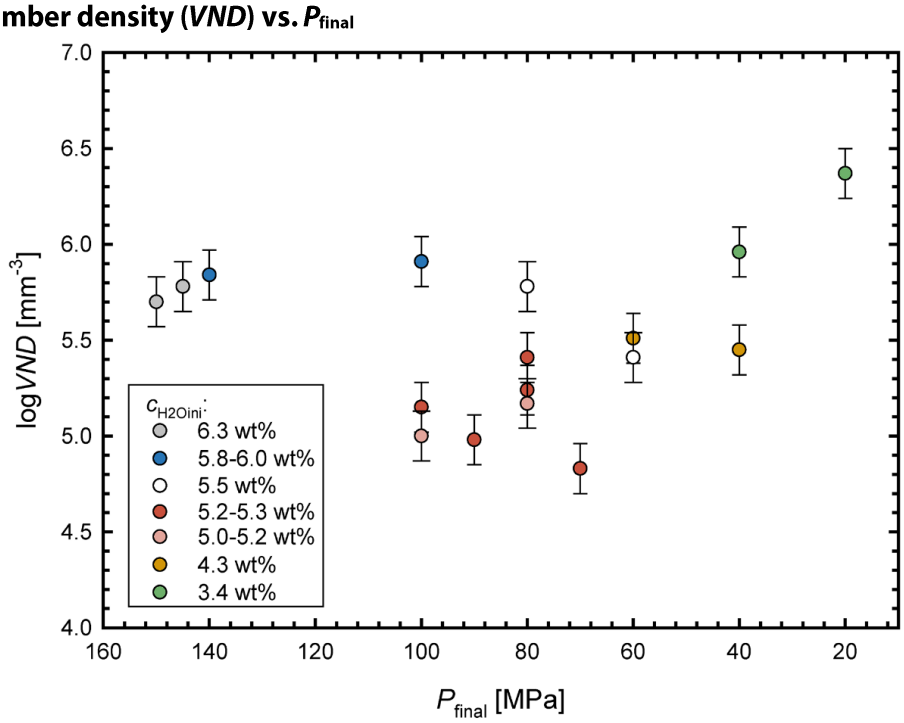

Fig. II.A1 log*VND* of the C-series (Table 1 in the main paper) with different initial H_2O concentrations (c_{H2Oini}) vs. final pressure (P_{final}), at which samples were quenched. Experiments of the C-series were hydrated at 200 MPa (< 5.3 wt% c_{H2Oini}) or 270 MPa (> 5.3 wt% c_{H2Oini}), then decompressed with 0.17 MPa·s^{-1} to P_{final} and isobarically quenched with 44 K·s^{-1}. Within each experimental set with experiments of similar c_{H2Oini}, no distinct dependence of log*VND* with P_{final} is observed.

Vesicle volume distributions

In the following, the vesicle volume distribution histograms of samples analyzed with quantitative image analysis ("CSDCorrections"; Higgins 2006) are presented. For analysis with CSDCorrections, a logarithmic size scale with the base 10 and 5 bins per decade was chosen, as recommended by Higgins (2006). With this setting each size interval has the 1.6 fold width of the previous interval and all intervals appear with the same width on a logarithmic scale. The fabric was set to massive and the measurement of the vesicle was set to the ellipse major axis. The aspect ratios for the short and long axes of the ellipses were automatically taken from the ImageJ results. The middle (inter-) axis was set to the average value of long and short axis length, as recommended by Marxer et al. (2015). In the following plots, the volume fraction of each size interval is plotted vs. vesicle size (l), which is attained by stereological calculations. The data refers to the initial main population observed in the central sample volume. Only in case of "CD97 coalesced" and "CD100 coalesced", the data are from analysis of the vesicle population after the initial vesicle number density was significantly reduced by coalescence (see main manuscript and data in Table II.2 therein).

C-series

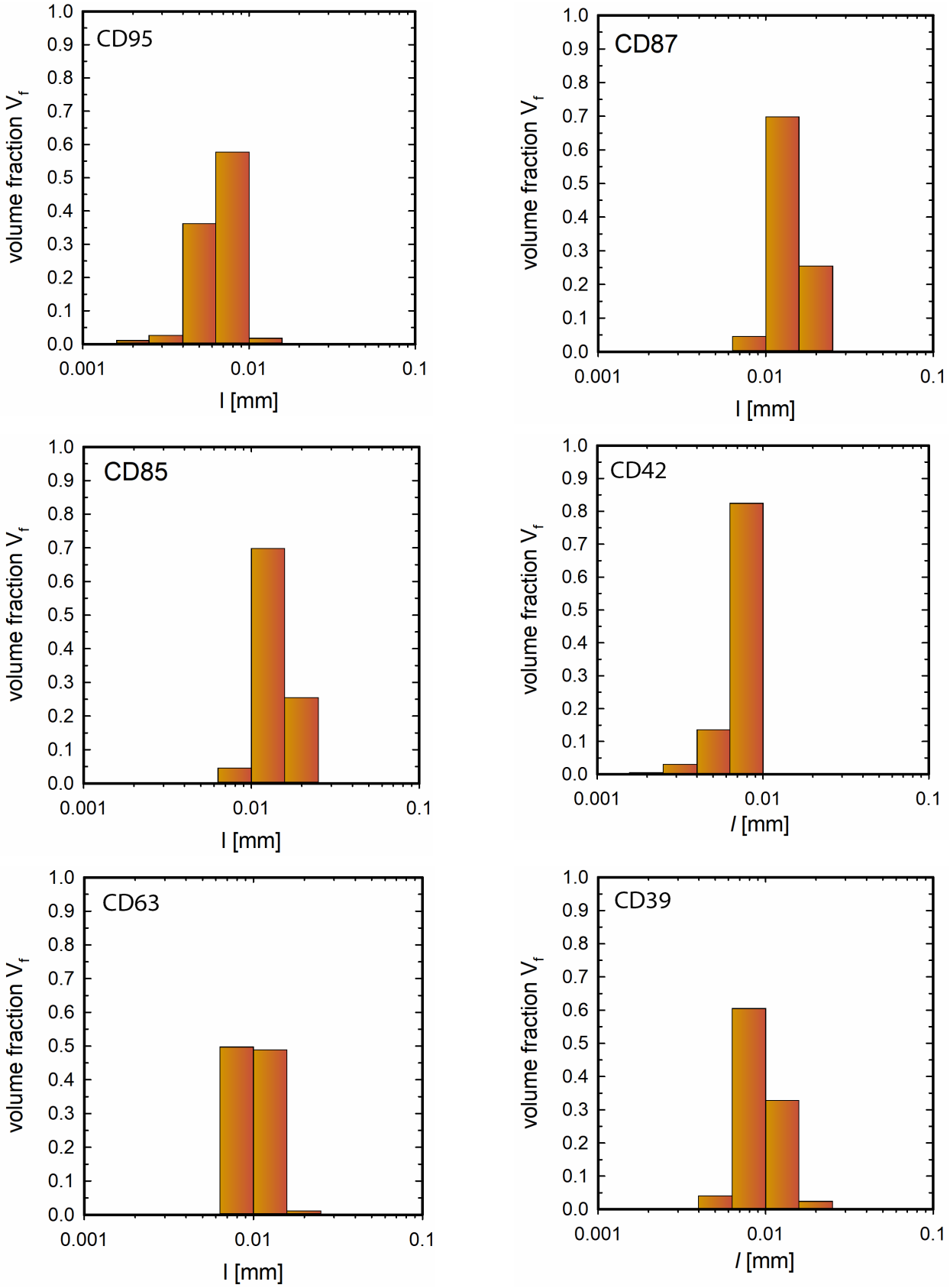
CD95
CD87
CD85
CD42
CD63
CD39
volume fraction V_f
l [mm]
/ [mm]
0.0
0.1
0.2
0.3
0.4
0.5
0.6
0.7
0.8
0.9
1.0
0.001
0.01
0.1

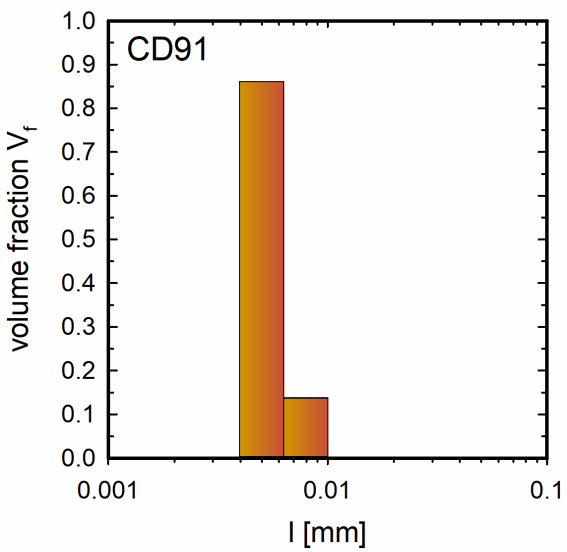
CD91
volume fraction V_f
1.0
0.9
0.8
0.7
0.6
0.5
0.4
0.3
0.2
0.1
0.0
0.001
0.01
0.1
l [mm]

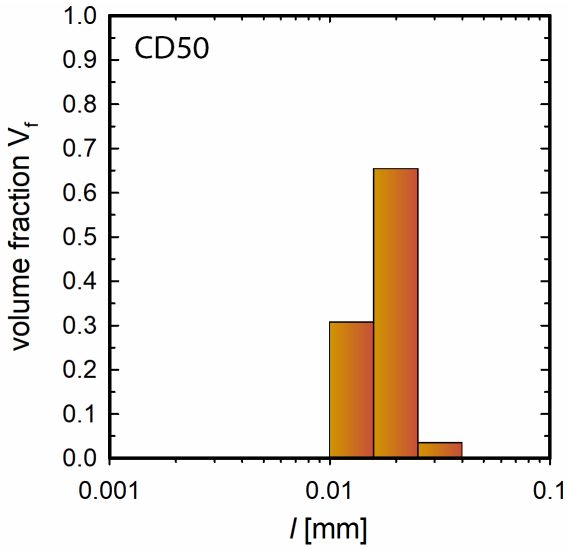
CD50
volume fraction V_f
1.0
0.9
0.8
0.7
0.6
0.5
0.4
0.3
0.2
0.1
0.0
0.001
0.01
0.1
l [mm]

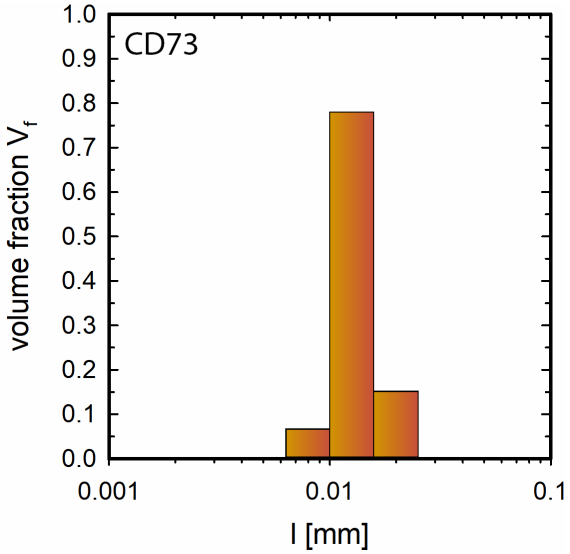
CD73
volume fraction V_f
1.0
0.9
0.8
0.7
0.6
0.5
0.4
0.3
0.2
0.1
0.0
0.001
0.01
0.1
l [mm]

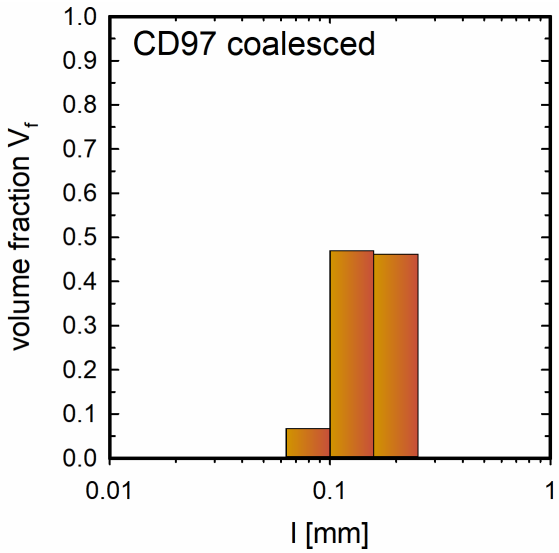
CD97 coalesced
volume fraction V_f
1.0
0.9
0.8
0.7
0.6
0.5
0.4
0.3
0.2
0.1
0.0
0.01
0.1
1
l [mm]

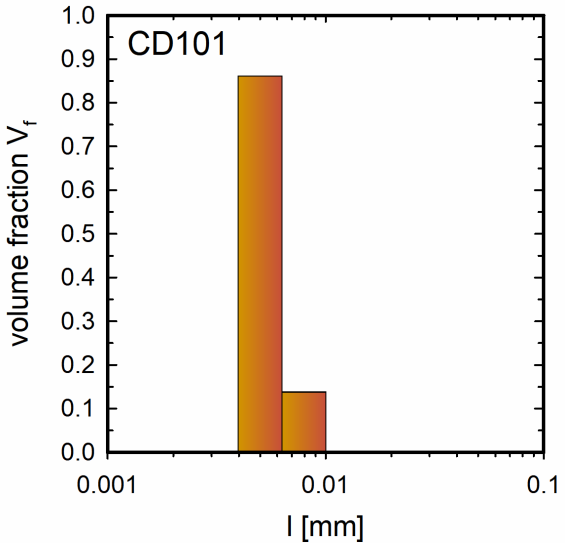
CD101
volume fraction V_f
1.0
0.9
0.8
0.7
0.6
0.5
0.4
0.3
0.2
0.1
0.0
0.001
0.01
0.1
l [mm]

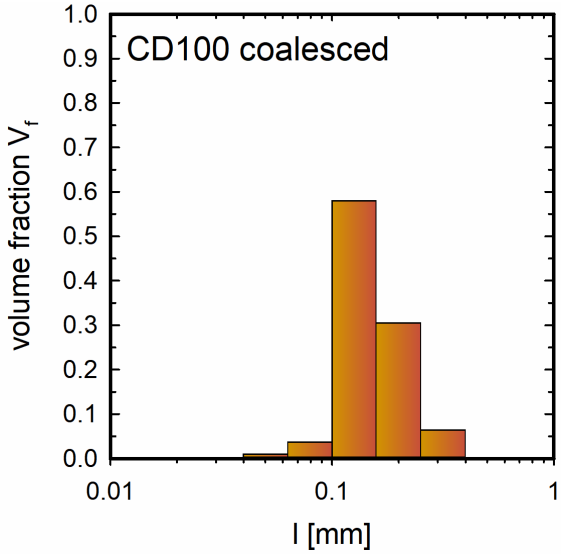
CD100 coalesced
volume fraction V_f
1.0
0.9
0.8
0.7
0.6
0.5
0.4
0.3
0.2
0.1
0.0
0.01
0.1
1
l [mm]

D-series

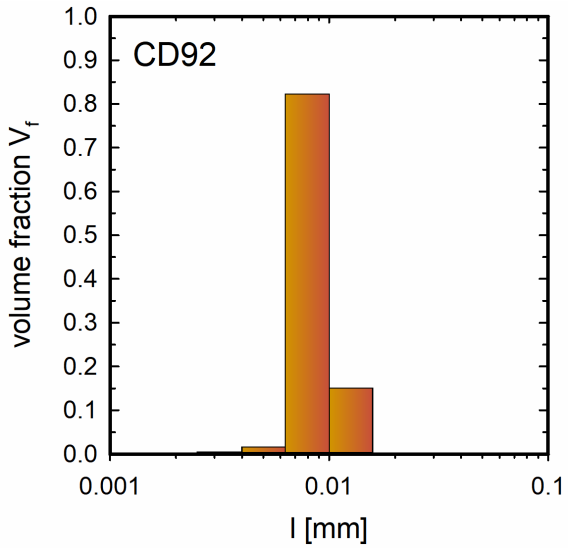
CD92
volume fraction V_f
1.0
0.9
0.8
0.7
0.6
0.5
0.4
0.3
0.2
0.1
0.0
0.001
0.01
0.1
l [mm]

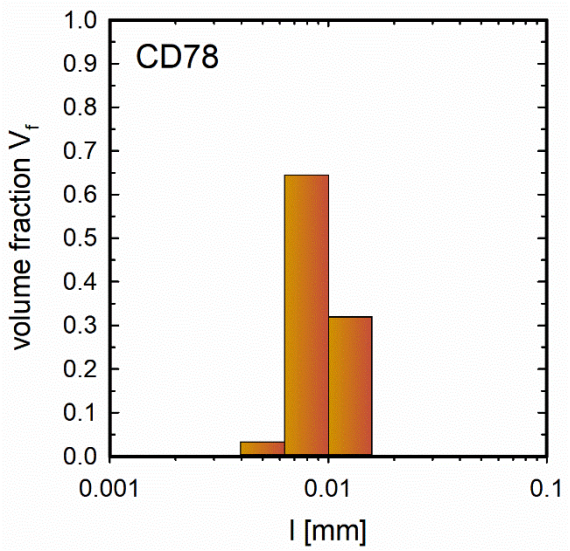
CD78
volume fraction V_f
1.0
0.9
0.8
0.7
0.6
0.5
0.4
0.3
0.2
0.1
0.0
0.001
0.01
0.1
l [mm]

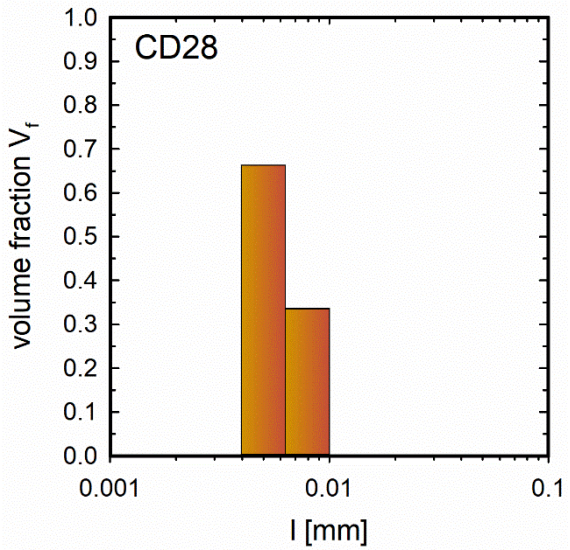
CD28
volume fraction V_f
1.0
0.9
0.8
0.7
0.6
0.5
0.4
0.3
0.2
0.1
0.0
0.001
0.01
0.1
l [mm]

TD-series

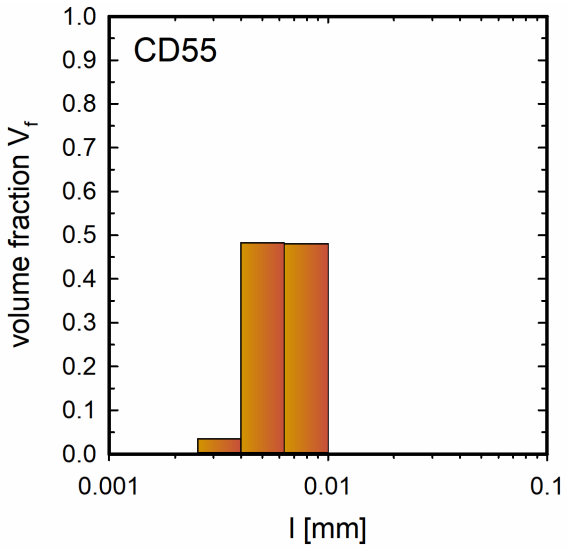

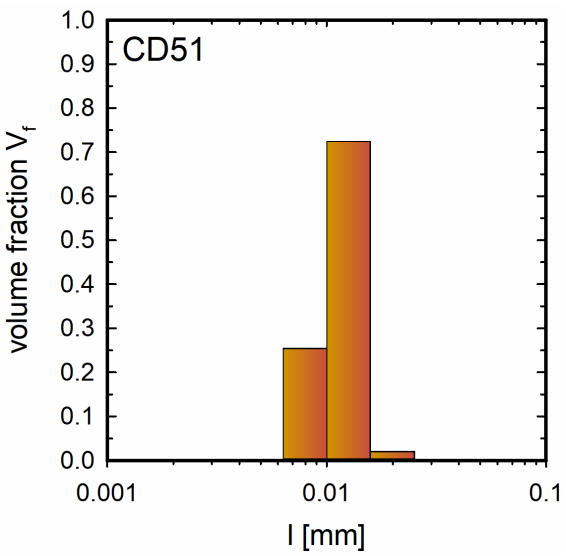

T-series

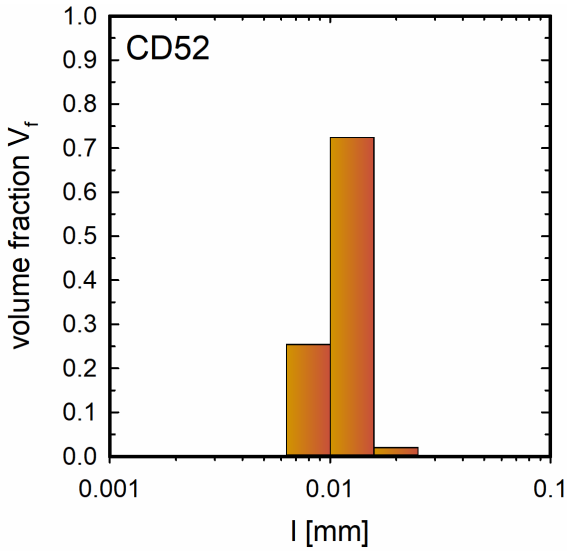

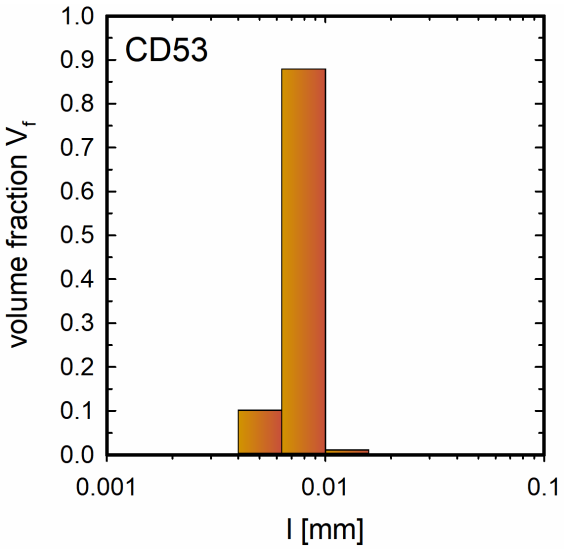

8.2 Sample images

In the following, images of those vesiculated samples of the C-series are shown, of which excerpts are compiled in Fig. II.3. The images were taken using a reflected light microscope and show the sample halves mounted in epoxy and polished for SEM-BSE analysis. All samples are still surrounded by the capsule material (Au80Pd20) and the images reflect the sample orientation during the experiments. The order of the images follows the order in Table II.2.

For scale: the inner capsule diameter of each sample is 5 mm.

CD94

c_{H2Oini} = 3.43 wt%

T_d = 1323 K

dP/dt = 0.17 MPa·s^{-1}

P_{final} = 40 MPa

CD95

c_{H2Oini} = 3.36 wt%
T_d = 1323 K
dP/dt = 0.17 MPa·s^{-1}
P_{final} = 20 MPa

CD87

c_{H2Oini} = 4.31 wt%
T_d = 1323 K
dP/dt = 0.17 MPa·s^{-1}
P_{final} = 60 MPa

CD85

c_{H2Oini} = 4.30 wt%

T_d = 1323 K

dP/dt = 0.17 MPa·s^{-1}

P_{final} = 40 MPa

CD40

c_{H2Oini} = 5.17 wt%
T_d = 1323 K
dP/dt = 0.17 MPa·s^{-1}
P_{final} = 100 MPa

CD42

c_{H2Oini} = 5.20 wt%
T_d = 1323 K
dP/dt = 0.17 MPa·s^{-1}
P_{final} = 90 MPa

CD63

c_{H2Oini} = 5.30 wt%

T_d = 1323 K

dP/dt = 0.17 MPa·s^{-1}

P_{final} = 80 MPa

CD50

c_{H2Oini} = 5.30 wt%
T_d = 1323 K
dP/dt = 0.17 MPa·s^{-1}
P_{final} = 70 MPa

CD73

c_{H2Oini} = 5.46 wt%
T_d = 1323 K
dP/dt = 0.17 MPa·s^{-1}
P_{final} = 60 MPa

CD102

c_{H2Oini} = 6.24 wt%

T_d = 1323 K

dP/dt = 0.17 MPa·s^{-1}

P_{final} = 150 MPa

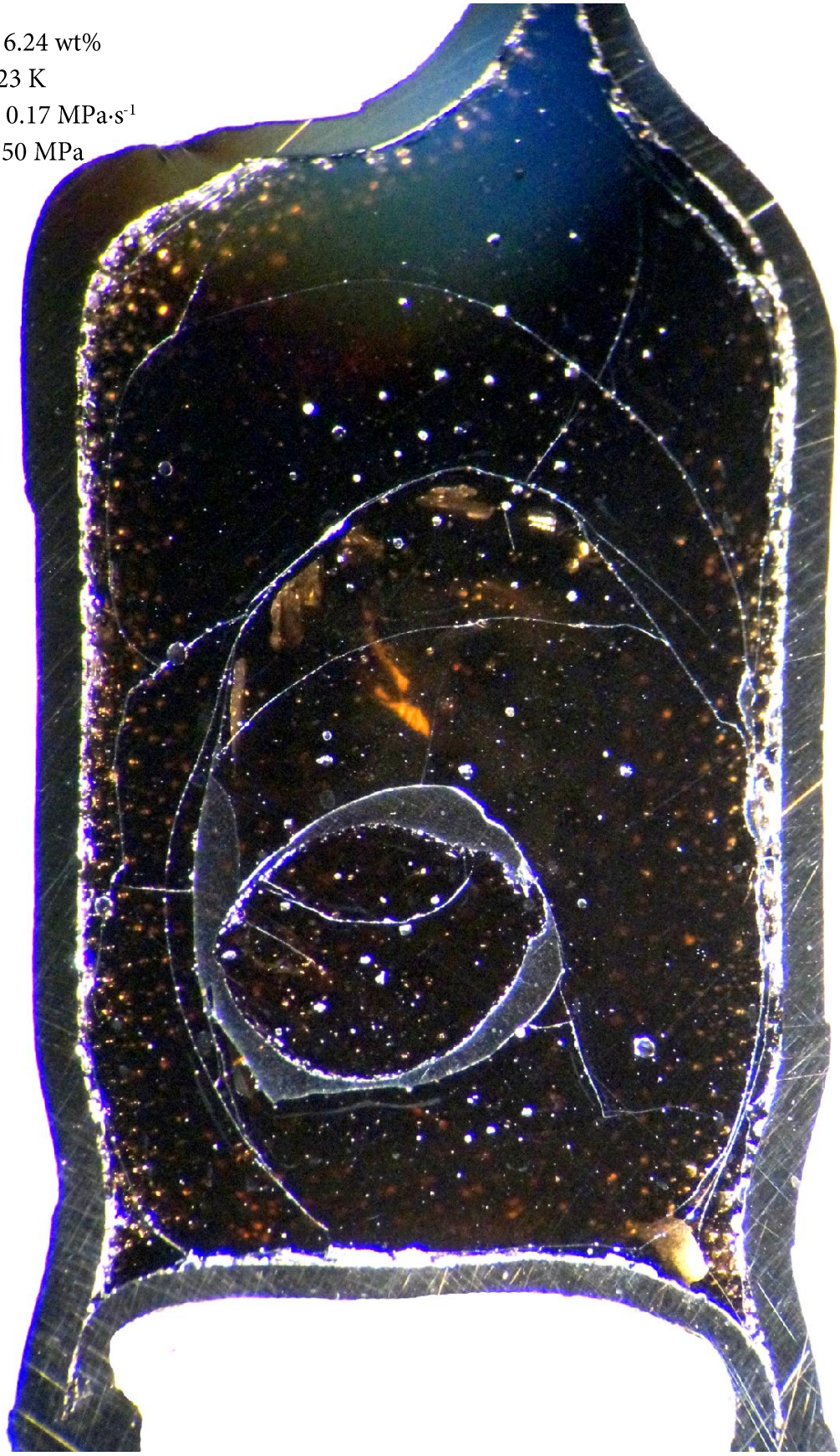

CD101

c_{H2Oini} = 6.28 wt%

T_d = 1323 K

dP/dt = 0.17 MPa·s^{-1}

P_{final} = 145 MPa

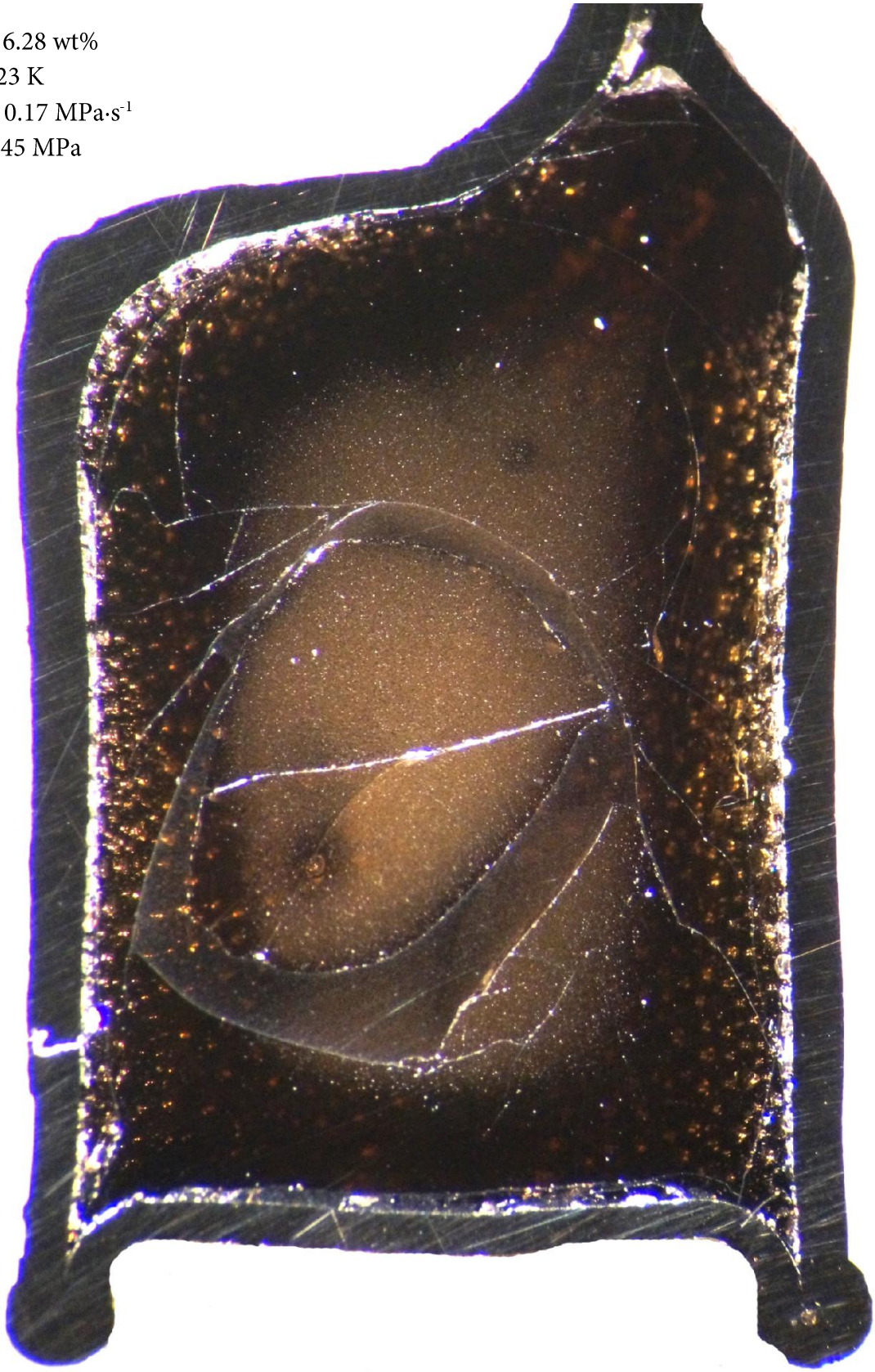

CD97

c_{H2Oini} = 6.30 wt%

T_d = 1323 K

dP/dt = 0.17 MPa·s^{-1}

P_{final} = 120 MPa

CD98

c_{H2Oini} = 5.96 wt%
T_d = 1323 K
dP/dt = 0.17 MPa·s^{-1}
P_{final} = 140 MPa

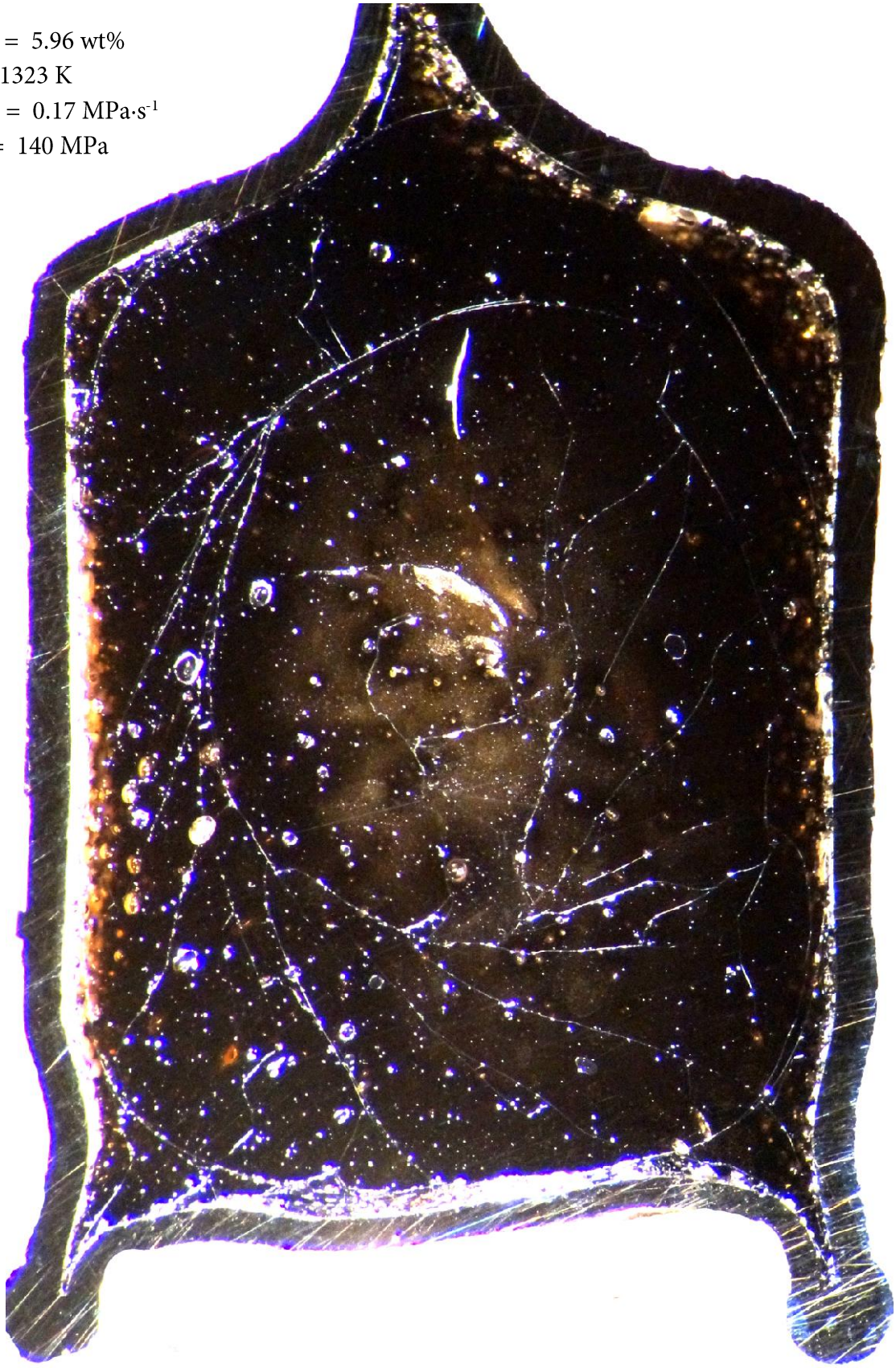

CD100

c_{H2Oini} = 5.77 wt%

T_d = 1323 K

dP/dt = 0.17 MPa·s^{-1}

P_{final} = 100 MPa

III. Vesicle shrinkage in hydrous phonolitic melt during cooling

A. Allabar, K.J. Dobson, C.C. Bauer, M. Nowak

Abstract

The ascent of hydrous magma prior to volcanic eruptions is largely driven by the formation of H_2O vesicles and their subsequent growth upon further decompression. Porosity controls buoyancy as well as vesicle coalescence and percolation, and is important when identifying the differences between equilibrium or disequilibrium degassing from textural analysis of eruptive products. Decompression experiments are routinely used to simulate magma ascent. Samples exposed to high temperature (T) and pressure (P) are decompressed and rapidly cooled to ambient T for analysis. During cooling, fluid vesicles may shrink due to decrease of the molar volume of H_2O and by resorption of H_2O back into the melt driven by solubility increase with decreasing T at P < 300 MPa. Here, we quantify the extent to which vesicles shrink during cooling, using a series of decompression experiments with hydrous phonolitic melt (5.3–3.3 wt% H_2O, T between 1323 and 1373 K, decompressed from 200 to 110–20 MPa). Most samples degassed at near-equilibrium conditions during decompression. However, the porosities of quenched samples are significantly lower than expected equilibrium porosities prior to cooling. At a cooling rate of 44 $K \cdot s^{-1}$, the fictive temperature T_f, where vesicle shrinkage stops, is up to 200 K above the glass transition temperature (T_g), Furthermore, decreasing cooling rate enhances vesicles shrinkage. We assess the implications of these findings on previous experimental degassing studies using phonolitic melt, and highlight the importance of correctly interpreting experimental porosity data, before any comparison to natural volcanic ejecta can be attempted.

1. Introduction

Volcanic eruptions are driven by magma density decrease caused by the exsolution of volatiles, mainly H_2O (e.g., Gonnermann and Manga 2007). H_2O supersaturation of the melt can be induced by a pressure (P) decrease and causes formation of vesicles, which then grow by both pressure related equation of state (EOS) expansion and continuous diffusion of H_2O from the melt into the fluid phase (e.g., Sparks 1978). The porosity of a magma is a key parameter influencing the buoyancy and thus driving the acceleration of magma during ascent.

In experimental studies, the porosity of decompressed silicate melts subsequently quenched to glass has been used to investigate vesicle growth and coalescence as well as the evolution of permeability or percolation (Giachetti et al. 2019; Lindoo et al. 2016). Porosity has also been used to distinguish between equilibrium or disequilibrium degassing by comparing the glass porosity (Φ_{glass}) or the residual H_2O concentration in the glass ($c_{H2Oglass}$)

with those at experimental equilibrium conditions (e.g., Gardner 2012; Larsen and Gardner 2004; Mangan and Sisson 2000; Iacono-Marziano et al. 2007).

However, vesicles may shrink during cooling through a decrease in molar volume of H_2O fluid (V_{mH2O}) within the vesicles (EOS shrinkage; Marxer et al. 2015), and because of the increasing isobaric solubility of H_2O in silicate melt with decreasing T at P < 300 MPa (Holtz et al. 1995; Schmidt and Behrens 2008), leading to resorption of H_2O from the fluid vesicles back into the melt (McIntosh et al. 2014; Ryan et al. 2015). Together, these processes lead to a reduction in porosity, and increase the H_2O concentration (c_{H2O}) of the melt during cooling before the supercooled melt is quenched to a glass. Measured Φ_{glass} and $c_{H2Oglass}$ therefore may not represent the molten state of the sample prior to cooling, especially when cooling rates are low. Slow cooling (~10 $K \cdot min^{-1}$) in sintering experiments using rhyolitic glass powder (T of 1023–823 K, P of 22 MPa and H_2O concentrations up to ~2.2 wt%) in the presence of fluid leads to resorption of H_2O vesicles resulting in fully dense obsidian (Gardner et al. 2019).

Cooling rates in decompression experiments are usually much faster (up to 150 $K \cdot s^{-1}$), but T and c_{H2O} are significantly higher and melt viscosities are lower compared to the sintering experiments of Gardner et al. (2019). Consequently, vesicle shrinkage is still expected during cooling of vesiculated melts (McIntosh et al. 2014; Marxer et al. 2015; Allabar and Nowak 2018). McIntosh et al. (2014) have found that during fast cooling of experimentally decompressed phonolitic melt to ambient T within 3–10 s significant resorption occurs, demonstrating that the state prior to quench cannot be frozen in. Therefore, we further investigate this effect and quantify vesicle shrinkage and H_2O resorption during cooling on an existing data set of vesiculated phonolitic melt with white pumice composition of the AD79 Vesuvius eruption (VAD79; Iacono-Marziano et al. 2007) quenched to glass. By applying different cooling rates (q) on these vesiculated phonolitic melts by additional experiments, we determine the influence of q on the extent of vesicle shrinkage.

Calculations were performed to quantify the effect of shrinkage during cooling, driven by the EOS of the H_2O fluid and resorption of H_2O back into the melt. To determine the fictive temperature (T_f) where vesicle shrinkage stops, Φ_{glass} was used as well as the liquid water to vesicle volume ratio at ambient conditions derived from X-ray computed tomography (XCT) data. Finally, the results of this study are compared to previous decompression experiments with hydrous phonolitic melt and discussed with respect to the possible effect of vesicle shrinkage. Variables used in this publication are listed in Table III.1.

Table III.1 Symbol definitions

Symbol	Definition	Unit
B_s	vesicle shrinkage factor	
c_{H2O}	H_2O concentration	wt%
c_{H2Oequ}	equilibrium H_2O concentration	wt%
$c_{H2Oglass}$	H_2O concentration in glass after quench	wt%
c_{H2Oini}	initial H_2O concentration in the melt prior to decompression	wt%
c_{H2OIR}	H_2O concentration measured with FTIR close to vesicles	wt%
c_{H2Ores}	maximum possible resorbed c_{H2O} assuming resorption to T_g	wt%
c_{H2Ores_Tf}	residual c_{H2O} at T_f	wt%
D_{H2O}	diffusivity of H_2O in silicate melt	$mm^2 \cdot s^{-1}$
dP/dt	decompression rate	$MPa \cdot s^{-1}$
l	characteristic diffusion length	mm
P	pressure	MPa
P_{final}	final pressure where samples were quenched	MPa
q	quench rate; NQ = 16 $K \cdot s^{-1}$; MQ = 44 $K \cdot s^{-1}$	$K \cdot s^{-1}$
r	radius	m
T	temperature	K
T_d	run temperature of decompression experiment	K
T_f	fictive temperature where vesicle shrinkage effectively stops	K
T_g	glass transition temperature	K
T_{g_eq}	glass transition temperature for melt with equilibrium c_{H2O}	K
T_{g_res}	glass transition T for melt with maximum resorbed c_{H2O}	K
V_{H2Ol}	volume of liquid H_2O in vesicles at room T	voxel
V_{mH2O}	molar Volume of H_2O	$cm^3 \cdot mol^{-1}$
VND	vesicle number density normalized to vesicle free sample volume	mm^{-3}
V_{ves}	vesicle volume in the glass	voxel
ΔP_{PS}	difference between saturation P and P of phase separation	MPa
η	melt viscosity	Pa·s
$\eta_{\_Tf}$	viscosity at T_f, where vesicle shrinkage stops	Pa·s
ρ_{melt}	melt density	$g \cdot cm^{-3}$
σ	surface tension	$N \cdot m^{-1}$
τ_d	decompression timescale	s
τ_{diff}	diffusion timescale	s
Φ_{EOS}	calculated porosity when shrinkage works until T_{g_eq}	%
Φ_{equ}	equilibrium porosity	%
Φ_{glass}	glass porosity	%
Φ_{RES}	calculated porosity when shrinkage works until T_{g_res}	%

2. Experimental and analytical methods

2.1 Decompression experiments

We augment a series of decompression experiments from Allabar and Nowak (2018) and Allabar et al. (2020a) (Table III.2) to quantify vesicle shrinkage during cooling of vesiculated VAD79 phonolitic melts. The experiments of these studies were conducted in an internally heated argon pressure vessel (IHPV) at decompression temperatures (T_d) of 1323–1373 K and initial dissolved H_2O contents (c_{H2Oini}) of 5.3, 4.3, and 3.3 wt%. Decompression rates were 0.064–1.7 MPa·s^{-1}, starting from initial P of 200 MPa to final P (P_{final}) ranging between 110–20 MPa. At P_{final}, samples were cooled with a medium quench rate (MQ, although reported as RQ in Allabar and Nowak 2018). Samples were quenched by melting a platinum wire, at which the sample capsules were fixed during the experiments, leading to a capsule drop into the cold zone of the samples holder (Berndt et al. 2002) that was equipped with a brass rod at the bottom to reduce cooling rate (see "quantification of cooling rate"). This procedure was necessary to obtain intact samples for analysis.

The experiments of this study were performed on the same starting material and at identical run temperature as in Allabar and Nowak (2018) and Allabar et al. (2020a), with c_{H2Oini} of 5.3 wt% and a decompression rate of 0.17 MPa·s^{-1}. However, different quench protocols were applied, to investigate the influence on the Φ_{glass} of the finally analyzed glassy samples. Synthetic VAD79 glass cylinders with 5 mm diameter and 6.5 mm length were inserted together with 5.3 wt% H_2O into Au80Pd20 tubes (13 mm length, 5 mm inner diameter) that were welded shut with a lid at the bottom. After sample filling, the upper ends of the capsules were crimped to a three sided star and welded. Possible leakage was checked by storing the capsules in a compartment dryer at 383 K, pressurizing to 100 MPa at ambient T, and again storing at 383 K. The capsules were re-weighed after each step. Constant capsule weight ruled out leakage and qualified the capsules for the experiments.

The samples were hydrated in the IHPV at slightly H_2O undersaturated conditions at 200 MPa and superliquidus T of 1523 K for at least 94 h to obtain a homogeneous hydrous melt. After hydration, T was decreased to the decompression temperature T_d of 1323 K, still above the liquidus (Iacono-Marziano et al. 2007; Marxer et al. 2015; Allabar et al. 2020a). The thermal gradient, measured by two thermocouples close to the samples over a distance of ~12 mm, is < 20 K. The T gradient within the samples is assumed to be < 10 K because the

sample length of 6.5 mm is lower than the distance between the two thermocouples. The samples were equilibrated at T_d for at least 0.5 h before decompression was initiated. For the first pair of experiments, samples were decompressed from 200 MPa to P_{final} of 80 MPa and quenched by switching off the furnace, while the samples remained in the hot zone of the sample holder (normal quench = NQ). The sample CD49 underwent a non-isobaric NQ, with a monitored P drop of ~5–7 MPa during cooling of the argon pressure medium (NQ non-isobaric), while sample CD66 underwent an isobaric NQ (± 0.1 MPa), with P being kept constant by pumping additional argon into the vessel. Sample CD74 (a replicate of CD50; Allabar et al. 2020a), was decompressed to 70 MPa and quenched with MQ. An additional pair of experiments, samples CD37 and CD41, were decompressed to 80 and 90 MPa, respectively, then cooled with an unknown rate that must have been either non-isobaric NQ or MQ, because of a missing T decrease that would have indicated the capsule drop from the hot zone into the cool part of the sample holder. After re-weighing to exclude capsule leakage, the quenched samples, except of CD74, were cut along their cylinder axis. One half of each sample was prepared for SEM image analysis and the other halves were prepared to obtain double-sided polished thin sections with 89–210 μm thickness for Fourier Transform Infrared (FTIR) and transmitted light microscopy analysis. Thin section thickness was measured with a Mitutoyo digital micrometer (± 3 μm). Sample CD74 was unwrapped from the capsule material and scanned using XCT.

2.2 Quantification of cooling rate

For the IHPV with rapid quench setup, a cooling rate (q) of ~150 $K \cdot s^{-1}$ (RQ) was determined by Berndt et al. (2002) for dropping the capsule from the hot zone of the furnace into the cold part of the samples holder. The temperature at the bottom of the sample holder is 293–298 K at experimental T of up to 1523 K and 200 MPa (Berndt et al. 2002). However, for experiments from Allabar and Nowak (2018) and Allabar et al. (2020a) the aim was to reduce tension crack formation in the samples during quench. Otherwise, samples will likely disintergrate and pieces may be lost during preparation. Thus, the experimental setup of the IHPV sample holder was modified by inserting a 35 mm brass cylinder at the bottom of the sample holder. This setup enables a medium quench rate (MQ) because the capsule stays slightly closer to the hot zone of the furnace during cooling, i.e., at T >298 K. In order to quantify the quench rate of this setup, reference experiments where performed on two glass

cylinders of the same geometry as for decompression experiment samples (5 mm diameter, 6.5 mm length) using haplogranite composition (AOQ = $Ab_{38}Or_{34}Qz_{28}$, Holtz et al. 1995; Nowak and Behrens 1995). The AOQ melts were hydrated with ~5.3 wt% H_2O in Au80Pd20 capsules at 200 MPa and 1523 K for 96 h. After hydration, one sample experienced the isobaric MQ protocol, while the other underwent an isobaric NQ. Doubly polished thin sections were prepared from the quenched glasses and the molecular H_2O and OH group absorption band intensities determined with FTIR (A_{5230} and A_{4520}, respectively). 20 and 23 measurements were performed on the NQ and RQ sample, respectively, with a spectral resolution of 4 cm^{-1} and 50 scans per measurement. A linear baseline subtraction (Behrens et al. 1996) and normalization to 1 mm sample thickness was applied. Cooling rates were then determined using the hydrous species geospeedometer (Zhang et al. 2000). For the MQ protocol, mean $A_{5230} = 0.793 \pm 0.08$ and $A_{4520} = 0.343 \pm 0.003$ yield a cooling rate of 44 ± 11 K·s^{-1}. For the NQ protocol, mean $A_{5230} = 0.769 \pm 0.002$ and $A_{4520} = 0.330 \pm 0.002$ give a cooling rate of 16 ± 3 K·s^{-1}. This NQ cooling rate is consistent with the logged T close to the sample during cooling, which showed nearly linear cooling from T_d down to ~573 K. The glass transition temperature (T_g) of this AOQ glass (at 5.3 wt% and a cooling rate of 16 K·s^{-1}) is at 660 K (Dingwell and Webb 1990; Giordano et al. 2008). Thus, linear cooling down to T_g can be assumed. The near sample T logs during NQ at P between 200 and 50 MPa show that the cooling rate is nearly independent of P in this range.

2.3 Determination of vesicle number density and glass porosity

Vesicle number density (*VND*) and Φ_{glass} were determined merely on the vesiculated central sample volume because this volume is of interest to study vesiculation driven by homogeneous phase separation. Heterogeneously nucleated fringe vesicles at the capsule wall and the drainage zone that is formed by diffusional loss of H_2O into fringe vesicles are experimental artifacts (e.g., Mangan and Sisson 2000; Iacono-Marziano et al. 2007; Preuss et al. 2016; Allabar and Nowak 2018; Allabar et al. 2020a) and were therefore omitted for analysis.

Sample CD66 was analyzed with transmitted light microscopy on the thin section of the sample. Vesicles were counted during focusing through the sample and Φ_{glass} was determined using measured vesicles sizes. The *VND*s in the other samples of this study were determined by analysis of the backscattered electron (BSE) images, because vesicles are large

enough for a sufficiently high intersection probability. The BSE images were analyzed using ImageJ and the stereological 2–3D conversion using CSDCorrections (Higgins 2000). The *VND* was normalized to vesicle free glass volume. An error in *VND* of ± 0.13 log units was estimated with an error propagation considering all steps that are prone to errors (Allabar et al. 2020a). Errors of Φ_{glass} were provided by CSDCorrections in case of BSE image analysis. For transmitted light microscopy analysis, an error in Φ_{glass} was estimated with an error propagation calculation, using the error in sample thickness of ± 3 µm and assuming an error of 10% for vesicle size measurement and 5% for the vesicle count. A more detailed description of *VND* and Φ_{glass} analysis is given in Marxer et al. (2015) and Allabar et al. (2020a).

2.4 FTIR-micro-spectroscopy

Near-infrared measurements in transmission mode were carried out with a Hyperion 3000 IR-microscope connected to a Bruker Vertex v80 FTIR, using a CaF_2 beam splitter and an InSb single element detector together with a 15× Cassegrain objective. Samples of Allabar et al. (2020a) and samples of this study were measured to determine the residual c_{H2O} in the glass between vesicles (c_{H2OIR}). Measurements were located between vesicles in the central sample volume or as close as possible to the vesicles at the margin of the central vesiculated volume (Fig. III.1). The knife-edge aperture was adjusted for each measurement individually between 10 × 10 to 30 × 30 µm to ensure that the beam path was free of vesicles. This was checked by focusing through the entire sample volume in *z* direction at the measurement location. 50 scans were recorded per spectrum with a spectral resolution of 4 cm^{-1} using air as reference. At least five spots per sample were measured. For the determination of c_{H2OIR} from molecular H_2O (A_{5210}) and hydroxyl group absorbance (A_{4470}) the c_{H2O}-density relationship (ρ[g·cm^{-3}] = 2.47-0.013·c_{H2O}[wt%]) and linear molar extinction coefficients (ε_{H2O} = 1.18 and ε_{OH} = 1.14 l·mol^{-1}·cm^{-1}) from Iacono-Marziano et al. (2007) were used.

To resolve c_{H2O} gradients with high spatial resolution between vesicles in the central vesiculated part of the sample CD73, mid-infrared measurements were performed using an attenuated total reflectance (ATR) objective (20×) mounted on the Hyperion3000 microscope in combination with a 64 × 64 focal plane array detector (FPA). The ATR germanium (Ge) crystal was brought in contact with the polished sample surface using a contact pressure of 3 (within a possible range of 1–5; ~4.4 N). At higher contact pressures the vesiculated glasses tend to break. A value of 3 is low enough to prevent cracking and is

sufficient for reproducible peak heights of the fundamental OH stretching band at 3450 cm^{-1}. An Au-mirror was used as reference, spectral resolution was decreased to 16 cm^{-1} to minimize the noise associated with atmospheric water vapor (Lowenstern and Pitcher 2013) and 256 scans were accumulated for each spectrum. With these settings, 128 × 128 spectra were collected in 4 frames that cover a sample area of 70 × 70 µm. For each spectrum the peak height of the fundamental OH stretching band at 3450 cm^{-1} was determined after linear baseline subtraction anchored at 3760 and 2430 cm^{-1}. Calibration for absolute c_{H2O} for this method was not performed because the contact pressure, i.e., the energy of the light reaching the detector across the area of a frame, was not homogeneous. This is probably due to a tiny tilt of the Ge-ATR-crystal relative to the sample surface.

2.5 Raman micro-spectroscopy

Raman micro-spectroscopy (RMS) mapping was performed on sample CD73 at the same location as the FTIR mapping to quantify $c_{H2Oglass}$ gradients. A Renishaw InVia confocal Raman micro-spectrometer was used, equipped with a 532 nm ("green") laser, a 1800 grooves·mm^{-1} grating, and a Peltier-cooled CCD-detector. Laser power was set to 10%, corresponding to ~2.5 mW on the sample, which is low enough to avoid oxidation or dehydration of the samples (Di Genova et al. 2017a). A 50× objective with a numerical aperture of 0.75 was used together with the high confocality setting to optimize for spatial resolution. The laser was focused at the sample surface, and it was checked whether the laser remained focused while moving across the mapped area. An area of 38 × 52 µm was mapped with one spectrum collected each µm (= 1976 spectra) from 100–4000 cm^{-1} with an acquisition time of 10 s. Laser intensity was checked before and after the mapping to confirm its stability. To obtain total H_2O concentration from the Raman spectra, a calibration was performed with hydrated reference samples from Marxer et al. (2015) (REF02–06 and one unpublished sample) with known c_{H2O} (1.37–5.60 wt%) from FTIR spectroscopy. Two calibrations were used (e.g., Schiavi et al. 2018): (1) calibration of the high wavenumber 3450 cm^{-1} band (HW) and (2) calibration of the ratio of the HW band and the low wavenumber (LW, 200–1250 cm^{-1}) aluminosilicate bands. A detailed description of calibration is given in the supplement "RMS and FTIR supplementary information".

2.6 XCT-measurements

The MQ sample (CD74) was scanned using a Zeiss Xradia 410 laboratory scanner system operating at 130 kV, a current of 76 µA, and the Xradia HE3 filter to reduce beam hardening effects. 2001 projections were collected with an exposure time of 10 s and the data were reconstructed using the Xradia proprietary algorithm to give a data volume with voxels of 2.06 µm edge length. The image data were segmented and visualized using AVIZO© (ThermoFisher). After first defining a sample mask (manual refinement of a magic wand segmentation interpolated between every 100th slice to ensure capture of all edge contacting vesicles with thin films), the image data were segmented into glass and vesicle using the magic wand tool built into the Avizo segmentation workroom. Image noise and the smallest vesicle population were then removed by opening (kernel = 3) and closing (kernel = 3) and a 2D (perpendicular to sample axis) fill operation. Segmentation of the vesicle–gas and vesicle–liquid phases is challenging because of the small difference in greyscale value, and the low signal-noise ratio in the raw data. However, after applying a 3D non-local means filter (5, 0.2, 10.3) to the vesicles, segmentation could be achieved manually with a single click per vesicle. For comparison, two vesicles were segmented by manual assignment to the liquid and gas phase, before the volume of the different phases were calculated.

3. Results and discussion

In the samples of this study, we observed heterogeneously nucleated fringe vesicles attached to the capsule walls, a vesicle free drainage zone, and a finely vesiculated central volume formed by homogeneous phase separation as reported elsewhere (e.g., Iacono-Marziano et al. 2007; Allabar and Nowak 2018; Allabar et al. 2020a). The log*VND* (in mm^{-3}) in the central sample volume ranges between 4.70 and 5.22 (analytical error ± 0.13 log units; Allabar et al. 2020), which is consistent with the log*VND* observed in other samples with a c_{H2Oini} of ~5.3 wt% (Table III.2). Sample capsules after decompression and quench are often deformed with concave capsule walls. Furthermore, the fringe vesicles in all samples including those of Allabar et al. (2020a) are strongly deformed with melt flow textures in their vicinity sometimes marked by small vesicles (Fig. III.1a). The homogeneously distributed small vesicles in the sample center are spherical, except of few vesicle pairs where the inter vesicle wall is dimpled or a neck is formed from one vesicle to the other (Fig. III.1b). Castro

et al. (2012) explain such textures with the onset of coalescence, while McIntosh et al. (2014) attribute this to vesicle shrinkage during cooling.

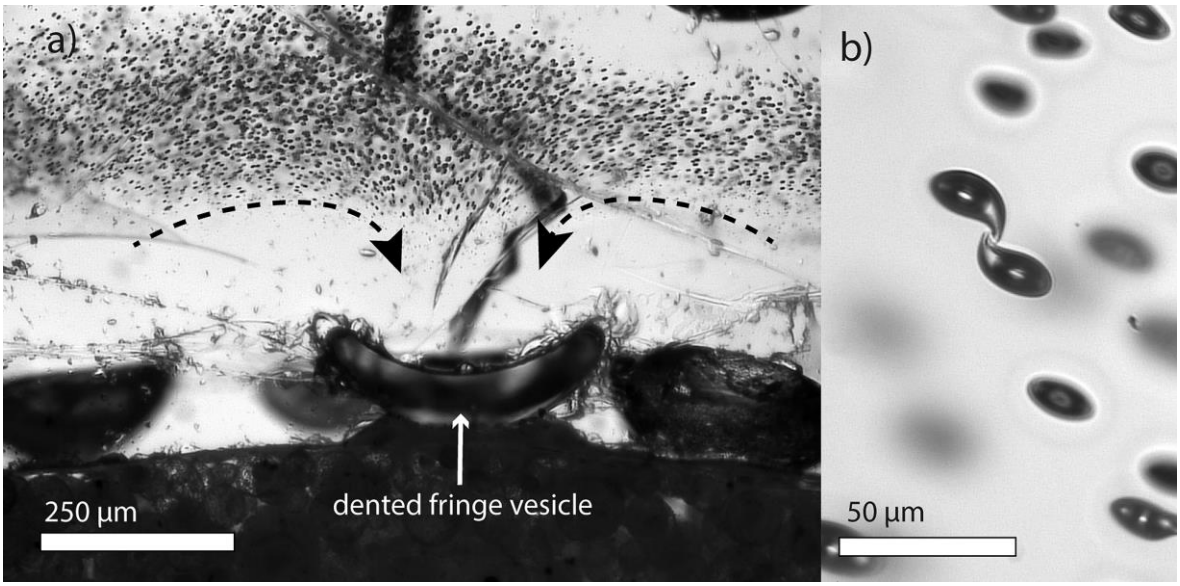

Fig. III.1 a) Transmitted light microscopy image of sample bottom of CD50 (Allabar and Nowak 2018). The fringe vesicles are dented and flow textures in the zone with small vesicles are visible. Large vesicles are surrounded by a vesicle free drainage zone. b) Transmitted light microscopy image of vesicles within the central part of CD49. Vesicles positioned close to each other are often deformed and form a neck towards each other. Detailed capsule images are shown in the supplement "Sample images" of study II.

Marxer et al. (2015) have also reported collapsed capsules with concave deformed walls after the decompression experiments (Figs. 6 and 15b, therein) and attribute this to vesicle shrinkage during cooling. Cooling causes a P drop within the capsule relative to quench pressure that drives capsule collapse during cooling. In contrast to this observation, an experimental setup capable to record the complete volume increase during decompression-induced degassing should freeze melt porosity (Φ_{melt}) at P_{final} during cooling. Consequently, capsules should show a convex shape. A concave deformation, however, as observed by Marxer et al. (2015) and in the experiments summarized in this study, can only be explained by a volume reduction of the capsule interior, i.e., shrinkage of H_2O vesicles, during cooling. Thus, we suggest that the textures observed at ambient conditions record vesicle shrinkage during cooling. These textures include the collapse of large fringe vesicles and flow textures preserved in the finely vesiculated glass in their vicinity. Strongly deformed vesicles attached to the capsule wall would not be able to maintain a spherical shape if shrinkage were faster than the time required for the vesicle to adjust its geometry by reduction of surface energy. In the central sample volume, a low number of large vesicles (~200–300 µm diameter) that

Table III.2 Summary of experimental conditions, results and calculations. All decompression experiments were hydrated at 200 MPa prior to decompression. Symbol definitions are given in Table III.1

sample #	c_{H2Oini} [wt%]	T_d [K]	P_{final} [MPa]	dP/dt [MPa·s^{-1}]	q [K·s^{-1}]	logVND [mm^{-3}]	Φ_{glass} [%]
CD66	5.29 ± 0.11	1323	80	0.17	16 isob.	5.22	0.5 ± 0.2
CD49	5.28 ± 0.09	1323	80	0.17	16 non isob.	4.70	3.1 ± 0.3
CD41	5.29 ± 0.09	1323	90	0.17	(44)*	5.22	1.1 ± 0.2
CD37	5.32 ± 0.09	1323	80	0.17	(16 non isob.)*	5.17	1.9 ± 0.2
CD74 (XCT)	5.33 ± 0.11	1323	70	0.17	44	n.d.	n.d.
~5.3 wt%							
CD40	5.17 ± 0.09	1323	100	0.17	44	5.15	0.1 ± 0.1
CD42	5.20 ± 0.09	1323	90	0.17	44	4.98	1.1 ± 0.1
CD63	5.30 ± 0.10	1323	80	0.17	44	5.24	7.0 ± 0.7
CD39	4.97 ± 0.13	1323	80	0.17	44	5.17	4.5 ± 0.5
CD91	5.33 ± 0.10	1323	80	0.17	44	5.41	9.0 ± 1.1
CD83	5.46 ± 0.07	1323	80	0.17	44	5.78	3.2 ± 1.0
CD50	5.30 ± 0.09	1323	70	0.17	44	4.83	13.1 ± 1.4
CD73	5.46 ± 0.17	1323	60	0.17	44	5.41	18.5 ± 2.2
CD92	5.10 ± 0.09	1323	80	0.064	44	5.35	4.6 ± 0.6
CD78	5.12 ± 0.05	1323	82	1.7	44	5.32	3.3 ± 0.6
CD28	5.29 ± 0.06	1323	95	1.7	44	5.05	0.5 ± 0.1
CD59	5.21 ± 0.05	1373	110	1.7	44	5.48	0.1 ± 0.1
CD55	5.22 ± 0.05	1373	100	1.7	44	4.60	0.5 ± 0.1
CD57	5.32 ± 0.07	1373	100	1.7	44	4.78	0.1 ± 0.1
CD51	5.27 ± 0.11	1373	75	1.7	44	4.98	4.2 ± 0.9
CD52	5.21 ± 0.07	1373	90	0.17	44	4.96	1.6 ± 0.4
CD53	5.17 ± 0.06	1373	80	0.17	44	4.95	1.5 ± 0.2
~4.3 wt%							
CD87	4.31 ± 0.10	1323	60	0.17	44	5.51	5.4 ± 1.3
CD85	4.30 ± 0.13	1323	40	0.17	44	5.45	24.4 ± 2.2
~3.3 wt%							
CD94	3.43 ± 0.05	1323	40	0.17	44	5.96	0.3 ± 0.1
CD95	3.36 ± 0.12	1323	20	0.17	44	6.37	15.4 ± 2.1

* quench rate of these samples was unknown after the experiment, but a possible quench rate was derived from Φ_{glass} (for details see text). Therefore, Φ_{EOS} and Φ_{RES} were not calculated for these samples.

appear at low P_{final} (sample CD 73) preserve deformation (Allabar et al. 2020a) while the small vesicles (~15 µm diameter) within the central sample volume are nearly spherical. The relaxation of deformed vesicles to a spherical shape depends on the radius (Toramaru 1998):

$$t_{relax} = \frac{r \cdot \eta}{\sigma} \quad \text{(III.1)}$$

Table III.2 (continued)

c_{H2OIR} [wt%]	c_{H2Oequ} [wt%]	τ_{diff}/τ_d	Φ_{equ} [%]	Φ_{EOS} [%]	Φ_{RES} [%]	T_f [K]	c_{H2Ores_Tf} [wt%]	Reference
5.00 ± 0.11	3.12	$5.7 \cdot 10^{-3}$	26.9	8.7	0.0	683	5.23	
n.d.	3.12	$8.8 \cdot 10^{-3}$	26.9	8.7	0.0	767	4.74	
5.23 ± 0.05	3.34	$6.8 \cdot 10^{-3}$	22.7	-	-	753	5.11	
5.08 ± 0.06	3.12	$4.9 \cdot 10^{-3}$	27.2	-	-	725	4.97	
n.d.	2.88	n.d.	32.3	12.1	1.9	810ǂ	4.22	
n.d.	3.56	$1.9 \cdot 10^{-2}$	17.9	5.8	0.0	784	5.21	AN18
5.22 ± 0.06	3.34	$9.8 \cdot 10^{-3}$	21.9	7.3	0.0	768	5.03	AA20a
5.10 ± 0.03	3.12	$2.9 \cdot 10^{-3}$	27.1	9.4	0.1	870	4.26	AN18
5.00 ± 0.05	3.12	$3.8 \cdot 10^{-3}$	24.0	8.1	0.0	859	4.31	AN18
n.d.	3.12	$2.0 \cdot 10^{-3}$	27.3	9.5	0.2	910	4.11	AA20a
n.d.	3.12	$1.6 \cdot 10^{-3}$	28.5	10.0	0.6	745	4.86	AA20a
5.18 ± 0.04	2.88	$3.4 \cdot 10^{-3}$	32.1	11.9	1.8	916	3.80	AN18
n.d.	2.63	$8.9 \cdot 10^{-4}$	39.3	17.4	4.9	885	3.60	AA20a
n.d.	3.12	$1.1 \cdot 10^{-3}$	25.2	8.6	0.0	839	4.39	AN18
5.14 ± 0.08	3.16	$3.5 \cdot 10^{-2}$	24.5	8.2	0.0	810	4.59	AN18
5.25 ± 0.04	3.45	$1.3 \cdot 10^{-1}$	20.8	6.8	0.0	755	5.24	AA20a
n.d.	3.61	$2.2 \cdot 10^{-1}$	17.1	5.6	0.0	835	5.19	AA20a
5.18 ± 0.02	3.40	$3.9 \cdot 10^{-1}$	20.5	6.7	0.0	791	5.17	AA20a
5.32 ± 0.02	3.40	$3.5 \cdot 10^{-1}$	21.4	7.0	0.0	757	5.36	AA20a
5.36 ± 0.07	2.85	$5.1 \cdot 10^{-2}$	31.5	11.5	0.7	776	4.54	AN18
5.32 ± 0.02	3.19	$1.0 \cdot 10^{-2}$	24.2	8.0	0.0	784	4.94	AA20a
5.21 ± 0.03	2.96	$7.6 \cdot 10^{-3}$	28.2	9.6	0.0	733	4.92	AN18
4.53 ± 0.17	2.63	$8.0 \cdot 10^{-3}$	27.8	11.1	0.0	852	3.72	AA20a
3.91 ± 0.12	2.07	$1.8 \cdot 10^{-3}$	43.7	26.0	11.4	945	2.71	AA20a
n.d.	2.07	$1.0 \cdot 10^{-2}$	32.2	17.6	1.6	748	3.36	AA20a
n.d.	1.37	$1.1 \cdot 10^{-3}$	58.5	45.4	35.2	646	2.65	AA20a

ǂ XCT method; References: AN18: Allabar and Nowak (2018); AA20a: Allabar et al. (2020a).

where r is radius in m, η is viscosity in Pa·s and σ is surface tension in N·m^{-1}. Thus, t_{relax} is more than 10 times larger for a vesicle 250 µm in diameter than for a vesicle with 15 µm diameter. However, a quantitative calculation is not possible here, because the quenched vesicle sizes do not represent the changing radii in the cooling melt, and in addition, η undergoes a complex evolution because of simultaneous cooling and melt rehydration.

3.1 Quantification of melt porosity prior to quench

The textural observations of the samples indicate vesicle shrinkage during cooling. Therefore, it is assumed that Φ_{glass} and c_{H2OIR} do not represent Φ_{melt} and c_{H2O} of the melt prior to cooling, respectively. Thus, Φ_{melt} and c_{H2O} at P_{final} and T_d are initially unknown. Nevertheless, the relative importance of H_2O diffusion during decompression can be determined, which is quantified by the ratio of diffusion timescale τ_{diff} to the timescale of decompression τ_d (Hajimirza et al. 2019). If the diffusion timescale is shorter than the decompression timescale ($\tau_{diff}/\tau_d << 1$), near-equilibrium degassing is facilitated and the melt porosity and c_{H2O} prior to quench can be calculated.

In the decompression experiments with hydrous phonolitic melt, the vesicles in the central melt volume form in a single event (Allabar and Nowak 2018; Allabar et al. 2020a), so τ_d is the time between the P at which phase separation occurs and P_{final}. The τ_{diff} is defined as

$$\tau_{diff} \equiv \frac{l^2}{D_{H2O}} \tag{III.2}$$

where D_{H2O} is the total H_2O diffusivity in $mm^2 \cdot s^{-1}$ as a function of c_{H2O} in wt% and T in K, calculated after Fanara et al. (2013):

$$\log D_{H_2O} = -1.11 - 2.07 \log c_{H_2O} - \frac{(4827 - 4620 \log c_{H_2O})}{T} \tag{III.3}$$

The characteristic diffusion length l in mm is defined by the inter-vesicle distance calculated as follows (Hajimirza et al. 2019):

$$l = \frac{1 - \left(\frac{\Phi}{100}\right)^{\frac{1}{3}}}{\left(1 - \frac{\Phi}{100}\right)^{\frac{1}{3}}} \left(\frac{4\pi}{3} VND\right)^{-\frac{1}{3}} \tag{III.4}$$[2]

[2] Correction to original publication: In the published article, the "π" was wrongly replaced by the symbol "Φ" (Allabar et al. 2020c).

For a conservative estimate of l we use Φ_{glass} for calculations. A conservative estimate of D_{H2O}, and thus of τ_{diff}, is realized using the equilibrium c_{H2O} (c_{H2Oequ}) at the P_{final} of each experiment, which results in the slowest possible H_2O diffusivity. The c_{H2Oequ} at 1373 K for VAD79 phonolitic melt (Iacono-Marziano et al. 2007; Marxer et al. 2015) is calculated by:

$$c_{H_2O}^{1323\,K}[wt\%] = 0.2321 \cdot P[MPa]^{0.5928} \quad \text{(III.5)}$$

For the onset of vesiculation, we use 110, 70, and 50 MPa for samples with 5.3, 4.3, and 3.3 wt% c_{H2Oini} respectively, to calculate τ_d. The given P's are 10 MPa above the respective P_{final}, at which vesicles are observed in the vitrified samples. It may be possible that vesiculation starts earlier at higher P and vesicles were completely resorbed in the high P_{final} experiments (see argumentation below). However, the usage the given P's constitutes a conservative estimate for τ_d. The obtained τ_{diff}/τ_d values are all << 1 (Table III.2) suggesting near-equilibrium degassing during decompression prior to quench. The resulting equilibrium melt porosity at P_{final} (Φ_{equ}) prior to quench can be calculated (Gardner et al. 1999, Equation 5 therein):

$$\Phi_{equ} = \left[\frac{\frac{\rho_{melt}}{M_{H_2O}} \cdot V_m(H_2O) \cdot (c_{H2Oini} - c_{H_2Oequ})}{1 + \left(\frac{\rho_{melt}}{M_{H_2O}} \cdot V_m(H_2O) \cdot (c_{H2Oini} - c_{H_2Oequ})\right)}\right] \quad \text{(III.6)}$$

where melt density ρ_{melt} (Ochs and Lange 1999) and molar volume of H_2O fluid V_{mH2O} (Duan and Zhang 2006) are calculated for equilibrium conditions at P_{final} prior to quench (Table 2). Furthermore, near-equilibrium degassing is evidenced by similar Φ_{glass} observed in the central volumes of samples decompressed with different dP/dt to a similar P_{final}. The samples with ~5.3 wt% c_{H2Oini} that are decompressed at T_d of 1323 K to 80–82 MPa reveal similar Φ_{glass} of 3.3–7.0% with no systematic dependence on dP/dt in the range between 0.064–1.7 MPa·s^{-1} (Allabar and Nowak 2018). If disequilibrium degassing occurred prior to quench, significant increase in porosity with decreasing dP/dt at constant P_{final} would be expected, which is not observed here.

Since near-equilibrium degassing must have prevailed in the experiments, melt porosity equals Φ_{equ} and c_{H2O} of the melt equals c_{H2Oequ} prior to quench. This knowledge enables us to quantify vesicle shrinkage during cooling.

3.2 Vesicle shrinkage during cooling

For all samples, the Φ_{glass} observed at ambient conditions (0.1–24.4%) is significantly lower than the calculated Φ_{equ} prior to quench (17.1–58.5%, Table III.2, Fig. III.2). This is in line with c_{H2OIR} at ambient conditions (3.91–5.36 wt%) that are higher than c_{H2Oequ} prior to quench (1.37–3.61 wt%, Table III.2). These discrepancies suggest that both significant vesicle shrinkage and H_2O resorption occurred in the experimentally decompressed samples during cooling.

The extent of vesicle shrinkage increases with lower q, as demonstrated by sample CD66 (c_{H2Oini} = 5.22 wt%; P_{final} = 80 MPa; q = 16 K·s^{-1} isobaric), which has a lower Φ_{glass} of 0.5% compared to MQ experiments with identical Pfinal and similar c_{H2Oini} (q = 44 K·s^{-1}; Φ_{glass} = 1.5–9.0%). With slow cooling, more time is available for diffusion to resorb H_2O from the fluid back into the melt, and for the vesicle size to equilibrate to the decreasing internal vesicle P by viscous flow of the melt. The Φ_{glass} of 3.1% in CD 49 (q = 16 K·s^{-1} non-isobaric) is in the range of porosities of the MQ experiments. Vesicles of this sample shrunk less than expected for isobaric quench because the influence of decreasing P during cooling on V_{mH2O} and H_2O solubility in the melt dampens the effect of T decrease. When Φ_{glass} of the experiments CD41 and CD37 with unknown q are compared to the trend of experiments with 44 K·s^{-1} (Fig. III.2), it can be estimated that CD41 (P_{final} = 90 MPa; Φ_{glass} = 1.1%) experienced a q of 44 K·s^{-1} and CD37 (P_{final} = 80 MPa; Φ_{glass} = 1.9%) a non-isobaric q with 16 K·s^{-1}.

3.3 Quantification of vesicle shrinkage during cooling

Vesicle shrinkage can be calculated when the conditions prior to quench are known. Note that resorption shrinkage requires c_{H2Oequ} being adjusted in the melt prior to cooling (Ryan et al. 2015). Otherwise, when the cooling-induced increase of H_2O solubility of the melt does not exceed H_2O supersaturation during cooling, no driving force for resorption of H_2O from the fluid phase back into the melt evolves. In our experiments both EOS- and H_2O resorption-shrinkage occurred because cooling started from Φ_{equ} and c_{H2Oequ}.

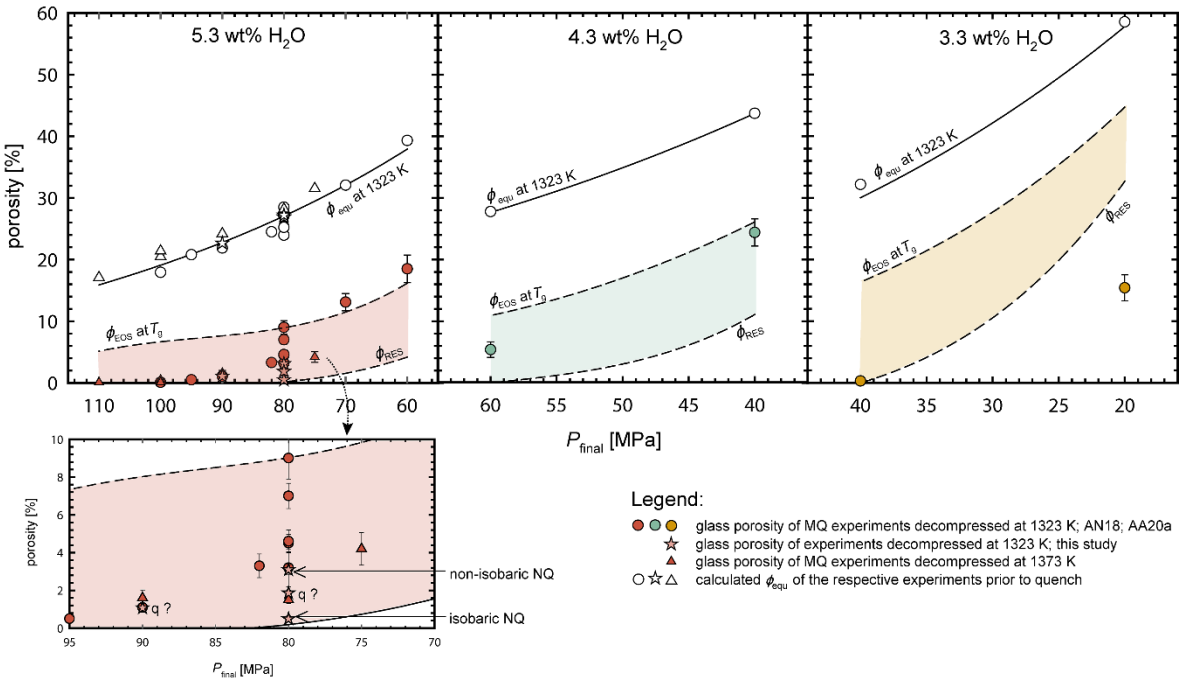

Fig. III.2 Observed glass porosities (Φ_{glass}) vs. P_{final} for 5.3, 4.3 and 3.3 wt% c_{H2Oini}. Equilibrium porosity (Φ_{equ}, solid line) is calculated for 1323 K and 5.3, 4.3 and 3.3 wt% c_{H2Oini}, respectively. The deviation of individual equilibrium porosity from the Φ_{equ} curve originates from slight variation in initial H_2O concentration or a slightly increased decompression temperature of 1373 K (triangles). Φ_{EOS} represents the calculated porosity at T_g related to EOS-shrinkage. Φ_{RES} is the minimum possible porosity taking additionally into account that H_2O is resorbed during cooling until T_{g_res} is reached, according to the H_2O solubility model of Shea (2017) (Equation III.8). Both Φ_{EOS} and Φ_{RES} are calculated for a cooling rate of 44 $K{\cdot}s^{-1}$. For details see text. The lower box is a zoomed excerpt of the 5.3 wt% c_{H2Oini} experiments for detailed visualization. References: AN18: Allabar and Nowak 2018; AA20a: Allabar et al. (2020a).

To demonstrate the contribution of each vesicle shrinkage mechanism to the overall shrinkage, we calculate in a first step solely EOS shrinkage down to T_g without any resorption (Marxer et al. 2015). For the melt with c_{H2Oequ} at the respective P_{final}, T_g was calculated (= T_{g_equ}) using the viscosity model of Giordano et al. (2008) and the cooling rate (44 $K{\cdot}s^{-1}$) dependent viscosity that defines the glass transition ($\log \eta = 9.66$ Pa·s; Dingwell and Webb 1990) where vesicle shrinkage is assumed to stop. The V_{mH2O} at P_{final} and T_d or T_{g_equ} can then be calculated (EOS of H_2O, Duan and Zhang (2006) for $T > 673.15$ K; WaterSteamPro™ (Orlov et al. 1999-2020 Version 6.5.0.64) for $T < 673.15$ K). The ratio of $V_{mH2O}(P_{final}, T_{run})$ and $V_{mH2O}(P_{final}, T_{g\_equ})$ corresponds to the shrinkage factor B_s (Marxer et al. 2015). This factor is then used to calculate the glass porosity by Equation. III.7 (Marxer et al. 2015, Equation. 4 therein) at T_g (Φ_{EOS}, Fig. III.2) when shrinkage started from Φ_{equ}:

$$\Phi_{EOS} = \frac{\Phi_{equ}}{\Phi_{equ} - B_s \cdot (\Phi_{equ} - 100)} \cdot 100 \quad \text{(III.7)}$$

However, this calculated Φ_{EOS} at T_g likely underestimates the real value, because the vesicles will effectively stop shrinking at a temperature > T_g due to limited viscous flow with increasing melt viscosity.

In a second step, we additionally account for resorption shrinkage because sample porosity is further reduced by H_2O resorption during cooling. Therefore, combined shrinkage by EOS and H_2O resorption was calculated using the rehydration quench method of Ryan et al. (2015) (Fig. III.3). Here, it is considered that T_g continuously decreases during cooling due to the H_2O resorption of melt (i.e., viscosity reduction). Ultimately, the melt is quenched to a glass when the T_g curve and retrograde H_2O solubility curve intersect (= T_{g_res}; Fig. III.3) defining the residual c_{H2O} in the glass after maximum possible resorption (c_{H2Ores}). Here, the T-dependent solubility Equation for phonolite from Shea et al. (2017) (which reproduces c_{H2Oequ} at 1323 K from Equation III.5 with < 3% relative deviation) was used to calculate temperature dependent solubility c_{H2O} curves during isobaric cooling (Fig. III.3):

$$c_{H_2O} = \frac{330P^{0.5} + 16P - 1.6P^{1.5}}{T} + 0.001P^{1.5} \quad \text{(III.8)}$$

where P is in MPa and T in K. The T_g curve was calculated for a cooling rate of 44 $K \cdot s^{-1}$ (Giordano et al. 2008; Dingwell and Webb 1990). Each cooling path is defined by the solubility curve, assuming that resorption effectively occurs until T_{g_res}. When the solubility reaches the c_{H2Oini} of the sample, T_{g_res} is equal to T_g of the melt with c_{H2Oini}. In this case, the degassed H_2O can be fully resorbed when the melt attains equilibrium H_2O content during cooling.

The possibility of complete resorption has consequences for experiments where the pressure difference required for (heterogeneous or homogeneous) phase separation (ΔP_{PS}) is intended to be determined. ΔP_{PS} is usually determined by finding the P at which vesicles are observable for the first time after decompression. If quench rates are used that allow vesicle shrinkage, vesicles may be fully resorbed until a certain pressure is reached and as a result ΔP_{PS} can be significantly overestimated by post mortem analysis of the vesiculated glasses. However, in this case, independent ΔP_{PS} estimates might be useful, e.g., using the widths of

the drainage zone in quenched samples to calculate the time needed to develop the diffusion width of the zone were no vesicles were formed due to insufficient supersaturation (Allabar and Nowak 2018) or by performing in-situ decompression experiments (Masotta and Keppler 2017). In turn, for all samples quenched at P for which the solubility curves in Fig. III.3 cross the T_g curve instead of ending at the rehydration limit, it can be ensured that vesicles will be observable in these samples. Shrinkage and resorption could also decrease the *VND* observed in vitrified samples when small vesicles are resorbed while large vesicles are not resorbed completely. However, in the experiments studied here, vesicles are similarly sized and we do not observe an increase of *VND* with decreasing P_{final}, suggesting that either all vesicles are resorbed to sizes below optical resolution or all vesicles remain at sizes above optical resolution during cooling.

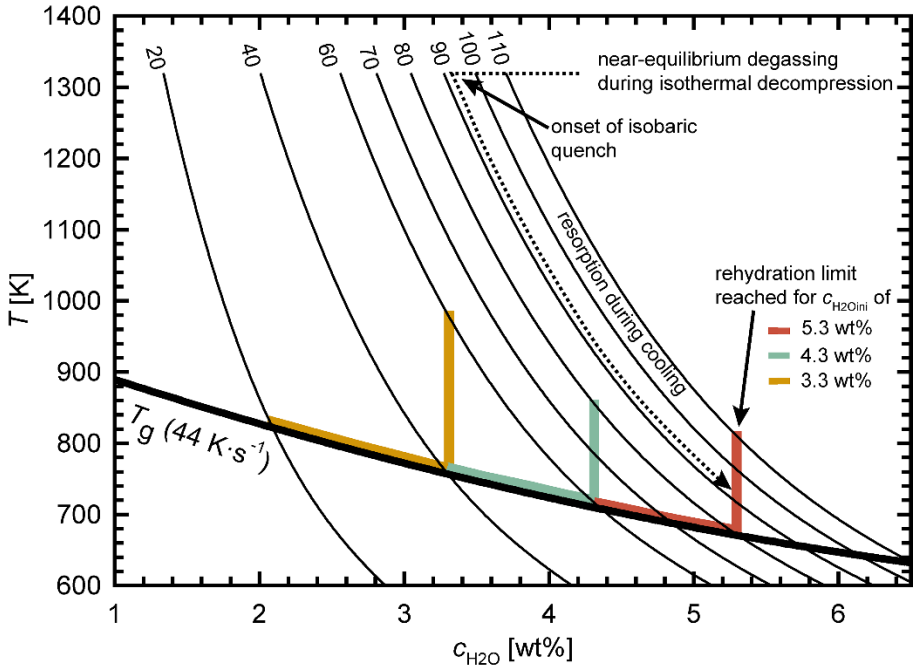

Fig. III.3 Rehydration quench scenarios using the method of Ryan et al. (2015) for P_{final} of the decompression experiments with c_{H2Oini} of 5.3–3.3 wt%, summarized in Table III.2. Isobaric H_2O solubility curves (thin black lines) for different P (in MPa) are calculated, using the H_2O solubility Equation for phonolitic melt from Shea et al. (2017) (Equation III.8). The T_g curve (thick black line) as a function of c_{H2O} for q = 44 K·s^{-1} was calculated with the viscosity model of Giordano et al. (2008) accounting for quench rate dependence of T_g (Dingwell and Webb 1990). The colored lines indicate the rehydration limit for the experiments summarized in Table III.2 defined by maximum possible resorbed c_{H2O}. These lines follow the T_g curve as long as the maximum resorbed c_{H2O} is < c_{H2Oini}. When the cooling-induced solubility increase reaches c_{H2Oini} (vertical colored lines), rehydration can be completed, and all vesicles will be fully resorbed if diffusion time is sufficient.

With T_{g_res} and the respective c_{H2Ores} the maximum extent of shrinkage and thus the minimum possible glass porosity (Φ_{RES}) was calculated (Fig. III.2). Φ_{EOS} and Φ_{RES} define an area (Fig. III.2), in which the glass porosity of the quenched experimental products are likely to be found, when they experienced equilibrium degassing prior to quench. At low P_{final}, one reason why this area becomes narrower is that the slopes of isobaric solubility curves are higher (Fig. III.3), which results in less resorption.

3.4 Comparison of calculated with observed porosities

Within error, the Φ_{glass} of the experimental samples with c_{H2Oini} of ~5.3 and ~4.3 wt% plot between the calculated Φ_{EOS} and Φ_{RES} (Fig. III.2). At high P_{final}, the glass porosities follow the resorption trend and then approximate the EOS trend at low P_{final} and higher porosities. This can be attributed to the higher residual c_{H2O} in the melt at high P_{final} resulting in a faster H_2O diffusivity (Equation 3) e.g., by half an order of magnitude at 100 MPa as compared to 60 MPa, assuming equilibrium H_2O content. Thus, resorption is expected to be more efficient at higher P_{final}. The variation of Φ_{glass} of the experiments quenched at a P_{final} of 80 MPa can be explained by slight variations in c_{H2Oini}, as it can also be seen in the variation of Φ_{equ} for the individual experimental samples as compared to the calculated Φ_{equ} as function of P_{final} for a sample with c_{H2Oini} of 5.3 wt% (Fig. III.2).

The Φ_{glass} of sample CD94 with c_{H2Oini} of 3.3 wt% and P_{final} of 40 MPa is close to the calculated Φ_{RES} trend, which can be explained by the high log*VND* of 5.96. This value is almost one order of magnitude higher than the log*VND* of ~5 in the 5.3 wt% c_{H2Oini} experiments (Table 2). Despite the slower H_2O diffusivity, the inter-vesicle distance (< 10 μm) in the 3.3 wt% experiments is roughly half of that of the 5.3 wt% experiments, which in turn improves efficiency of H_2O resorption. This results in similarly low τ_{diff}/τ_d for experiments with c_{H2Oini} of 3.3 wt% as compared to experiments with higher c_{H2Oini} of 5.3 wt%. The glass porosity of CD95 with c_{H2Oini} of 3.3 wt% H_2O and a P_{final} of 20 MPa is below the minimum possible value (Φ_{RES}). Possibly, in this sample equilibrium porosity was not achieved prior to quench. An H_2O supersaturation prior to quench would counteract resorption until the solubility curve exceeds the residual c_{H2O} of the melt. Vesicle shrinkage would then start from a melt with porosity < Φ_{equ}, but solely by EOS-shrinkage. However, according to the calculations above, diffusion must have been fast enough for equilibrium degassing and viscous retardation of vesicle growth is not expected due to a low viscosity of 10^3-10^4 Pa·s

(Thomas et al. 1994). However, according to Toramaru (1998) the effective viscosity of a vesicle-rich silicate melt is larger for pure melt with identical c_{H2O} if the fluid phase is stored in a large *VND* of small isolated vesicles. The two experiments with 3.3 wt% c_{H2Oini} are those with the highest log*VND* of ~6. This high *VND* might have caused a high bulk viscosity, limiting equilibrium growth of the vesicles. Furthermore, the sample decompressed to 20 MPa might have an unpredictably low glass porosity, because it was quenched close to the critical point of H_2O, where slight changes in *T* and *P* have a large effect on fluid density and calculations close to this point might be prone to large errors. Therefore, these two experiments might not be suitable for the shrinkage calculations presented here, where degassing close to equilibrium prior to quench is a pre-requisite. Thus, the experiments with c_{H2Oini} of 3.3 wt% were not considered for the following calculations.

3.5 Determination of T_f where vesicle shrinkage effectively stops

We conclude, that EOS and resorption driven vesicle shrinkage effectively stops at temperatures $T_f > T_{g\_res}$. This is based on the observation that Φ_{glass} of the investigated samples with 5.3 and 4.3 wt% c_{H2Oini} are higher than Φ_{RES} (Fig. III.2). Different methods can be applied to determine T_f:

3.5.1 Determination of T_f via glass porosity

For the determination of T_f from Φ_{glass}, we assume that the observed glass porosity represents the equilibrium porosity of the supercooled melt at T_f, where vesicle shrinkage effectively stops. Equation III.7 can be used to calculate the *T* dependent Φ_{equ}, and therefore, we find the temperature T_f (and the resulting ρ_{melt}, V_{mH2O} and H_2O solubility) at known P_{final} and c_{H2Oini}, where Φ_{glass} matches the calculated porosity (Fig. III.4). The T_f for samples with 5.3 and 4.3 wt% c_{H2Oini} and a *q* of 44 $K \cdot s^{-1}$ range between 733 and 945 K, while T_f is lower at 16 $K \cdot s^{-1}$ with 683 and 767 K (Table III.2).

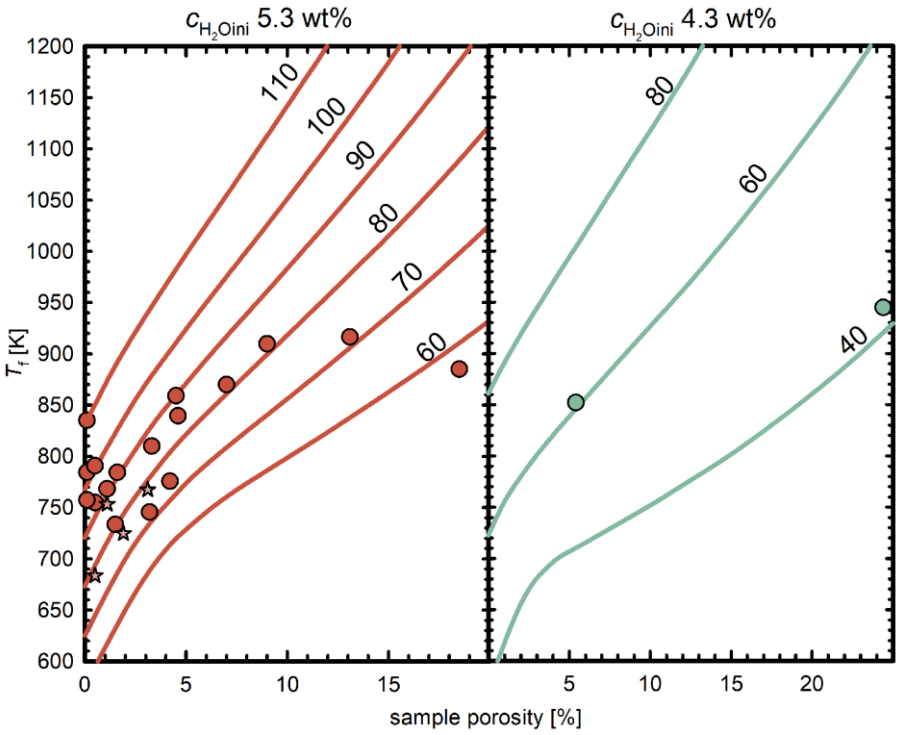

Fig. III.4 Determination of T_f from glass porosity. Temperature dependent equilibrium porosities are exemplarily calculated for 5.3 and 4.3 wt% c_{H2Oini} at the different P_{final} (given in MPa next to each line) at which the samples were quenched. T_f was calculated based on the glass porosity, P_{final} and the individual c_{H2O} of each sample. The data points show the T_f that is derived from glass porosity of each sample. They do not all plot exactly on the curves calculated for the respective P_{final}, due to small deviation of c_{H2Oini} of the experiments from the H_2O concentration that the curves were calculated for. Experiments with c_{H2Oini} of 3.3 wt% were not considered here because they may not have achieved equilibrium H_2O content prior to quench, which however is a pre-requisite for the T_f calculation (for details see text).

3.5.2 Determination of T_f via the H_2O liquid to vesicle volume ratio – application of XCT analysis

An independent method for determining the extent of vesicle shrinkage is provided by the ratio of liquid H_2O volume (V_{H2Ol}) in quenched vesicles to total vesicle volume (V_{ves}) using XCT analysis (McIntosh et al. 2015).

During decompression, the exsolved H_2O fluid is supercritical because P_{final} and T exceed the critical point of H_2O. During cooling, vesicles shrink until T_f is reached. Below T_f the vesicle volume remains constant during further isochoric cooling and consequently, the pressure inside the vesicles starts to drop. The supercritical fluid follows a path of constant density until the liquid-vapor phase boundary is reached, after which the liquid-vapor ratio changes with the P in the vesicles following the water-steam equilibrium curve until ambient

T is reached. H_2O present as vapor and liquid at room temperature results in an internal vesicle P of 0.035 bar. The volume of liquid water (water vapor can be neglected in this case due to its low density) gives an approximation of the amount of H_2O fluid trapped at T_f. As the amount of liquid water observed at ambient T would completely fill the vesicle volume at P_{final} as a single phase fluid, we can calculate T_f from the equation of state of H_2O. This method does not require knowledge of EOS- and H_2O resorption-contribution to shrinkage.

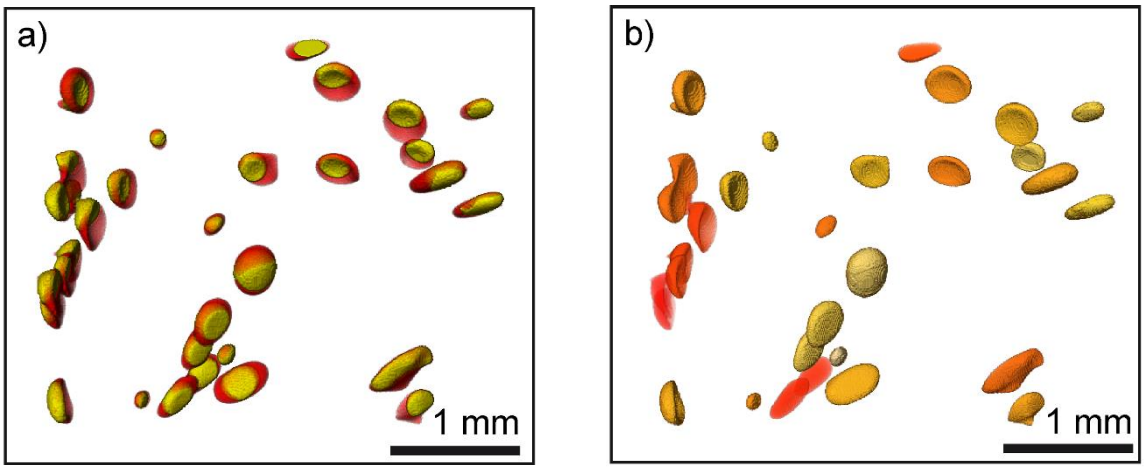

Fig. III.5 a) XCT-images of large vesicles in the central vesiculated volume of CD74 that are filled with vapor (yellow) and liquid H_2O (red) at ambient conditions. Volume of liquid H_2O to vesicle volume ratios were used to calculate T_f where vesicle shrinkage stops. Due to capillary forces, the liquid water is not gravitationally located at the bottom of each vesicle. b) same vesicles color coded for T_f, with light yellow for high T_f towards orange for low T_f. Edge length of the XCT images are approximately 3.6 mm.

XCT-imaging reveals, that larger deformed vesicles are distributed within the central finely vesiculated volume of the MQ sample CD74 (Fig. III.5a). The large vesicles may be ascended fringe vesicles or a product of coalescence (Allabar et al. 2020a). The smaller dispersed spherical vesicles are close to the limit of XCT resolution and were therefore not included in the V_{H2Ol} analysis. Analysis of vesicles in CD74 yield V_{H2Ol} to V_{ves} ratios between 0.56 and 0.20, corresponding to T_f between 710 and 954 K, respectively (Fig. III.6) with a random spatial distribution of T_f within the sample (Fig. III.5b). The T_f estimates from XCT analysis are within the range of T_f derived from the glass porosity calculations (Fig. III.7). The mean value of 810 K can be assumed, if cooling was homogeneous throughout the sample implying that a single temperature T_f is valid for the vesiculated part of the sample. However, we propose that vesicle shrinkage within an experimental sample may be a complex process including competition of vesicles in close vicinity (including the small, finely dispersed

vesicle population) and the ability of a vesicle to achieve efficient volume reduction by deformation that will depend on its surrounding. These processes may lead to differences in T_f of individual vesicles.

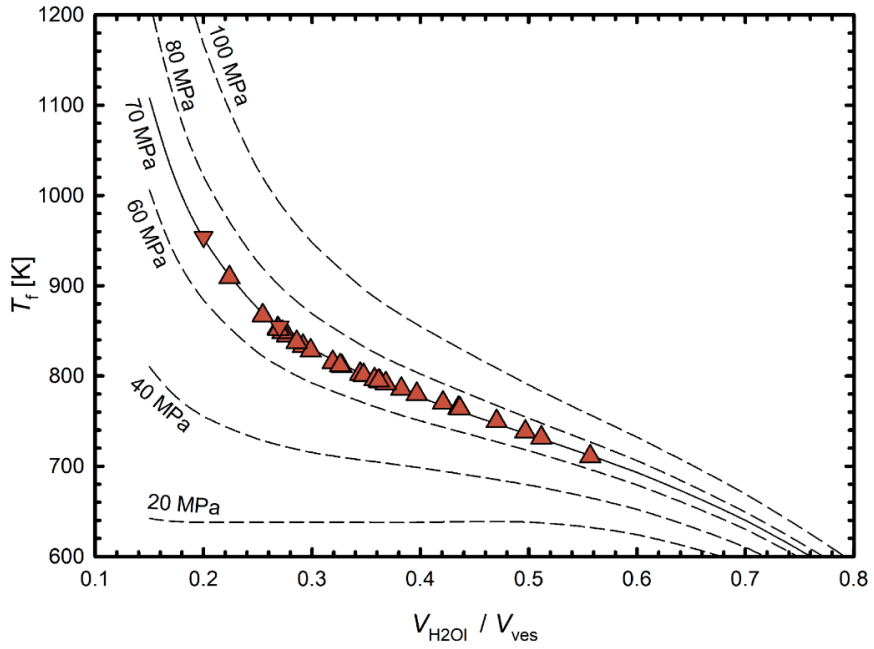

Fig. III.6 T_f's determined from individual large vesicles in CD74 using the ratio of the volume of liquid H_2O in the vesicle to the total vesicle volume based on XCT data (Fig. III.5) handled by automated analysis (triangles up) and manual analysis (triangles down). The determined volume ratios at P_{final} of 70 MPa define a T_f range between 710 and 954 K for CD74. The additional dashed curves are exemplarily shown for different P_{final}.

Together, the methods of estimating T_f (Fig. III.7) show that for samples with 5.3 and 4.3 wt% c_{H2Oini}, vesicle shrinkage stops up to 200 K above T_g, and that the relationship between T_f and P_{final} is similar to the relationship between T_g and P_{final}. We assume that T_f derived from Φ_{glass} reveals a mean T_f for the whole central sample volume comparable to the mean T_f from XCT analysis. Using T_f and the P_{final} for each sample, the theoretical residual c_{H2O} in the supercooled melt at T_f (= c_{H2Ores_Tf}) can be calculated (Fig. III.7), and used to define the viscosity at which vesicle shrinkage stops. The viscosity $\eta_{\_Tf}$ ranges from 10^6 to 10^8 Pa·s at 44 K·s^{-1} and appears to be independent of P_{final}. For cooling with 16 K·s^{-1}, we find a $\eta_{\_Tf}$ of 10^8 and 10^9 Pa·s due to lower T_f as a result of slower cooling.

At lower viscosities (above T_f) it is likely that the vesicles instantaneously shrink to their equilibrium size. This instantaneous growth and shrinkage has been shown in in-situ experiments (Masotta and Keppler 2014) demonstrating pressure cycling induced vesicle volume changes in a melt with a viscosity of $8.5 \cdot 10^5$ Pa·s.

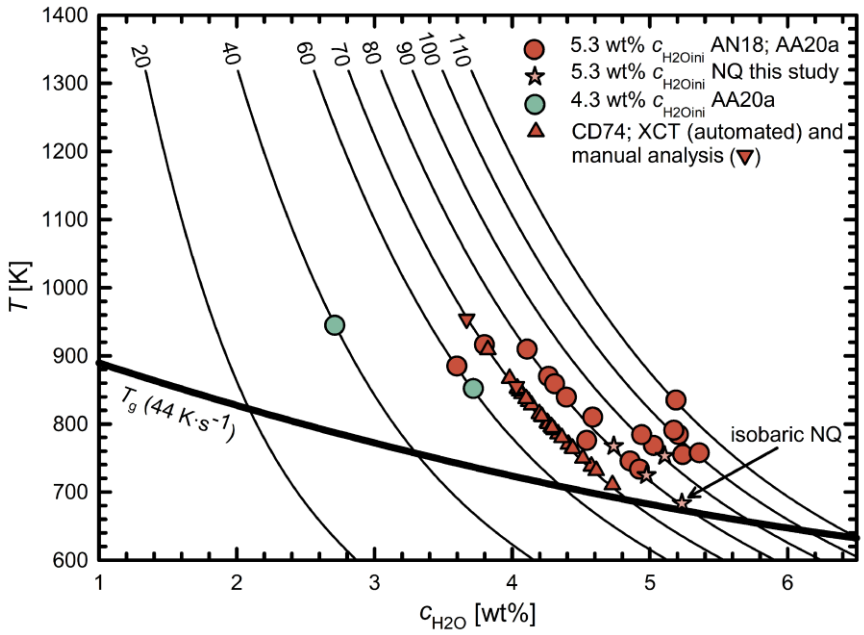

Fig. III.7 Summarized T_f's of samples calculated from both Φ_{glass} (Fig. III.4) and XCT data (Fig. III.6) in the same plot as Fig. III.3. Each solubility curve (black lines) is labeled with the corresponding P in MPa. T_f's are up to 200 K higher than T_g, which means that vesicle shrinkage stops significantly before T_g is reached. Isobaric NQ (16 K·s^{-1}) reveals the lowest T_f because more time was available for vesicle shrinkage driven by H_2O resorption and viscous flow of the melt compared to MQ (44 K·s^{-1}). The XCT data based T_f's are qualitatively consistent with T_f's calculated from glass porosity. References: AN18: Allabar and Nowak (2018); AA20a: Allabar et al. (2020a).

3.6 Uncertainties of vesicle shrinkage calculations

The H_2O solubility Equation (Equation III.8) used here is based on experimentally determined H_2O solubility in phonolitic melt over P and T ranges between 20–395 MPa and 1123–1473 K (Shea 2017, Equation 8 therein). Since there is no experimental access to low T and P, H_2O solubility data in phonolitic melt between liquidus T and T_g due to crystallization, the applicability of this solubility model is uncertain, but remains up to now the only option to estimate H_2O resorption. While it is assumed that towards lower T, phonolitic melts would exhibit a strong increase in H_2O solubility as seen in haplogranitic melt (Shea 2017; Liu et al. 2005), this remains unconstrained.

An alternative H_2O solubility model, which is based on the assumption of thermodynamic equilibrium (Ottonello et al. 2018), allows further tests. However, it predicts a smaller increase of solubility with decreasing T, which contrasts with the high c_{H2OIR} measured in the glass between the vesicles (e.g., c_{H2Ores} of ~4.3 wt% calculated with the model for P_{final} = 80 MPa at T_{g_res}, compared to ~5.3 wt% derived from Equation 8 and ~5 wt%

measured in the glasses). H_2O resorption in samples of this study occurs in a T ranging between T_d and a temperature below the liquidus in the metastable state. In the H_2O solubility model of Liu et al. (2005) for rhyolitic melts, experimental data determined below the liquidus are included, which cannot be described by thermodynamic equilibrium. Since the H_2O solubility (Equation. III.8) is based on these data, it is suggested that this dependence is more suitable for quantifying resorption processes of supercooled melt apart from equilibrium.

A further uncertainty in our calculations is that pure H_2O is assumed to be in the vesicles rather than an H_2O fluid with dissolved silicate components, which may influence the EOS parameters. However, at such low P, the solubility of melt components in H_2O fluid is low (e.g., Stalder et al. 2000). Therefore, this will have only a minor influence on our calculations.

3.7 H_2O concentrations measured with FTIR and Raman micro-spectroscopy

The results of the FTIR-ATR mapping and RMS mapping on sample CD73 are shown in Fig. III.8. In both the FTIR-ATR-map and the RMS-map an increase in $c_{H2Oglass}$ towards vesicles is detected, testifying H_2O resorption during cooling. With both methods, this can be clearly seen in the case of the vesicle just below the glass surface (marked with an arrow in Fig. III.8a), with a resorption halo intersecting the sample surface. However, the results of the two methods differ with respect to the area of increased $c_{H2Oglass}$ above this vesicle that appears to be larger in the RMS-map. Additionally, the resorption halos with increased $c_{H2Oglass}$ around intersected vesicles are clearly visible only in the FTIR-ATR-map. We attribute this to the different beam penetration depth of the two methods. In case of the FTIR-ATR measurements, the effective penetration depth is ~0.25 µm (calculation after Compton and Compton (1993) given in the supplement "RMS and FTIR supplementary information"). Penetration depth of the RMS measurement must be higher to explain the RMS data. To get an estimate on RMS-penetration depth, we used a VAD79 thin section that was polished to ~20 µm thickness and measured it on top of a Si single-crystal standard that is usually used for the performance check of the spectrometer. With the same measurement conditions as for the mapping of the vesiculated samples, we find a distinct Si-Raman signal although the laser beam was focused at the glass sample surface. Thus, the penetration depth of the laser is > 20 µm. However, the effective penetration depth that quantitatively determines the c_{H2O}

result is unknown. The large laser penetration depth is consistent with the study of Everall (2000), who finds that depth resolution of Raman spectroscopy is limited and usually worse than expected. Depth resolution gets worse by focusing into the sample volume, such that a 5 µm focus depth results in an illuminated depth of ~18 µm at a refractive index of 1.5 (Everall 2000). For glasses with homogeneously dissolved H_2O, it is usually suggested to use an optimal focus depth where HW and LW bands are at a maximum intensity (~5-10 µm focus depth depending on glass composition; Schiavi et al. 2018; Di Genova et al. 2017a) because this reduces the error in c_{H2O} by focus inaccuracies. However, this approach should not be used for samples inhomogeneous in c_{H2O} for which a high spatial resolution *and* depth resolution is desired.

The large penetration depth using RMS of at least 20 µm has to be considered for the interpretation of $c_{H2Oglass}$ between vesicles. In detail, a c_{H2O} profile extracted from the RMS-map between two vesicles below the surface is shown by the A-B profile (Figs. III.8a, c, 9). In transmitted light, a diameter of ~20 µm of the vesicles below the surface of the A-B profile was determined. The vesicle at the profile end B is ~1 µm below the surface, which is also indicated by the diffraction rings on the transmitted light microscopy image of the sample surface (Fig. III.8a). The other vesicle at B is slightly deeper (Fig. III.9). In the A–B profile (Fig. III.9) the c_{H2O} determined from the HW calibration (3450 cm^{-1} band only, i.e., total H_2O) decreases when approaching vesicles that are several microns below the surface, while the c_{H2O} from HW/LW calibration further increases. The latter is related to the HW/LW calibration that reflects H_2O concentration per glass volume and is thus independent from the measured glass volume. A lower c_{H2O} near the vesicle at the profile end A is measured because the vesicle is located deeper below the sample surface. Compared to the vesicle at profile end B, which is closer to the surface (Fig. III.9), a larger glass volume with less H_2O is measured at profile end A. This dilutes the Raman signal of resorption halos near the vesicle (Fig. III.9). The same dilution problem occurs when measuring in the vicinity of intersected vesicles. Because of the large penetration depth of Raman spectroscopy measurements, the increased $c_{H2Oglass}$ around the vesicle, which extends only a few micrometers away from the vesicle, is diluted by H_2O poorer glass underneath (Fig. III.A3 in supplement "RMS and FTIR supplementary information"). Thus, resorption halos of intersected vesicles are clearly visible only in the FTIR-ATR-map.

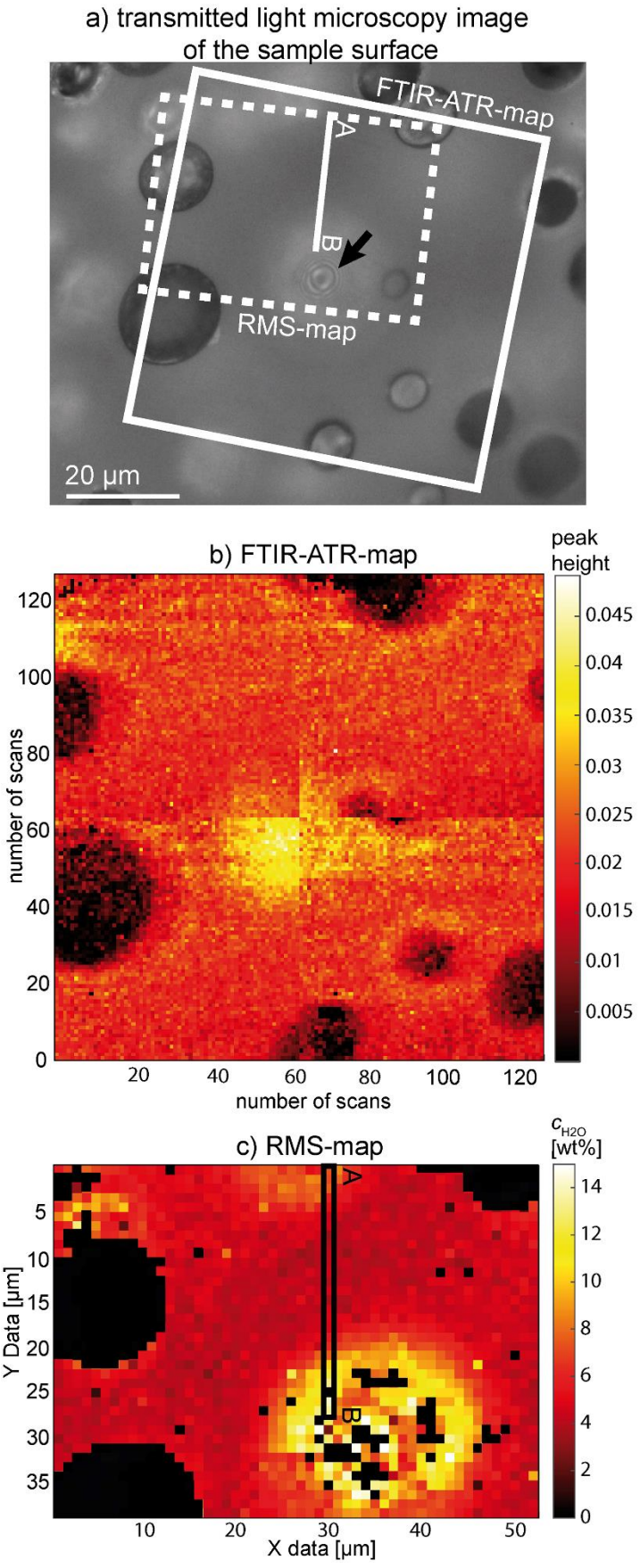

Fig. III.8 a) Transmitted light microscopy image of the mapped area of CD73 focused at the sample surface. The arrow is pointing at the central intact vesicle that is located ~1 µm below the surface, as indicated by the light diffraction rings. The frames indicate the areas of FTIR-ATR and Raman micro-spectroscopy (RMS)-mapping. b) FTIR-ATR map based on 128×128 MIR spectra representing a sample area of 70×70 µm stitched by 4 frames (64×64 spectra each) showing a slight lateral offset. Spectra of each 64×64 frame were monitored simultaneously with a focal plane array MIR detector. Quantitative c_{H2O} determination was not calibrated due to a small tilt of the Ge-ATR crystal relative to the sample surface. Therefore, the pixel are color coded for the peak height of the 3450 cm^{-1} fundamental OH stretching band, representing total dissolved H_2O near the surface of the intersected sample. c) RMS-map: color coded c_{H2O} concentrations derived from Rama spectra. RMS measurements that are affected by epoxy or carbon relicts (mostly within the intersected vesicles from preparation and previous carbon coating for SEM imaging), are colored black.

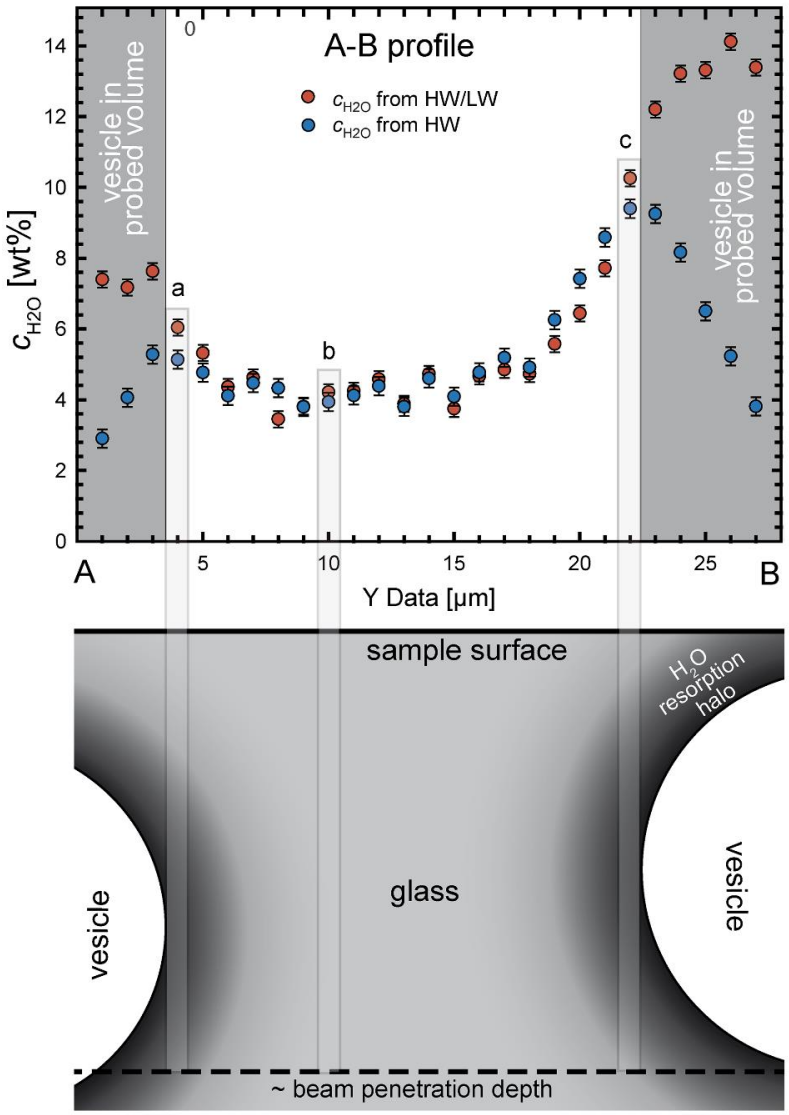

Fig. III.9 Raman measured c_{H2O}–distance profile from position A to B as indicated in Fig. III.8a,c. c_{H2O} from both HW and HW/LW calibration, is shown. Errors in c_{H2O} relate to the errors of calibration using hydrous VAD79 samples with different c_{H2O} (for details see supplement "RMS and FTIR supplementary information"). Below is a schematic illustration of the A–B intersection of the sample below the surface. The vesicle at profile end A is positioned slightly deeper than the vesicle at the end B, which is ~1 µm below the surface. In the schematic intersection, the vesicle is drawn slightly deeper because the profile approaches the vesicle slightly lateral. The penetration depth of the laser beam during RMS measurements was determined to be at least 20 µm as indicated by the dashed line. Thus, the measurements with a vesicle in the probed beam yield different c_{H2O} values, dependent on HW and HW/LW calibration (data in grey areas; for details see text). All other measurements are unaffected by the vesicles. The highlighted bars indicate the illuminated volume yielding the resulting c_{H2O} to which they are connected in the plot above. The c_{H2O} at position a is lower than at position c because the high c_{H2O} of the H_2O resorption halo (shaded in black to dark grey) around the vesicle A is more diluted by H_2O poorer glass towards the sample surface compared to vesicle B.

Despite the high penetration depth, we can use the H_2O contents from the RMS-map, which are not influenced by a vesicle in the measured volume. Theoretically, the HW/LW values with vesicles in the probed volume represent the H_2O content in the glass above the vesicle. However, we do not know whether the vesicle wall has a reflectance effect on the laser beam, which could distort the signal. Because of this uncertainty, we only consider measurements without vesicles in the probed volume. This is the case for measurements for which the HW and HW/LW calibration provide identical results within error (Fig. III.9). We exclude all measurements from further interpretation, where the deviation of the two values is greater than the relative change to the nearest value (Fig. III.9, data with grey background). In the sample volume between the vesicles, a relatively homogeneous c_{H2O} of ~4.3 wt% is measured, which is significantly higher than calculated equilibrium c_{H2O} of 2.6 wt% at P_{final}. McIntosh et al. (2014) found ~20 µm diffusion profiles (with 12 µm half fall distance) in a phonolitic sample after rapid cooling within 3–10 s at 100 MPa. Therefore, it can be assumed that sample CD73 with diffusion lengths of ~10 µm and cooling within ~20 s has adjusted to the measured $c_{H2Oglass}$ of 4.3 wt% between the vesicles by resorption, although the melt had a low equilibrium c_{H2O} of ~2.6 wt% at P_{final} prior to cooling. We attribute the steep increase of c_{H2O} towards the vesicles to resorption at a late stage, where solubility strongly increases and concurrently, diffusivity decreases during cooling, becoming too slow for equilibrating the entire supercooled melt volume between the vesicles. Thus, the shape of such diffusion profiles results from the interplay of the timescale of cooling with the H_2O solubility increase and diffusivity decrease.

All c_{H2O} values measured between the vesicles of CD73 are above the calculated c_{H2Ores_Tf}. This is also the case for the NIR-FTIR transmission measurements through the glass without vesicles in the beam (Table III.2). These measurements resemble a mean c_{H2O} between vesicles, but with unknown contribution of steep H_2O gradients towards vesicles. Nevertheless, the general observation of higher c_{H2O} in the glass compared to calculated values may indicate, that further H_2O diffusion occurs below T_f without further vesicle shrinkage (McIntosh et al. 2014). Assuming isochoric behavior of vesicles below T_f, H_2O diffusion from fluid to melt or glass below T_f changes the proportions of H_2O liquid and vapor observed at ambient T and may affect the T_f determination using XCT data. To test this, the liquid H_2O proportion in small vesicles of the pervasive clouds need to be analyzed in the future, where resorption is expected to be much more effective due to short diffusion distance than in the

large vesicles that were used here. Alternatively, the discrepancies between c_{H2Ores_Tf} and c_{H2O} measured in the glasses can also originate from an underestimation of H_2O solubility towards low T by Equation III.8. Additionally to the discussion of experiment CD95 above, this could be an alternative reason for the mismatch between calculated and observed porosity.

3.8 Impact of experimental technique on vesicle shrinkage

Quantification of vesicle shrinkage in post-mortem analyzed H_2O-vesicle bearing samples requires knowledge of the experimental apparatus and the quench technique used (Fig. III.10). When samples are quenched isobarically, EOS shrinkage and resorption will be driven by T drop only (case 1 in Fig. III.10). For a non-isobaric quench, shrinkage will depend on the pressure medium that surrounds the sample and on the magnitude of pressure drop. When gas is used as pressure medium, P drops during cooling (CD49, this study). However, the P drop within the autoclave is less than that expected from a simple EOS calculation of the gas because only part of the gas volume of the IHPV is heated prior to quench. Nevertheless, V_{mH2O} decreases stronger during cooling than the V_{mgas} of the pressure medium.

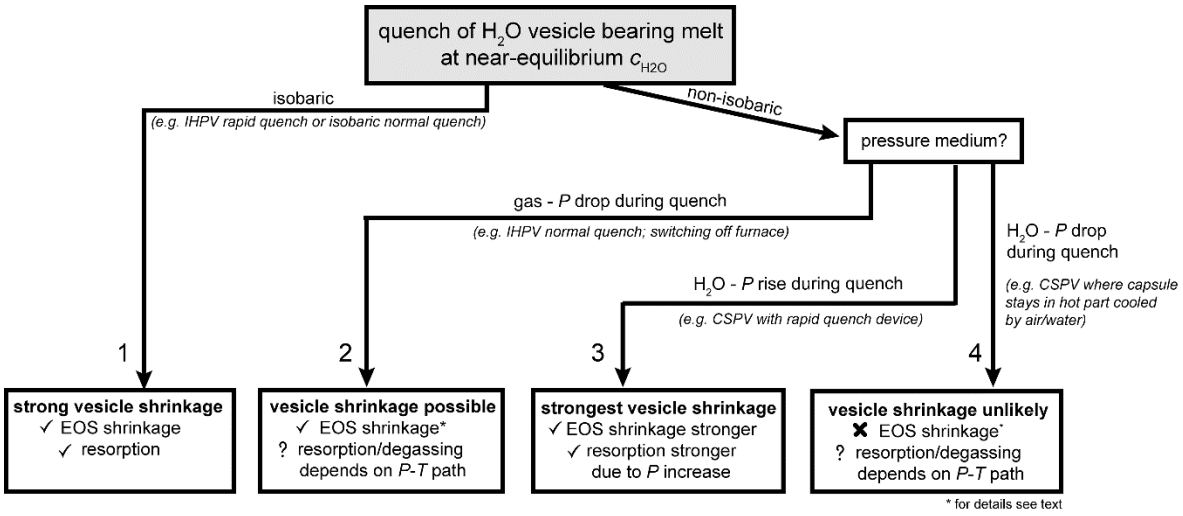

Fig. III.10 Flowchart for illustrating the impact of different experimental quench techniques on H_2O-vesicle shrinkage in melts that reached near equilibrium c_{H2O} prior to quench. For a constant cooling rate, vesicle shrinkage and the single contributions (EOS- and resorption-shrinkage) will vary according to the shown quench conditions.

The pressure inside the vesicle will drop relative to the pressure medium and EOS shrinkage is facilitated (case 2). Test experiments in cold seal pressure vessels (CSPV), using H_2O as pressure medium, revealed that P may rise by up to 10 MPa during cooling when a rapid quench device is used because the hot capsule and parts of the guide rod heats the water

in the cold part of the vessel by dropping in it. In this case, the strongest vesicle shrinkage is possible because the *P* increase supports resorption by solubility increase and compression of H_2O according to the EOS (case 3). If the sample remains in the hot section and the vessel is cooled by compressed air or water externally (e.g., Larsen and Gardner 2004), both the pressure inside the autoclave and the vesicles will drop during cooling according to EOS of H_2O, provided the *P* is not actively held constant. Because there is no *P* difference between the vesicles and the pressure medium, there will be no driving force for EOS-shrinkage (case 4). However, during cooling accompanied with a *P* drop, the retrograde *T* dependence of H_2O solubility will compete with the *P*-induced solubility decrease. Shrinkage in such an experiment is unlikely or will be of minor extent. However, the prerequisite for shrinkage to occur at all is that some time for melt relaxation and diffusion is given. Theoretically, a sample has to cool infinitely fast to prevent vesicle shrinkage. The experiments summarized in this study belong to case 1 (MQ and NQ isobaric) and case 2 (CD49).

3.9 Review of experimentally derived porosities in phonolitic melt

Numerous decompression experiments have been performed using hydrous phonolitic melts (Larsen and Gardner 2004; Iacono-Marziano et al. 2007; Larsen 2008; Mongrain et al. 2008; Shea et al. 2010a; Gardner 2012; Marxer et al. 2015; Preuss et al. 2016; Allabar and Nowak 2018; Allabar et al. 2020a). When these data are compiled with the data of this study (supplement "Literature review") we can evaluate the effect of vesicle shrinkage during cooling also in these experiments, which are quenched with more commonly used rapid quench protocols (> 100 $K \cdot s^{-1}$). We include only such data where H_2O was the only volatile, degassing occurred in a closed system and glass porosity and *VND* were reported for experiments quenched at P_{final} > 22.1 MPa (above the critical point of H_2O).

For the compiled experimental data, we calculated whether near equilibrium H_2O content can be adjusted prior to quench (see calculations described above). Therefore, when available, the solubility data of each study were used for H_2O solubility at given run conditions. Otherwise, the general H_2O solubility dependence for phonolitic melt (Equation III.8) was used and H_2O diffusivity was calculated with Equation III.3 (Fanara et al. 2013). For all experiments, in which near-equilibrium porosity was adjusted prior to quench, the equilibrium porosity was calculated. The Φ_{glass} vs. Φ_{equ} is shown in Fig. III.11. In about half of the decompression experiments, vesicle shrinkage has likely occurred during cooling

($\Phi_{glass} < \Phi_{equ}$), despite faster quench rates (150–200 $K \cdot s^{-1}$) than in our study. The occurrence of vesicle shrinkage even at these high cooling rates is consistent with the large resorption-induced H_2O gradients towards vesicles rims found by McIntosh et al. (2014) in phonolitic glasses after cooling within 3–10 s from T_d to ambient T. The varying degrees of vesicle shrinkage presented in in Fig. III.11 can be attributed to the following parameters:

3.9.3 Different experimental techniques

Experiments from studies using gas as pressure medium ((G) in Fig. III.11) experienced a near isobaric quench (case 1, Fig. III.10), and showed large degrees of vesicle shrinkage, varying with quench rate (Fig. III.11). For most studies using H_2O as pressure medium ((W) in Fig. III.11) the actual quench rates and P changes during cooling are not known. Thus, direct comparison is not possible. One study reports a slight P increase of 5 MPa during quench (case 3, Mongrain et al. 2008). Therefore, stronger vesicle shrinkage is expected but not observed (Fig. III.11). This is likely due to higher cooling rate (> 100 $K \cdot s^{-1}$) compared to the studies using gas as pressure medium and the possibility of pre-existing hydration vesicles (see below).

3.9.4 Run temperature

Φ_{equ} increases with T_d and consequently the difference between the experimental T_d and T_f increases, enhancing vesicle shrinkage. The compiled data suggest an increase in vesicle shrinkage with increasing T_d. However, several mechanisms contribute to shrinkage, and run temperature is not solely responsible for the varying degree of vesicle shrinkage.

3.9.5 Hydration vesicles prior to decompression

For some experiments, glass powder was used as starting material. During hydration, H_2O vesicles can remain in the hydrated melt at H_2O supersaturated conditions prior to decompression, resulting in a melt with up to 12% porosity prior to decompression (Larsen 2008). These pre-existing fluid vesicles can cause artificially high glass porosities close to, or above the equilibrium line. Vesicle shrinkage might therefore still have occurred during cooling.

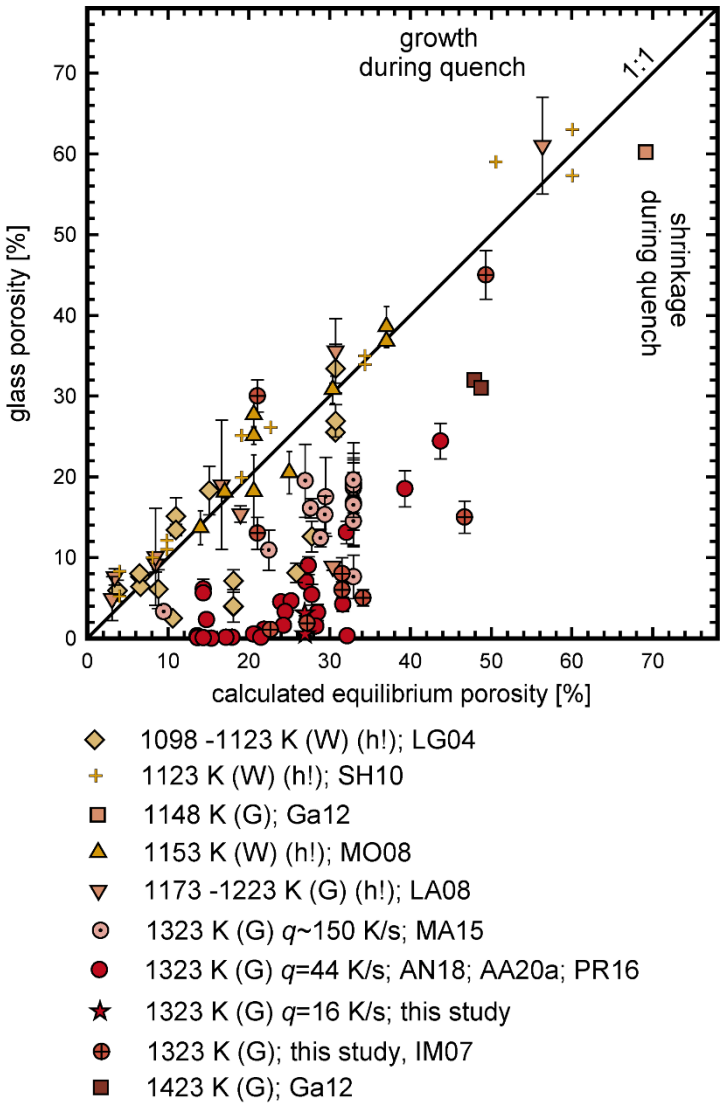

Fig. III.11 Observed glass porosities vs. calculated equilibrium porosities for all decompression experiments with hydrous phonolitic melt composition, in which near-equilibrium degassing was facilitated prior to quench. (G) gas as pressure medium, (W) water as pressure medium. When *q* and error bars are not given, they are unknown. (h!) hydration vesicles might have been present prior to decompression due to the use of powder as starting material and H_2O supersaturated conditions prior to decompression. The experiments with melts containing hydration vesicles are the only ones plotting close to the 1:1 line, suggesting that no vesicle shrinkage occurred. The presence of a pre-existing fluid phase, however, can shift the glass porosities of the quenched samples to higher values towards or above the 1:1 line, although shrinkage occurred. Additionally, other reasons might also influence the glass porosity of these samples (see text). All data of other samples plot below the 1:1 line indicating vesicle shrinkage during cooling. A faster cooling rate (150 $K \cdot s^{-1}$) leads to slightly less shrinkage (MA15) compared to slower cooling (44–16 $K \cdot s^{-1}$; this study) References: LG04: Larsen and Gardner (2004); SH10: Shea et al. (2010); GA12: Gardner (2012); MO08: Mongrain et al. (2008); LA08: Larsen (2008); MA15: Marxer et al. (2015); AN18: Allabar and Nowak (2018); AA20a: Allabar et al. (2020a); PR16: Preuss et al. (2016); IM07: Iacono-Marziano et al. (2007). Compilation of data can be found in the supplement "Literature review").

3.9.6 Crystallization

Some experiments (Mongrain et al. 2008; Larsen and Gardner 2004; Larsen 2008; Shea et al. 2010a) were performed below the liquidus and crystals are reported or documented in the SEM images. Crystals increase the bulk viscosity (e.g., Costa 2005), which could decrease the degree of vesicle shrinkage due to the shift of T_f towards higher values.

4. Conclusion

Significant vesicle shrinkage can occur during cooling of vesicle-bearing silicate melts that achieved near-equilibrium c_{H2O} during decompression. The degree of vesicle shrinkage (EOS- and H_2O- resorption shrinkage) varies with experimental technique and quench style, with shrinkage enhanced by high residual c_{H2O} in the melt (i.e., P_{final}), increasing T_d, and slower quench rates.

The procedures presented here demonstrate how vesicle shrinkage can be determined, and how we can gain insight into the processes controlling shrinkage for experimentally vesiculated and quenched samples. While we can extract semi-quantitative information that constrains whether melt degassing is occurring in equilibrium or disequilibrium, we highlight the need for improved understanding of EOS- and resorption shrinkage through both in-situ decompression experiments and numerical modelling.

The present study was limited to phonolitic melts, but while the processes controlling shrinkage will be less pronounced in rhyolitic melts, they should still be important, and shrinkage will be especially significant for decompression experiments on melts with high H_2O diffusivity and low melt viscosity. It is therefore critical to consider vesicle shrinkage before porosity and c_{H2O} data from postmortem samples of decompression experiments are used for interpreting vesiculation of silicate melts. Otherwise, melt porosity is significantly underestimated leading to a false interpretation of the onset of coalescence, percolation or the distinction between equilibrium or disequilibrium degassing of a melt.

5. Supplement

5.1 RMS and FTIR supplementary information

5.1.7 Calibration of Raman micro-spectroscopy (RMS) for quantitative H_2O determination

Calibration was performed using the hydrated VAD79 samples REF02–06 from Marxer et al. (2015) and an unpublished sample that was hydrated with 1.37 wt% H_2O. H_2O concentrations are known from FT-NIR measurements of Marxer et al. (2015). For each standard sample 4–7 RMS spectra were acquired, part of which were measured before and part of which was measured directly after the mapping, without changing the optical setting of the instrument. Measurement setting for the calibration were the same as for the mapping of CD73 presented in the paper: a 50× objective with a numerical aperture of 0.75 was used, and spectra were collected from 100–4000 cm^{-1} in high confocality setting with an acquisition time of 10 s. Spectra were corrected for frequency-dependent scattering intensity of the laser and the temperature and baseline subtracted using the Matlab©-script provided by Di Genova et al. (2017a). After this treatment, the Matlab©-script calculates the band area of the low wavenumber (LW, 200–1250 cm^{-1}) alumino-silicate bands and the fundamental OH stretching band at high wavenumber (3450 cm^{-1}; HW) representing total dissolved H_2O. Baseline substraction is exemplarily shown in Fig. III.A1.

Table III.A1 Hydrated VAD79 reference samples (Marxer et al. 2015) used for c_{H2O} calibration of Raman spectroscopy data. Samples were hydrated in the IHPV at 1323 K and 200 MPa and were equilibrated for 96 h.

sample	c_{H2O} (FTIR) [wt%]	absolute error in c_{H2O} [wt%]
REF01	1.37	0.13
REF02	2.20	0.16
REF03	3.10	0.21
REF04	4.10	0.28
REF05	5.15	0.36
REF06	5.60	0.40

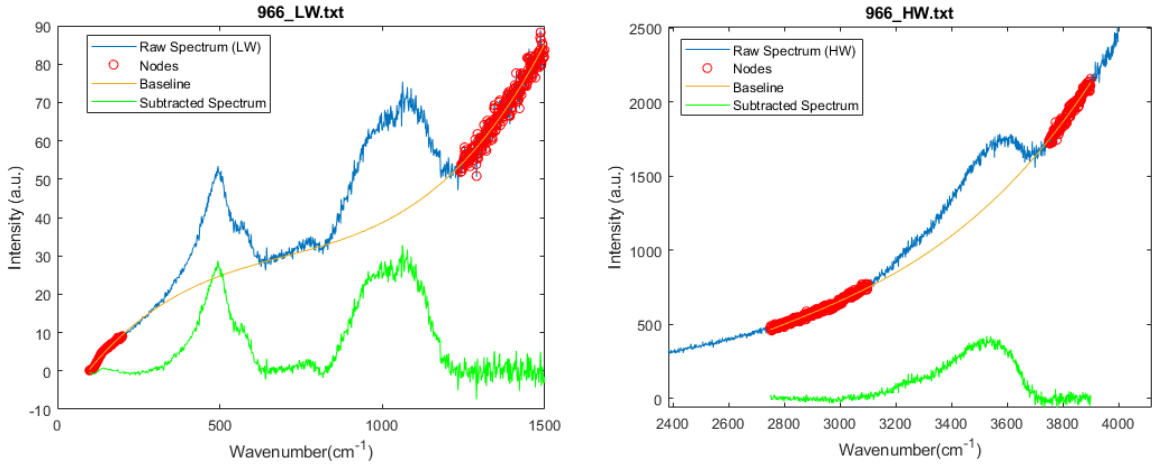

Fig. III.A1 Images generated by the Matlab©-Script provided by Di Genova et al. (2017a). The images show raw Raman spectra (blue) and baseline substracted Raman spectra (green) of the LW band (left) and HW water band (right).

We used two types of calibration: (1) Calibration of the H_2O band (HW) area, which is also known as "external calibration" and (2) the ratio of the HW and the LW band areas (HW/LW), also known as "internal calibration" (Schiavi et al. 2018). However, we calibrated both, HW and HW/LW against the external standards. Weighted least-squares linear regressions (Fig. III.A2) with R^2 of 0.97 and 0.98, respectively, are obtained for the homogeneous hydrous VAD79 standard glasses (Table III.A1) and the given measurement settings. The linear dependency of HW/LW vs. c_{H2O} from FTIR measurements was used to process the mapped Raman data of sample CD73.

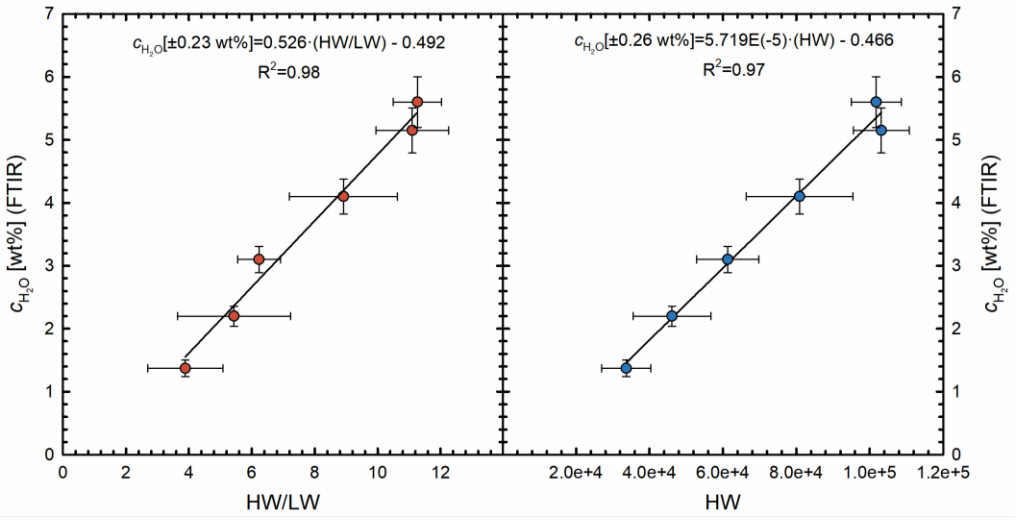

Fig. III.A2 Weighed least-squares linear regressions of HW/LW and HW band calibration to c_{H2O} from FTIR. Error bars in c_{H2O} are absolute errors from FT-NIR-H_2O determination. Error bars in HW/LW and HW band area indicate the standard deviation from multiple measurements.

5.1.8 Penetration depth during H_2O mapping of partly degassed phonolitic glasses

FTIR- ATR spectroscopy

The effective penetration depth (d_p) of the evanescent wave during ATR measurement with FTIR was calculated for the Bruker Hyperion3000 microscope equipped with a Ge-crystal ATR objective (20×) after Compton and Compton (1993):

$$d_p = \frac{\lambda}{2\pi n_p (sin^2\theta - n_{sp}^2)^{\frac{1}{2}}} \quad \text{(III.A1)}$$

where λ is the wavelength of radiation in the Ge-crystal, θ ist the angle of incidence, n_p the refractive index of the ATR Ge-crystal (= 4.0) and n_{sp} is the refractive index ratio of the glass sample and the ATR crystal. The angle of incidence in the optical setup used in this study is fixed at ~37°. Using the linear dependency of glass density as a function of H_2O concentration (c_{H2O}) for phonolitic glass (Eqn. 2; Iacono-Marziano et al. (2007) yields glass a density of ~2.4 g·cm^{-3} for 3.5–6 wt% H_2O.

$$\rho\left[\frac{g}{cm^3}\right] = 2.47 - 0.013 \cdot c_{H2O} \quad \text{(III.A2)}$$

The corresponding refractive index determined from Tan and Arndt (2001) is ~1.5 at a light wavelength of 0.59 µm. The refractive index decreases only slightly with increasing wavelength (Tan and Arndt 2001). Thus, 1.5 is used to calculate penetration depth for the 3450 cm^{-1} water band (λ = 2.899 µm), which yields a d_p of 0.25 µm.

Comparison of penetration depth using Raman and FTIR-ATR spectroscopy

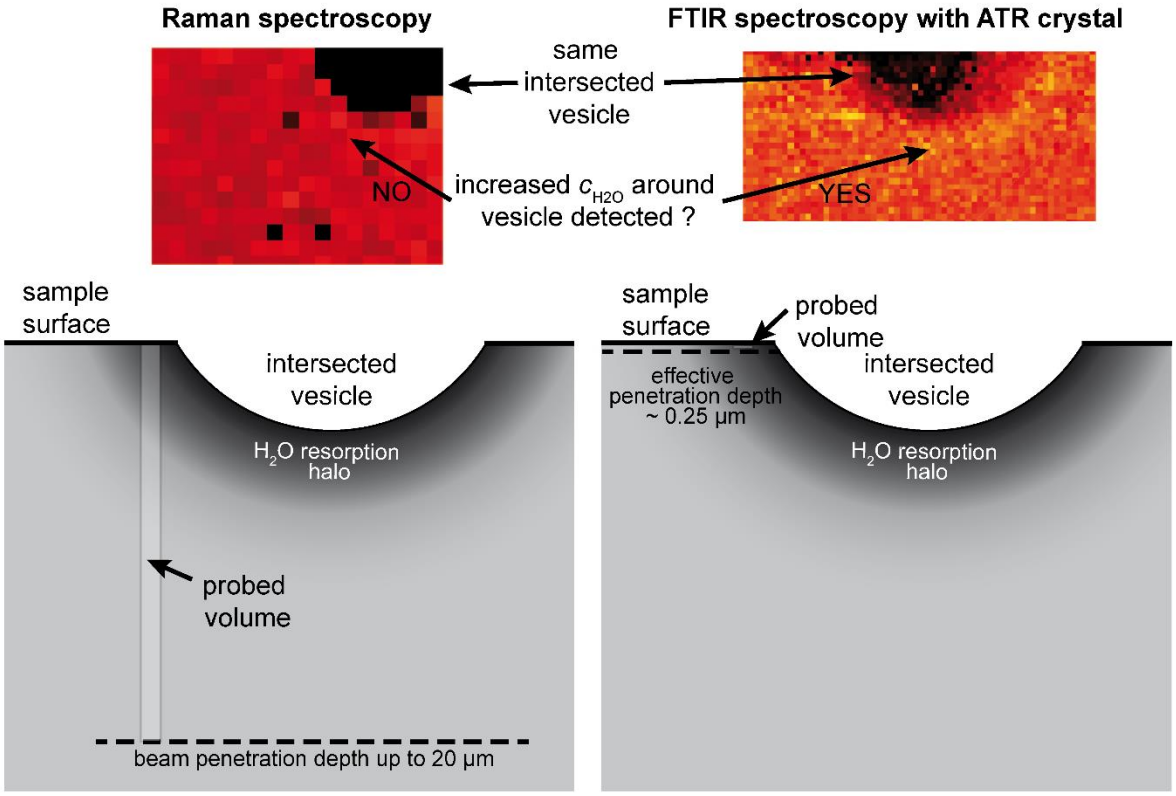

Fig. III.A3 Schematic comparison of penetration depth of confocal Raman spectroscopy measurements on sample CD73 with FTIR-ATR explaining why an increased c_{H2O} is detectable around intersected vesicles with FTIR-ATR-FPA mapping, but not with Raman spectroscopy.

The different penetration depths of RMS and FTIR-ATR spectroscopy explain the differences in relative H_2O concentration changes of the 2D maps that are obtained from both methods. In the RMS-map no increase in c_{H2O} around intersected vesicles is observed (Fig. A3), while such an increase in c_{H2O} is found with FTIR-ATR spectroscopy.

The sample volume probed by Raman spectroscopy is ~20 µm deep and the high c_{H2O} in the resorption halo is diluted by the signal of the glass below with less H_2O. In contrast to that, using the FTIR-ATR method with the low penetration depth, the increase in c_{H2O} close to the vesicle can be detected (Fig. III.A3). Concluding, with both methods H_2O-gradients of vesiculated silicate glasses can be detected. Although it is not clear what the effect of vesicle

walls within the laser-excited sample volume is, Raman spectroscopy reveals depth information that can be well quantified, at least for the vesicle free regions of the glass. FTIR-ATR spectroscopy is more suitable for surface-near high spatial resolution measurements. However, perfectly flat sample surfaces and tilt-free alignment with the ATR-crystal are required.

5.2 Literature review

The supplement "literature review" is an MS Excel file available as online resource under the following link (open access):
https://static-content.springer.com/esm/art%3A10.1007%2Fs00410-020-1658-3/MediaObjects/410_2020_1658_MOESM1_ESM.xlsx

References

Alidibirov M, Dingwell DB (1996) Magma fragmentation by rapid decompression. Nature 380:146-148

Allabar A, Nowak M (2018) Message in a bottle: Spontaneous phase separation of hydrous Vesuvius melt even at low decompression rates. Earth Planet Sci Lett 501:192-201

Allabar A, Salis Gross E, Nowak M (2020a) The effect of initial H_2O concentration on decompression-induced phase separation and degassing of hydrous phonolitic melt. Contrib Mineral Petrol 175:22

Allabar A, Dobson KJ, Bauer CC, Nowak M (2020b) Vesicle shrinkage in hydrous phonolitic melt during cooling. Contrib Mineral Petrol 175:21

Allabar A, Dobson KJ, Bauer CC, Nowak M (2020c) Correction to: "Vesicle shrinkage in hydrous phonolitic melt during cooling". Contrib Mineral Petrol 175:41

Bagdassarov N, Dorman A, Dingwell DB (2000) Effect of alkalis, phosphorus, and water on the surface tension of haplogranite melt. Am Mineral 85:33-40

Barone G, Mazzoleni P, Corsaro RA, Costagliola P, Di Benedetto F, Ciliberto E, Gimeno D, Bongiorno C, Spinella C (2016) Nanoscale surface modification of Mt. Etna volcanic ashes. Geochim Cosmochim Acta 174:70-84

Behrens H et al. (1996) Near-infrared spectroscopic determination of water species in glasses of the system $MAlSi_3O_8$(M = Li, Na, K): an interlaboratory study. Chem Geol 128:41-63

Berndt J, Liebske C, Holtz F, Freise M, Nowak M, Ziegenbein D, Hurkuck W , Koepke J (2002) A combined rapid-quench and H_2-membrane setup for internally heated pressure vessels: Description and application for water solubility in basaltic melts. Am Mineral 87:1717-1726

Binder K (1984) Nucleation barriers, spinodals, and the Ginzburg criterion. Phys Rev A 29: 341-349

Bureau H, Keppler H (1999) Complete miscibility between silicate melts and hydrous fluids in the upper mantle: Experimental evidence and geochemical implications. Earth Planet Sci Lett 165(2):187-196

Burnham CW, Davis NF (1971) The role of H_2O in silicate melts: 1. P-V-T relations in the system $NaAlSi_3O_8$-H_2O to 10 kilobars and 1000 °C. Am J Sci 270:54-79

Cahn JW, Hillard JE (1959) Free energy of a nonuniform system, III: nucleation in a two-component incompressible fluid. J Chem Phys 31:688-699

Cahn JW (1965) Phase separation by spinodal decomposition in isotropic systems. J Chem Phys 42:93-99

Castro JM, Burgisser A, Schipper CI, Mancini S (2012) Mechanisms of bubble coalescence in silicic magmas. Bull Volcanol 74:2339-2352

Cioni R, Civetta L, Marianelli P, Metrich N, Santagrone, R, Sbrana A (1995) Compositional Layering and Syn-ruptive Mixing of a Periodically Refilled Shallow Magma Chamber: the AD79 Plinian Eruption of Vesuvius. J Petrol 36:739-776

Cioni R (2000) Volatile content and degassing processes in the AD79 magma chamber at Vesuvius (Italy) Cotrib Mineral Petrol 140:40-54

Cioni R, Bertagnini A, Santacroce R, Andronico D (2008) Explosive activity and eruption scenarios at Somma-Vesuvius (Italy): Towards a new classification scheme. J Volcanol Geotherm Res 178:331-346

Cluzel N, Laporte D, Provost A (2008) Kinetics of heterogeneous bubble nucleation in rhyolitic melts: implications for the number density of bubbles in volcanic conduits and for pumice textures. Contrib. Mineral. Petrol. 156:745-763

Compton SV, Compton DAC (1993) Optimization of data recorded by internal reflectance spectroscopy. In Coleman PB, Ed, Practical Sampling Techniques for Infrared Analysis, 55-92. CRC Press, Boca Raton, Florida

Cormier L, Dargaud O, Calas G, Jousseaume C, Papin S, Trcera N, Cognigni A (2015) Zr environment and nucleation role in aluminosilicate glasses. Mater Chem Phys 152:41-47

Costa A (2005) Viscosity of high crystal content melts: Dependence on solid fraction. Geophys Res Lett 32:1-5

Dargaud O, Cormier L, Menguy N, Patriarche G, Calas G (2011) Mesoscopic scale description of nucleation processes in glasses. Appl Phys Lett 99:021904

De Vivo B, Lima A, Webster JD (2005) Volatiles in Magmatic-Volcanic Systems. Elements 1:19-24

Debenedetti PG (2000) Phase separation by nucleation and by spinodal decomposition: fundamentals. In: Kiran E, Debenedetti PG, Peters CJ (Eds.), Supercritical Fluids. In: Nato Science Series E, vol.366, pp 123-166

Devine JD, Gardner JE, Brack HP, Layne GD, Rutherford MJ (1995) Comparison of microanalytical methods for estimating H2O contents of silicic volcanic glasses. Am Mineral 80:319-328

Di Genova D, Sicola S, Romano C, Vona A, Fanara S, Spina L (2017a) Effect of iron and nanolites on Raman spectra of volcanic glasses: A reassessment of existing strategies to estimate the water content. Chem Geol 475:76-86

Di Genova D, Kolzenburg S, Wiesmaier S, Dallanave E, Neuville DR, Hess KU, Dingwell DB (2017b) A compositional tipping point governing the mobilization and eruption style of rhyolitic magma. Nature 552:235-238

Di Genova D, Caracciolo A, Kolzenburg S (2018) Measuring the degree of "nanolitization" of volcanic glasses: Understanding syn-eruptive processes recorded in melt inclusions Lithos 318-319:209-218

Dingwell DB, Webb SL (1990) Relaxation in Silicate Melts. Eur J Mineral 2:427-449

Duan ZH, Zhang ZG (2006) Equation of state of the H_2O, CO_2, and H_2O-CO_2 systems up to 10 GPa and 2573.15 K: Molecular dynamics simulations with ab initio potential surface. Geochim Cosmochim Acta 70:2311-2324

Everall NJ (2000) Confocal Raman Microscopy: Why the Depth Resolution and Spatial Accuracy Can Be Much Worse than You Think. Appl Spectrosc 54:1515-1520

Fabbrizio A, Carroll MR (2008) Experimental constraints on the differentiation process and pre-eruptive conditions in the magmatic system of Phlaegrean Fields (Naples, Italy). J Volcanol Geoth Res 171(1-2):88-102

Fanara S, Botcharnikov RE, Husen A, Buddensieck J, Behrens H (2012) Pre-eruptive conditions of the Campanian Ignimbrite eruption: experimental constraints from phase equilibria and volatile solubility studies. Proceedings of IODP-ICDP Kolloquium: 41-43, Kiel, Germany.

Fanara S, Behrens H, Zhang YX (2013) Water diffusion in potassium-rich phonolitic and trachytic melts. Chem Geol 346:149-161

Foden J (1986) The petrology of Tambora volcano, Indonesia: a model for the 1815 eruption. J Volcanol Geotherm Res 27:1-41

Fortelný I, Živný A, Jůza J (1999) Coarsening of the Phase Structure in Immiscible Polymer Blends. Coalescence or Ostwald Ripening? J Polym Sci 37:181-187

Gardner JE, Hilton M, Carroll MR (1999) Experimental constraints on degassing of magma: Isothermal bubble growth during continuous decompression from high pressure. Earth Planet Sci Lett 168:201-218

Gardner JE, Ketcham RA (2011) Bubble nucleation in rhyolite and dacite melts: temperature dependence of surface tension. Contrib Mineral Petrol 162:929-943

Gardner JE (2012) Surface tension and bubble nucleation in phonolite magmas. Geochim Cosmochim Ac 76:93-102

Gardner JE, Wadsworth FB, Llewellin EW, Warkins JM, Coumans JP (2019) Experimental constraints on the textures and origin of obsidian pyroclasts. Bull Volcanol 81:22

Genareau K, Proussevitch AA, Durant AJ, Mulukutla G, Sahagian DL (2012) Sizing up the bubbles that produce very fine ash during explosive volcanic eruptions. Geophys Res Lett 39:L15306

Gervasoni F, Klemme S, Rocha-Júnior ERV, Berndt J (2016) Zircon saturation in silicate melts: a new and improved model for aluminous and alkaline melts. Contrib Mineral Petrol 171:21

Giachetti et al. (2019) Bubble Coalescence and Percolation Threshold in Expanding Rhyolitic Magma. Geochem Geophys 20:1054-1074

Giordano D, Russell JK, Dingwell DB (2008) Viscosity of magmatic liquids: A model. Earth Planet Sci Lett 271:123-134

Gonnermann HM, Manga M (2007) The fluid mechanics inside a volcano. Annu Rev Fluid Mech 39:321-356

Gonnermann HM, Gardner JE (2013) Homogeneous bubble nucleation in rhyolitic melt: Experiments and nonclassical theory. Geochem Geophys Geosys 14:4758-4773

Gurioli L, Houghton BF, Cashman KV, Cioni R (2005) Complex changes in eruption dynamics during the 79 AD eruption of Vesuvius. Bull Volcanol 67:144-159

Hajimirza S, Gonnermann HM, Gardner JE, Giachetti T (2019) Predicting Homogeneous Bubble Nucleation in Rhyolite. JGR Solid Earth 124:2395-2416

Hamada M, Laporte D, Cluzel N, Koga KT, Kawamoto T (2010) Simulating bubble number density of rhyolitic pumices from Plinian eruptions: constraints from fast decompression experiments. Bull Volcanol 72:735-746

Hertz P (1908) Über den gegenseitigen durchschnittlichen Abstand von Punkten, die mit bekannter mittlerer Dichte im Raume angeordnet sind. Math Ann 67:387-398

Higgins MD (2000) Measurement of crystal size distributions. Am Mineral 85:1105-1116

Higgins MD (2006) Quantitative Textural Measurements in Igneous and Metamorphic Petrology. Cambridge University Press, New York.

Holtz F, Behrens H, Dingwell DB and Johannes W (1995) H_2O solubility in haplogranitic melts: Compositional, pressure, and temperature dependence. Am Mineral 80:94-108

Hurwitz S, Navon O (1994) Bubble nucleation in rhyolitic melts - experiments at high-pressure, temperature and water content. Earth Planet Sci Lett 122:267-280

Iacono-Marziano G, Schmidt BC, Dolfi D (2007) Equilibrium and disequilibrium degassing of a phonolitic melt (Vesuvius AD 79 “white pumice”) simulated by decompression experiments. J Volcanol Geotherm Res 161:151-164

Kueppers U, Scheu B, Spieler O, Dingwell DB (2006) Fragmentation efficiency of explosive volcanic eruptions: A study of experimentally generated pyroclasts. J Volcanol Geotherm Res 153:125-135

Lamorgese A, Mauri R (2016) Spinodal decomposition of chemically reactive binary mixtures. Phys Rev 94:022605

Larsen JF, Gardner JE (2004) Experimental study of water degassing from phonolite melts: implications for volatile oversaturation during magmatic ascent. J Volcanol Geotherm Res 134:109-124

Larsen JF (2008) Heterogeneous bubble nucleation and disequilibrium H2O exsolution in Vesuvius K-phonolite melts. J Volcanol Geotherm Res 175:278-288

Lindoo A, Larsen JF, Cashman KV, Dunn AL, Neill OK (2016) An experimental study of permeability development as a function of crystal-free melt viscosity. Earth Planet Sci Lett 435:45-54

Liu Y, Zhang Y, Behrens H (2005) Solubility of H_2O in rhyolitic melts at low pressures and a new empirical model for mixed H_2O-CO_2 solubility in rhyolitic melts. J Volcanol Geotherm Res 143:219-235

Llewellin EW, Coumans JP, Humphreys M, Wadsworth FB, Dobson KJ, Allabar A, Brooker RA, Mathias S, Gardner JE, Coggins J (2019) A validated numerical model for the growth and resorption of bubbles in magma. Abstract, AGU Fall Meeting 2019. San Francisco, USA

Lowenstern JB, Pitcher BW (2013) Analysis of H_2O in silicate glass using attenuated total reflectance (ATR) micro-FTIR spectroscopy. Am Mineral 98:1660-1668

Lubetkin SD (2003) Why Is It Much Easier To Nucleate Gas Bubbles than Theory Predicts? Langmuir 19:2575-2587

Malfait WJ, Halter WJ (2008) Structural relaxation in silicate glasses and melts: High-temperature Raman spectroscopy. Phys Rev 77:014201

Mangan M, Sisson T (2000) Delayed, disequilibrium degassing in rhyolite magma: decompression experiments and implications for explosive volcanism. Earth Planet Sci Lett 183:441-455

Marxer H, Bellucci P, Nowak M (2015) Degassing of H_2O in a phonolitic melt: a closer look at decompression experiments. J Volcanol Geotherm Res 297:109-124

Masotta M, Keppler H (2017) A new hydrothermal moissanite cell apparatus for optical in-situ observations at high pressure and high temperature, with applications to bubble nucleation in silicate melts. Am Mineral 102:2022-2031

Mastrolorenzo G, Brachi L, Canzanella A (2001) Vesicularity of various types of pyroclastic deposits of Campi Flegrei volcanic field: evidence of analogies in magma rise and vesiculation mechanisms. J Volcanol Geotherm Res 109:41-53

Mcintosh I, Llewellin E, Humphreys M, Nichols A, Burgisser A, Schipper CI, Larsen J (2014) Distribution of dissolved water in magmatic glass records growth and resorption of bubbles. Earth Planet Sci Lett 401:1-11

McIntosh et al. (2015) 'Practical' glass transition temperatures of vesicular glasses: a combined FTIR-XRCT approach. Abstract, 10th Silicate melt workshop. La Petite Pierre, France

Miller CF, Wark DA (2008) Supervolcanoes and their explosive supereruptions. Elements 4:11-16

Mongrain J, Larsen JF, King PL (2008) Rapid water exsolution, degassing, and bubble collapse observed experimentally in K-phonolite melts. J Volcanol Geotherm Res 173:178-184

Mourtada-Bonnefoi C, Laporte D (2004). Kinetics of bubble nucleation in a rhy-olitic melt: an experimental study of the effect of ascent rate. Earth Planet Sci Lett 218:521-537

Mujin M, Nakamura M (2014) A nanolite record of eruption style transition. Geology 42:611-614

Mujin M, Nakamura M, Miyake A (2017) Eruption style and crystal size distributions: crystallization of groundmass nanolites in the 2011 Shinmoedake eruption. Am Mineral 102(12):2367-2380

Mysen B (2014) Water-melt interaction in hydrous magmatic systems at high temperature and pressure. Prog in Earth and Planet Sci 1:4:1-18

Navon O, Lyakhovsky V (1998) Vesiculation processes in silicic magmas. In: Gilbert, J.S and Sparks, R.S.J. (eds). The Physics of Explosive Volcanic Eruptions. Geological Society, London, Special Publications 145:27-50

Nowak M, Behrens H (1995) The speciation of water in granitic glasses and melts determined by in situ near-infrared spectroscopy. Geochim Cosmochim Acta 59:3445-3450

Nowak M, Behrens H (1997) An experimental investigation of diffusion of water in haplogranitic melts. Contrib Mineral Petrol 126:365-376

Nowak M, Behrens H (2001) Water in rhyolitic magmas: getting grip on a slippery problem. Earth Planet Sci Lett 184:515-522

Nowak M, Cichy SB, Botcharnikov RE, Walker N, Hurkuck W (2011) A new type of high-pressure low-flow metering valve for continuous decompression: first experimental results on degassing of rhyodacitic melts. Am Mineral 96:1373-1380

Ochs F, Lange R (1999) The density of hydrous magmatic liquids. Science 283:1314-1317

Oh J, Rey AD (2000) Theory and simulation of polymerization-induced phase separation in polymeric media. Macromol Theory Simul 9:941-660

Orlov KA, Alexandrov AA, Ochkov VF, Ochkov AV.: WaterSteamPro™ Version 6.5.0.64. Moscow Power Engineering Institute (technical university), 1999-2010.

Ottonello G, Richet P, Papale P (2018) Bulk solubility and speciation of H_2O in silicate melts. Chem Geol 479:176-187

Paillat O, Elphick W, Brown WL (1992) The solubility of water in $NaAlSi_3O_8$ melts: a re-examination of Ab-H_2O phase relationships and critical behavior at high pressures. Contrib Mineral Petrol 112:490-500

Pan AC, Rappl RJ, Chandler D, Balsara NP (2006) Neutron Scattering and Monte Carlo Determination of the Variation of the Critical Nucleus Size with Quench Depth J Phys Chem 110:3692-3696

Papale P, Dobran F (1993) Modeling of the ascent of magma during the plinian eruption of Vesuvius in A.D.79. J Volcanol Geotherm Res 58:101-132

Parsons I, Brown WL (1991) Mechanisms and kinetics of exsolution -structural control of diffusion and phase behaviour in alkali feldspars. In: Diffusion, atomic ordering and mass transport. J Ganguly (Ed) Advances in Physical Geochemistry Vol. 8. Springer Verlag

Petrishcheva E, Abart R (2012) Exsolution by spinodal decomposition in multicomponent mineral solutions. Acta Mater 60(15):5481-5493

Preuss O, Marxer H, Ulmer S, Wolf J, Nowak M (2016) Degassing of hydrous trachytic Campi Flegrei and phonolitic Vesuvius melts: experimental limita-tions and chances to study homogeneous bubble nucleation. Am Mineral 101:859-875

Proussevitch AA, Sahagian DL (1996) Dynamics of coupled diffusive and decompressive bubble growth in magmatic systems. J Geophys Res 101:17,447-17,455

Ryan AG, Russel JK, Nichols ARL, Hess KU, Porritt LA (2015) Experiments and models on H_2O retrograde solubility in volcanic systems. Am Mineral 100:774-786

Sahagian D, Carley TL (2020) Explosive Volcanic Eruptions and Spinodal Decomposition: A Different Approach to Deciphering the Tiny Bubble Paradox. Geochem Geophys Geosys 21:e2019GC008898

Scaillet B, Pichavant M, Cioni R (2008) Upward migration of Vesuvius magma chamber over the past 20,000 years. Nature 455:216-219

Schiavi F, Bolfan-Casanova N, Withers AC, Médard E, Laumonier M, Laporte D, Flaherty T, Gómez-Ulla, A (2018) Water quantification in silicate glasses by Raman spectroscopy: Correcting for the effects of confocality, density and ferric iron. Chem Geol 483:312-331

Schlinger CM, Smith RM (1986) Superparamagnetism in volcanic glasses of the KBS tuff: Transmission electron microscopy and magnetic behavior. Geophys Res Lett 13:729-732

Schlinger CM, Rosenbaum JG, Veblen DR (1988) Fe-oxide microcrystals in welded tuff from southern Nevada: Origin of remanence carriers by precipitation in volcanic glass. Geology 16:556-559

Schmalzried H (1981) Solid State Reactions Verlag Chemie, Weinheim, Florida, Basel 2nd edition.

Schmelzer JWP, Abyzov AS, Möller J (2004) Nucleation versus spinodal decomposition in phase formation processes in multicomponent solution. J Chem Phys 121:6900-6917

Schmidt BC, Behrens H (2008) Water solubility in phonolite melts: Influence of melt composition and temperature. Chem Geol 256:259-268

Sharp TG, Stevenson RJ, Dingwell DB (1996) Microlites and "nanolites" in rhyolitic glass: Microstructural and chemical characterization. Bull Volcanol 57:631-640

Shea T, Larsen JF, Gurioli L, Hammer JE, Houghton BF, Cioni R (2009) Leucite crystals: surviving witnesses of magmatic processes preceding the 79AD eruption at Vesuvius, Italy. Earth Planet Sci Lett 281(1-2):88-98

Shea T, Gurioli L, Larsen JF, Houghton BF, Hammer JE, Cashman KV (2010a) Linking experimental and natural vesicle textures in Vesuvius 79AD white pumice. J Volcanol Geotherm Res 192:69-84

Shea T, Houghton BF, Gurioli L, Cashman KV, Hammer JE, Hobden BJ (2010b) Textural studies of vesicles in volcanic rocks: An integrated methodology. J Volcanol Geotherm Res190:273-289

Shea T, Gurioli L, Houghton BF (2012) Transitions between fall phases and pyroclastic density currents during the AD 79 eruption at Vesuvius: building a transient conduit model from the textural and volatile record. Bull Volcanol 74:2363-2381

Shea T, Hellebrand E, Gurioli L, Tuffen H (2014) Conduit- to Localized-scale Degassing during Plinian Eruptions: Insights from Major Element and Volatile (Cl and H_2O) Analyses within Vesuvius AD 79 Pumice. J Petrol 55:315-344

Shea T (2017) Bubble nucleation in magmas: a dominantly heterogeneous process? J Volcanol Geotherm Res 343:155-170

Shen AH, Keppler, H (1997) Direct observation of complete miscibility in the albite-H_2O system. Nature 385:710-712

Snyder HL, Meakin P (1983) Phase separation dynamics: Comparison of experimental results. J Chem Phys 79:5588-5594

Sparks RSJ (1978) The dynamics of bubble formation and growth in magmas: a review and analysis. J Volcanol Geotherm Res 3:1-37

Stalder R, Ulmer P, Thompson AB, Günther D (2000) Experimental approach to constrain second critical end points in fluid/silicate systems: Near-solidus fluids and melts in the system albite-H_2O. Am Mineral 85:68-77

Tan CZ, Arndt J (2001) The refractive index of silica glass and its dependence on pressure, temperatre, and the wavelength of the incident light. In Nalwa HS, Ed, Silicon-Based Materials and Devices 2, Chapter 2, 50-91. Academic Press, New York

Tanaka H, Yokokawa T, Abe H, Hayashi T, Nishi T (1990) Transition from metastability to instability in a binary-liquid mixture. Phys Rev Lett 65:3136-3139

Thomas N, Jaupart C, Vergniolle S (1994) On the vesicularity of pumice. J Volcanol Geotherm Res 99: 633-15

Tolman RC (1949) The Effect of Droplet Size on Surface Tension. J Chem Phys 17, 333

Toramaru A (1998) Formation of propagation pattern in two-phase flow systems with application to volcanic eruptions. Geophys J 95:613-623

Toramaru A (2006) BND (bubble number density) decompression rate meter for explosive volcanic eruptions. J Volcanol Geotherm Res 154:303-316

Watson EB, Harrison TM (1983) Zircon saturation revisited: temperature and composition effects in a variety of crustal magma types. Earth Planet Sci Lett 64:295-304

Webster JD, Golfogg B, Stinoni MF, Shimizu N, De Vivo B (2014) C-O-H-Cl-S-F Volatile Solubilities, Partitioning, and Mixing in Phonolitic-Trachytic Melts and Aqueous-CarbonicVapor±Saline Liquid at 200MPa. J Petrol 55:2217-2248

Xiong Y, Kiran E (1998) High-pressure light scattering apparatus to study pressure-induced phase separation in polymer solutions. Rev Sci Instrum 69:1463-1471

Zhang Y, Xu Z, Behrens H (2000) Hydrous species geospeedometer in rhyolite: Improved calibration and application. Geochim Cosmochim Acta 64:3347-3355

Zhuang W, Kiran E (1998) Kinetics of pressure-induced phase separation (PIPS) from polymer solution by time-resolved light scattering. Polyethylene + n-pentane. Polymer 13:2903-2915